UNIVERSITY OF BIRMINGHAM

FLOWABILITY AND STORAGE STABILITY OF HIGHLY ACTIVE POWDER SURFACTANT SYSTEMS

by

Bingyu Zhuo

A thesis submitted to the University of Birmingham for the degree of

DOCTOR OF PHILOSOPHY

School of Chemical Engineering
College of Physical and Engineering Sciences
University of Birmingham
October 2018

Abstract

Surfactant powder is a highly valuable product with many applications. It was felt desirable to enhance the physical stability of the powder so that it could be transported over long distances and to ensure its quality at end-use applications. Two different surfactant samples (with 33 wt% and 70 wt% surfactant content) were used in this research.

Firstly, the powders were characterised by their physical characteristics, mechanical properties, storage stability, and flowability. In addition, the effects of the physical characteristics on the flow behaviour of highly concentrated surfactant granules of different size ranges were studied. These studies showed that the surfactant powders were prone to picking up moisture and deliquescing under high humidity, poor in flow, and easily deformable.

Several materials (NaCl, KCl, Na_2SO_4, and EwBase) were used to coat the surfactant powders using a fluidised bed coater. The salt coating improved the flowability of the powder, but apart from Na_2SO_4, they all also reduced the deliquescence humidity of the powders. It was demonstrated that the Na_2SO_4 coating improved both the flowability and storage stability of the highly concentrated surfactant powder system. It was also shown that the enhanced flowability was related to the increase in the

Heckel parameter when a salt coating of more than 70% surface coverage was achieved.

For surfactant powder, it was also found that reduction in particle size increased the flowability, until the van der Waal's force became more significant and reduced the effect. The flowability and particles properties were fitted into a flowability prediction model established by Liu *et al.* (2008), and discrepancy was found between the data and the model. The model was thus further developed to seek a better understanding of the relationship between powder flowability and mechanical properties based on the Heckel parameter. It was demonstrated that improved flowability of the bulk powder was related to an increase in the Heckel parameter of the particles.

Overall, this report demonstrated a method in enhancing flowability of soft particle with salt coating, and also extends the understanding between powder's flowability and its mechanical properties.

Dedications

I would firstly like to express my deepest gratitude to my supportive supervisor who has offered me this opportunity and guided me through these years. In addition, I would like to thank the industrial counterparts of this project, Jerome Castro, Nigel Somerville-Roberts, and Clare Martins from P&G for their support and guidance in my research. I would also like to extend my appreciation to the participants of the CHARIOT research consortium, who have given me valuable feedback through these years.

I would not have been able to complete the course without support from my friends at the University of Birmingham. A special shout out to my group members, Javier, Mariana, Andy, Toni, Teddy, Xiaotong, Gilmore, LeiXing, Tom, Jesus, and Ling He (the list could go on forever), for the support they provided in the lab and with the entertainment. I also thank my leisure support team, Michal and Ben (s) for their friendship during my writing up of the thesis. Moreover, I would like to thank the team member in A.C.E, and Ana for those special memories in Birmingham. Of course, my deepest appreciation goes to my parents and grandma, who brought me up to be who I am now and supported me through all the years. Thank you.

Acknowledgement

The author gratefully acknowledges the financial support from Technology and Science Board, UK (Grant Number: TS/L003473/1), which funded a project called “CHARIOT” via a government supply chain fund, “the Advance Manufacturing Supply Chain Initiative”, aiming to rebuild British manufacturing prowess.

Table of Contents

List of Figures

List of Tables

Nomenclature

a	Kawakita constant	-
a_0	Inter-particle separation without external force	m
B	Proportionality constant	-
b^{-1}	Kawakita parameter	Pa
C	Kawakita constant	-
C_H	Hamaker constant	J
d	Diameter of the particle	m
d_{32}	Sauter mean diameter	m
D_{tablet}	Diameter of the tablet	m
$d_{v,10}$	Diameter of the 10th percentile particle	m
$d_{v,50}$	Diameter of the 50th percentile particle	m
$d_{v,90}$	Diameter of the 90th percentile particle	m
$d_{v,min}$	Minimum volume-based diameter	m
E	Young's modulus	Pa
e	Constant	-
F_{adh}	Adhesion force	N
$F_{adh,0}$	Adhesion force with absence of deformation	N
F_{CP}	Resultant force of reduced hydrostatic forces in the liquid found in the bridge	N
F_{CT}	Surface tension force acting on the axial component at the interface	N
F_D	Normal force in the Derjaguin model	N
F_D	Normal force in the JKR model	N
F_{DMT}	Normal force in the DMT model	N
F_{ext}	Force acting between two surfaces with minimum separation without contact	N
ff_c	Flowability index	-

F_H	Normal force in the Hertz model	N
F_{HO}	Adhesion between particles in the absence of normal force	N
F_{max}	Maximum force first observed in the compression	N
F_N	Normal force	N
F_{off}	Pull-off force between two surfaces	N
f_{pl}	Contact area due to plastic deformation	m^2
F_t	Deformation of two contacting particles with a force	N
F_{vdW}	van der Waal's force	N
g	Gravitational force	$m\,s^{-2}$
H	Hardness of a material	m
h	Height at the applied stress	m
h_0	Degree of volume reduction	-
h_i	Initial height	m
HR	Hausner ratio	-
h_r	Surface asperity	m
i	Displacement in the vertical direction	m
k	Constant related to plastic contact failure between particles	-
K_1	Adams constant	-
K^{-1}	Heckel parameter	Pa
N	Number of taps for Kawakita equation	-
n	Number of the sample population	-
P	Pressure	Pa
p	Probability (significance level)	-
p_{c1}	Vapour pressure above the particles	Pa
p_{c2}	Vapour pressure above the sinter bridge	Pa

P_m	Mean pressure in the compression	Pa
P^{sat}	Saturated vapour pressure	Pa
p_{vdw}	van der Waal's pressure	Pa
r	Contact radius	m
R	Radius	m
R_1	Radius of particle 1	m
R_2	Radius of particle 2	m
R_E	Equivalent radius	m
R_G	Gas constant	-
RH_0	Specific relative humidity	%
r_K	Kelvin radius	m
r_{mean}	Mean radius of the particle	m
s	Distance	m
S_a	Surface average roughness	m
S_{oblate}	Surface area	m^2
s_r	Radius of curvature between the particles	m
s_x	Standard deviation	-
t	Tablet thickness	m
T	Temperature of the system	K
v	Poisson's ratio	-
V	Volume of the gas adsorbed	m^3
V_{int}	Interaction potential	J m^{-2}
V_{LM}	Molar volume of the liquid	m^3
V_m	Volume of the monolayer of adsorbent on the surface	m^3
V_N	Volume of the material	m^3
V_O	Initial volume of the bulk material	m^3

V_p	Volume of a sphere	m^3
W	Ratio of equilibrium constants	-
w	Viscous sintering	-
x_{ad}	Coefficient of adhesion due to plastic deformation	m^2
x_{height}	Particle initial height	m
x_{width}	Particle initial width	M

Geek Symbols

μ	Viscosity of a material	Pa.s
ϕ	Sphericity	-
ϕ_x	Sphericity of a particle of the measured Feret diameter	-
α'	Apparent coefficient of friction	
α_M	Angle of repose	°
β	Half-angle	°
Γ	Work of adhesion in the JKR model	J m^{-2}
γ_{LV}	Surface tension of the liquid in the vapour phase	N m^{-1}
δ	Equivalent to half of the total displacement	m
δ_{fp}	Neck height formed in deformation	m
δ_H	Penetration in the Hertz prediction	m
δ_{pen}	Rigid body displacement in the DMT prediction	-
ε	Bulk powder bed voidage	-
ε_n	Natural strain in the packed bed	-
ζ	Adhesion energy at the contacting surface in DMT model	J m^{-2}
θ	Effective angle of internal friction	°
κ	Constant related to the plasticity of a material	-
κ_t	Constant related to the plasticity of a material under time consolidation	-
ρ^*	Relative density	kg m^3
ρ_B	Bulk density	kg m^3
ρ_P	Particle density	kg m^3
ρ_T	Tapped bulk density	kg m^3
σ	Applied normal stress	Pa
σ_1	Major consolidation stress	Pa

σ_2	Minor consolidation stress	Pa
σ_C	Unconfined yield strength	Pa
σ_h	Horizontal stress	Pa
σ_o	Uniaxial yield stress	Pa
σ_v	Vertical stress	Pa
σ_z	Stress applied in the z-axis	Pa
τ	Failure stress	Pa
τ'_o	Apparent strength of the single particles	Pa
τ_{0s}	Nominal Strength of the particle	Pa
$\tau_{contact}$	Duration of contact between the two particles	s
τ_{max}	Maximum shear stress	Pa

Chapter 1. Introduction

1.1 Surfactant Powder Systems

Surfactant is the main component in the total formulation of detergent, constituting 15–40 wt%. The functions of surfactant can also be applied to other diverse products, such as motor oil, medicine, drilling, flotation agents, electronic printing, microelectronics, and viral research, to name a few. For this reason, surfactant is considered to be one of the most versatile products in the chemical industry (Rosen & Kunjappu, 2012). The hydrophobic and hydrophilic features of the surfactant, such as wetting ability, emulsifying ability, dispersive ability, foaming ability and foaming control ability, can all be varied to change its properties (Yu, et al., 2008).

There are different classes of surfactants, such as anionic, non-ionic, cationic, zwitterionic, and silicone surfactants (Yu, et al., 2008). *Zwitterionic surfactant* consists of two charged groups of different signs under normal conditions. The main type of zwitterionic surfactant, amphoteric surfactant, can be either cationic, zwitterionic, or anionic under the influence of solutions with varying pH (Bajpai & Tyagi, 2007). A combination of various surfactants is commonly applied to achieve better detergency performance compared to a formula that only contains a single surfactant (Yu, et al., 2008).

Although mixtures of different surfactants have been used in the past, the linear alkylbenzene sulfonate (LAS), anionic surfactants with the chemical formula of $RC_6H_4SO^-_3M^+$, dominate the formulation of washing detergents (Yu, et al., 2008; Rosen & Kunjappu, 2012). This type of surfactant is widely used because it is highly soluble in water, it is not affected by a low pH environment or hardness of the water and it is relatively cheap to manufacture (Rosen & Kunjappu, 2012).

Figure 1.1 Undesired agglomerated surfactant powder system

However, powdered surfactant systems faces long-term storage stability issues in that granulates tend to form unwanted agglomeration, as shown in Figure 1.1. The process results in the reduction in the particle flow property, product quality, a loss of functionality, and can cause

segregation within the final product. The process can occur in different stages of the production, storage, and transportation of the powder (Hartmann & Palzer, 2011).

The occurrence of agglomeration is due to the hygroscopic nature of the surfactant system, and as the content of the surfactant powder increases, the particles tend to absorb more moisture (Rebecca, 2009). The phenomenon is also caused by time consolidation under the weight of the powder bed over a period of time. This behaviour was described in the work of Jenike in 1964, where the consolidation was found to be dependent on the physical properties of the powder, the external force on the particles, and environment conditions such as temperature and humidity (Teunou & Fitzpatrick, 2000).

Highly concentrated surfactant powder is desirable in the consumer industry to reduce the cost of transportation. The solid form with high surfactant content reduces the volume required during transportation. The transported powder can then be mixed into formulation in different parts of the world accordingly. This supply chain of the raw material allows savings on operating costs by reducing the manufacturing facility for surfactant. Furthermore, it allows saving by centralising the production of the surfactant. However, material is wasted when the quality of the product deteriorates during long transportation journeys. It was reported that highly concentrated surfactant powders lost their flowability and consolidated during the journey, even with sealed packaging. Godridge (2009) found that the humidity in the packaging could reach 50% RH (Rebecca, 2009).

In order to improve the flowability and storage stability of the surfactant powder, it was essential to understand the characteristics of the particles that contribute to the bulk powder's flowability and physical stability. Although currently there are several models that have been developed to understand the flowability of the powders, the complexity of the powder systems has made the prediction of their flow behaviour difficult. Furthermore, Hart & Wu (2011) demonstrated that the flowability of the detergent powder behaved differently from the correlation mentioned, where particles ranging in size from 125–180 μm had better flowability than those larger particles. There was therefore a need to investigate the impact of the physical properties of the particles on the flow behaviour of the surfactant powder system. Ultimately, it was to improve on the current model for the prediction of the powders' flowability. In addition to the above, due to the poor flowability and storage stability of the surfactant powder, it was also necessary to study methods to improve the powders' shelf life.

Typically, in the production of washing detergent, batch production is used to mix, agglomerate, coat, and to create granules. While having advantages such as quality control in batch production, continuous process is desired to increase the production rate and reducing the production cost. Therefore, it was proposed to investigate on flowability enhancement technique which can be applied with a screw mixer.

Currently, there are a few methods to improve the storage stability and flowability of powder, which include adding flow additives, coating, and

granulation. There was a need to find the right material/s and also techniques to improve the flowability and storage stability of the powder. The material used should also complement the formula of the final product.

1.2 Aims and Objectives

The main aim of the research presented in this thesis was to improve the storage stability and flowability of a highly concentrated surfactant system. It was necessary to understand the characteristics of particles in order to identify a relationship between the mechanical behaviour of the particles and their storage stability and flowability. The research also studied the impact of coating of the surfactant powders on their flowability and storage stability. In addition, the different methods for characterising time consolidation to determine the powder storage stability, and to characterise the powder's mechanical properties, were exploited.

1.3 Thesis Outline

Chapter 2. The effects of the different properties of the powders and environmental conditions on the flowability and storage stability are reviewed. Different models that have been developed to describe the flow behaviour of the powders are also presented. In addition, the various mechanisms that cause a reduction in flowability and storage stability are also presented. Different techniques for characterising the mechanical properties, flowability, and storage stability are described. The chapter

also includes different strategies to enhance the flowability of the powder product.

Chapter 3. Materials, instruments, and experimental procedures used for the characterisation of the particles are presented in this chapter. The mathematical models and data error analysis used for the characterisation are also presented.

Chapter 4. This chapter describes how the physical characteristics, mechanical properties, and hygroscopicity of two different surfactant raw powders, HiLAS 33 and HiLAS 70, were examined. The flowability and storage stability were also investigated using a Schulze's ring shear tester and an unconfined compression test. It was attempted to relate the particles' characteristics to their flowability and storage stability. Different compression models were also studied. The study aimed to provide an understanding of the difference in the particle characteristics between the two powders, and of how those characteristics are related to flowability and storage stability.

Chapter 5. A study continuing on from that described in Chapter 4 aimed to investigate how the particle size affected the flowability of the powder. An attempt was also made to establish a model to predict the flow behaviour of particles with different particle characteristics. In addition, the particles' mechanical properties were examined using both bulk and single-particle compressions.

Chapter 6. This chapter reports on how, in order to enhance the flowability of the surfactant powder, potassium chloride was used to coat the raw powder using a fluidised bed coater. The coverage and mechanical properties of the coated particles were determined together with other properties (such as particle size and shape, particle density, surface roughness, mechanical properties, and hygroscopicity). In addition, the relationship between the mechanical properties and flowability was examined.

Chapter 7. This chapter describes how, after successfully coating potassium chloride onto the surface of surfactant powder and demonstrating that the salt coating enhanced the flowability and reduced the moisture uptake of HiLAS 33, the power was also coated with sodium chloride. The results were compared to further relate the coverage and mechanical properties to the flowability. In addition, more materials (sodium sulphate and EW base) were used to examine the effect of different coating materials on the coated particles' flowability. Subsequently, the knowledge obtained was used to coat the higher concentrated surfactant powder, HiLAS 70. The coated particles were then subjected to flowability and storage stability tests.

Chapter 8: This final chapter presents the overall conclusions of the research along with recommendations for future work building on this project.

Chapter 2. Literature Review

2.1 Flowability of Powder

The ability of granular solids and powders to flow is described as flowability, where the flow behaviour is dependent on various physical characteristics and chemical properties of the materials (Ganesan, et al., 2008; Schulze, 2011). Powder is considered to have good flowability if the particles do not experience consolidation and can be transported out of a silo or hopper easily solely by the force of gravity (Schulze, 2011). The understanding of the materials' flowability is thus essential for the design of silos and other bulk solid-handling equipment to prevent flow issues such as flow blockage, segregation, non-continuous flow, and flooding (Schulze, 2011). In order to understand the flow characteristics of powder, an example of a bulk solid in a container with a positive normal compressive stress exerted in the vertical direction is illustrated in Figure 2.1.

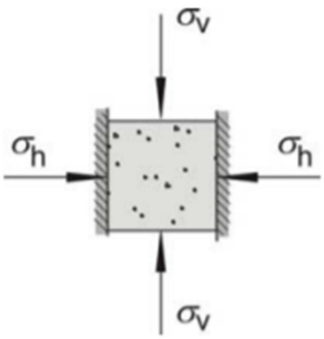

Figure 2.1 Stress element of a bulk solid in a container that is assumed to have infinite filling height and a frictionless inner wall (Schulze, 2011)

The flow behaviour of a bulk solid is different from that of a Newtonian fluid. For a Newtonian fluid, all the stresses (vertical, σ_v, and horizontal, σ_h) would have equivalent magnitude. However, for a bulk solid, the applied vertical stress from the top will result in a horizontal stress that is less than the compression stress. The ratio of the horizontal stress to the vertical stress (σ_h / σ_v) is represented by a stress ratio, which has been found to be normally between 0.3 and 0.6 (Schulze, 2011).

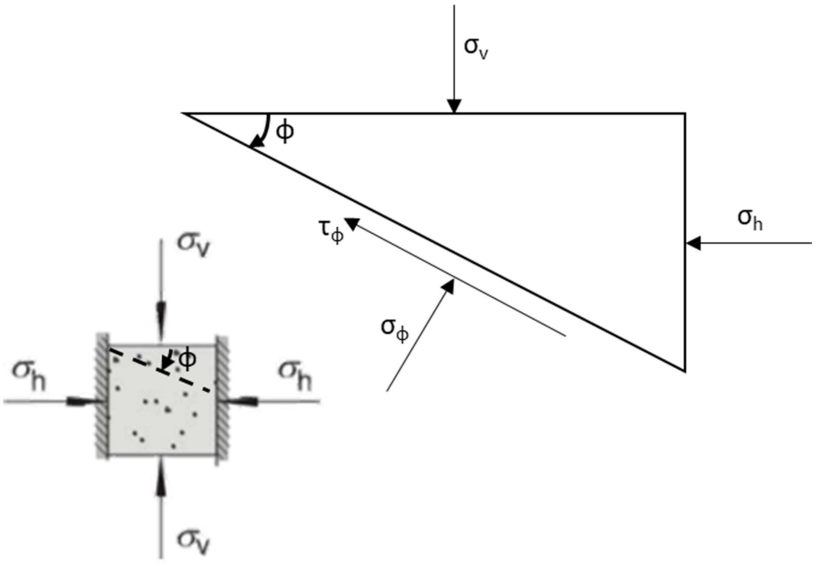

Figure 2.2 Equilibrium of stresses with cutting planes at arbitrary inclination angles (Schulze, 2011; Althaus, et al., 2012)

At different cutting planes, the bulk solid experiences different stresses, which can be analysed by balancing the forces at a triangular cross-section of the bulk solid, as shown in Figure 2.2. Assuming that the wall of the container is frictionless, and no shear stresses are applied to the top or bottom surface of the bulk solid, the normal stresses are the only external force.

2.2 The Effects of Particles' Characteristics on their Flowability

The flowability of dry powder is influenced by its material properties such as reactive chemical groups, surface free energy, adsorbate and coating, elastic modulus, and plasticity. The physical and structural properties of the particles such as size, size distribution, shape, crystallinity, porosity, and roughness can also affect the flowability (Jones, et al., 2003; Johanson, 2009). Furthermore, the environmental, storage, and process conditions can also affect the flowability of the dry powder. All these parameters can be grouped generally into three categories: i) intrinsic physical properties; ii) bulk powder properties; and iii) processing/external conditions (Leturia, et al., 2014). Due to the several parameters that can impact on the flow behaviour, a product's flow characteristic cannot be easily determined by a single correlation (Ganesan, et al., 2008; Schulze, 2011; Stoklosa, et al., 2012).

Despite the complex nature, models have been developed to predict powder flowability by relating gravitational force and the particle–particle adhesion to the powder's limiting tensile stress (Hartmann & Palzer, 2011;

Tomas, 2000; Li , et al., 2004; Liu, et al., 2008; Zhou & Peukert, 2008). Li et al. (2004) have suggested that for the powder to flow, the following condition has to be observed:

$$\rho_p d_{v,min}^3 g \geq \frac{\alpha S_C}{\varepsilon} \quad (2.1)$$

where ρ_p is the particle density, $d_{v,min}$ is the minimum volume-based diameter, g is the acceleration due to gravitational force, α is the adhesiveness between two particles, ε is the bulk powder-bed porosity, and S_C is the effective contact area between the two particles. This model hypothesised that the adhesion force between the particles is the multiple of the adhesiveness between two particles and the effective contact area (Li , et al., 2004). It was then was illustrated that when the gravitational force, contributed by parameters on the left-hand side of the equation, is greater than the cohesive forces experienced by the particles, the powder will flow.

In addition to the above, Liu *et al.* (2008) further derived Equation (2.2) from Equation (2.1), using Tomas' (2000) adhesion model, which includes both elastic and plastic local deformation when two particles are in contact (Tomas, 2000; Liu, et al., 2008). The adhesion model also considers the internal friction angle, the time-dependent internal friction angle, and the tensile strength of the packed and unpacked bulk powder. However, this model does not consider the effect of particle size (Liu, et al., 2008). In this model, Liu et al. (2008) demonstrated that the powder will flow by its own weight when the following criterion is met:

$$\rho_p d_{v,min}^3 g \geq \frac{B\pi[(1+\kappa)F_{HO} + \kappa F_N]}{\phi^2 \varepsilon} \quad (2.2)$$

where ρ_p is the particle density, $d_{v,min}$ is the minimum volume-based diameter, g is the acceleration due to gravitational force, ϕ is the sphericity, B is the proportionality constant, and ε is the bulk powder-bed voidage (Liu, et al., 2008). In addition, κ is a constant mainly related to the plastic contact failure between the particles, F_{HO} is the adhesion between particles in the absence of external normal force, and F_N is the external force applied to the powder (Tomas, 2000). F_{HO} can be described by the following equation:

$$F_{HO} = \frac{C_H h_r}{12 a_O^2} \quad (2.3)$$

where C_H is the Hamaker constant and a_0 is the inter-particle separation distance without an external force. Furthermore, h_r is the surface roughness of the particles, where h_r is smaller than the particle size.

Equation (2.2) also shows that the minimum volume-based particle diameter has a strong influence (a power of 3) on flowability. This is because the reduction in particle size can lead to an increase in the surface area per unit mass. Ultimately, the smaller particles generate stronger cohesive forces, mainly due to van der Waal's (vdW) force and hence reduce the flowability of the powder (Ganesan, et al., 2008; Fitzpatrick, et al., 2004; Seville, et al., 2000). The vdW forces play a role in enhancing the agglomeration process, especially for a dry powder system. Using Silicon Dioxide with equal spheres, it was found that vdW forces dominate the gravitational force initially, until as the particle size increases,

the gravitational force will overcome the vdW forces (Seville, et al., 2000). As a result, larger particles in general have better flowability than smaller ones (Li , et al., 2004; Seville, et al., 2000).

For the same ibuprofen powders of different sizes, Liu *et al.* (2008) found that there is a correlation between the parameters on the left-hand side in Equation (2.4) and the flowability index:

$$\ln(\rho_p d_{v,min}^3 g\phi^2\varepsilon) \propto ff_c \qquad (2.4)$$

where ff_c is the flowability index (i.e. the ratio of the consolidation stress to the unconfined yield stress), and $d_{v,\,min}$ is the minimum particle size. This correlation was derived based on the assumption that the adhesion between particles is similar, as the experiment was conducted with the same material of different sizes, while the $d_{v,\,min}$ was applied as the diameter to represent the wide particle-size distribution. Commonly, the equivalent volumetric diameter of the 10-percentiles in the powder system, $d_{v,10}$, was used instead of the smallest size of the powder system (Liu, et al., 2008). However, Hart & Wu (2011) demonstrated that the flowability of the detergent powder behaved differently from the correlation mentioned, in that particles in a size range from 125–180 μm had better flowability than those larger particles.

This inconsistency about the effect of particle size on flowability, represented by the flow index, ff_c, may be explained using Equation (2.4) which shows that apart from particle size, the flowability is also proportional to the square of the sphericity of the particle. Furthermore,

irregularity in the shape of particles for a given size can increase the number of contacts among adjacent particles, thus diminishing the flowability of the powder (Johanson, 2009; Mellmann, et al., 2013). Moreover, for particles with rough surfaces, the interlocking mechanism can result in a reduction in flowability. With this mechanism, the particles can orientate themselves and become physically bound, hence obtaining a mechanically stable system that cannot be easily disrupted and made to flow (Kock & Huhn, 2007; Peleg, 1977).

The material properties of the particles are also a vital factor in determining the flow behaviour of the powder, as shown on the right-hand side of Equation (2.2) by the κ parameter. It has been demonstrated that the more rigid the material, the better the flowability (Tomas, 2001). As the external compressive normal force is applied on a soft contact of two similar spherical particles, the contact point can be deformed, resulting in the formation of a contact area and an increase in the adhesive force between the two particles (Tomas, 2000). A more detailed discussion on contact mechanisms and adhesion models will be presented in a later section.

2.2.1 **Humidity/moisture content**

The relative humidity of the air that the material is stored in also affects a material's flowability. Basically, humidity increases the moisture content in the product, and the moisture content greatly affects the flowability of the material (Hartmann & Palzer, 2011). The moisture sorption can increase the formation of liquid bridges, resulting in increased cohesiveness

between the particles. This will alter the frictional properties of the material, such as the wall friction angle and the internal angle of friction. Furthermore, the moisture content can modify the surface properties and the adherence pattern of the particles. Different materials react differently to moisture content (Ganesan, et al., 2008).

In addition to the above, in a compaction process, the moisture content can modify the deformability of the particle. The increase in the deformability will result in the formation of solid bridges or increase the contact area between particles (Sebhatu, et al., 1997). (This mechanism will be further explained in a later section.) Furthermore, the moisture can also act as a lubricant and increase the distance between particles by forming liquid bridges. The increase in separation will result in a reduction of vdW force (Crouter & Briens, 2014; Emery, et al., 2009).

2.2.2 **Temperature**

The flowability of dry powder will be compromised when the particles are exposed to temperatures higher than a certain temperature, even when the moisture level is kept constant. This temperature is related to the glass transition temperature (Chung, et al., 2000; Zafar, et al., 2017).

2.2.3 **Pressure**

Pressure here refers to the compacting pressure, which is a vital factor that has impact on the flow properties of bulk solids. Granulated materials are subject to compaction due to vibration (e.g. during transportation), impact from a falling stream of solids (e.g. during packing), or external

loading. The increasing pressure reduces the distance between particles, thus increasing inter-particle adhesion, and causes a significant increase in critical arching dimension (Ganesan, et al., 2008).

2.3 Contact Mechanics

In a bulk powder system, particles are in contact with each other, and the various contact mechanisms can modify the interaction forces between the particles. The contact area between the particles can be affected by the material's mechanical properties, surface properties, and shape (Zafar, et al., 2017; Fu, et al., 2012; Peleg, 1977).

2.3.1 Mechanical properties of materials

Essentially, the deformation mechanism is affected by the physical characteristic of the material. The failure modes of different materials can be classified as reversible elastic, irreversible plastic, reversible viscoelastic, and irreversible viscoelastic (Tomas, 2000). These different deformations will result in different adhesion forces between the particles.

2.3.1.1 Elastic deformation

When a particle deforms elastically, the material will recover from the deformation once the applied pressure is withdrawn. The recovery can be prevented if stress is applied for a significant duration, resulting in a permanent bond due to rearrangement of molecules. The bond formed will have to resist the residual elastic strain energy trying to recover from the

deformation, and hence, such a bond does not have a high affinity of adhesion.

There are a few models for quantifying the adhesion force of the elastic contact, mainly the Derjaguin, Muller, and Toporov (DMT) adhesion theory, and Johnson, Kendall and Roberts (JKR) model.

In order to understand the adhesion force during elastic contact, it is necessary to understand the deformation mechanism. Hertz demonstrated the relationship between the penetration and the contact radius (Derjaguin, et al., 1975),

$$\delta_H(a) = \frac{r^2}{2R} \tag{2.5}$$

where δ_H is the penetration in the Hertz model, r is the contact radius and R is the particle radius. The relationship between the compression force, F_H, and the contact radius is described as (Barthel, 2008; Yap, et al., 2008),

$$F_H(r) = \frac{4Er^3}{3(1-v^2)R} \tag{2.6}$$

where E is the Young's modulus and v is the Poisson ratio. The Hertz model predicts elastic deformation of spheres without adhesion (Barthel, 2008). The contact radius, when two particles are in contact, can be estimated using the Hertz theory given by the following equation (Zhou & Peukert, 2008):

$$r^3 = \frac{R_E}{E} F_H \tag{2.7}$$

where E is the elastic modulus of the system and R_E is the equivalent radius of the two contact particles as shown in (2.8).

$$R_E = \frac{R_1 R_2}{R_1 + R_2} \tag{2.8}$$

where R_1 and R_2 are the radii of the two different contacting particles. Equation (2.7) shows that the contact area between two particles of known sizes is related to the elastic modulus (stiffness) for a given external force.

the DMT model is based on an earlier model developed by Derjaguin in 1934. The contact stresses and the gap shape are based on the Hertz predictions. The deformation of the particle is also based on Hertz contact, and it is assumed that the surfaces cannot be interpenetrated. In the earlier prediction, the normal force, F_D, is described as

$$F_D = F_H(r) - \pi R\zeta \tag{2.9}$$

(Barthel, 2008), where ζ is the adhesion energy at the contacting surface and R is the radius of the particle. From Equation (2.10), substituting F_H from Equation (2.6) and assuming the external applied load is nil (*i.e.* F_D = 0), the contact radius can be derived:

$$r \approx \left(\frac{\pi(1-\nu^2)\zeta R^2}{E}\right)^{1/3} \tag{2.10}$$

Subsequently, the pull-off force between two surfaces (spherical object in contact with a flat plane), F_{off}, was given as (Barthel, 2008; Derjaguin, et al., 1975)

$$F_{off} = -\pi\zeta R \tag{2.11}$$

This equation assumes that the adhesion energy does not increase with the contact deformations and ignores the energy of the non-contacting adhesion forces (Derjaguin, et al., 1975). Subsequently, Derjaguin derived the force acting between two surfaces in close proximity with each other without any contact, $F_{ext,}$ in the "Derjaguin approximation", as shown in Equation (2.12), which is widely used in measurements of surface forces:

$$F_{exp} = 2\pi \int_0^{+\infty} dii\sigma_z(i) \tag{2.12}$$

where $\sigma_z(i)$ is the radial distribution of surface stresses, and i is the displacement in the normal direction. By assuming that the surfaces are rigid, and ignoring the curvature impact on the surface interaction, the following equation was derived by Derjaguin:

$$F_{exp} = 2\pi R V_{int}(\delta_{pen}) \tag{2.13}$$

where V_{int} is the interaction potential, and δ_{pen} is the rigid body displacement. Following from this, by computing the Derjaguin approximation into the Derjaguin 1934 model, the compression force, F_{DMT}, is predicted in the DMT model as

$$F_{DMT} = F_H(r) + F_{ext}(r) \tag{2.14}$$

The pull-out force using the DMT model, Equation (2.15), was derived from Equation (2.11) to integrate the Derjaguin approximation (Derjaguin, et al., 1975; Barthel, 2008).

$$F_{off} = -2\pi R\zeta \tag{2.15}$$

The DMT theory still applies the Hertzian stress distribution and deformation, and the assumption made in the Derjaguin approximation. Because of this, DMT theory is only valid for small and rigid spheres (Barthel, 2008).

Unlike DMT theory, which works for rigid spheres, the JKR model is based on experiments carried out on soft rubber-like spheres. The JKR model uses an energy-transfer mechanism whereby the soft material deforms and a neck around the contact area is formed. The contact radius is formed by a transfer of work, $\zeta\pi r^2$, from the contact area. The relationship between the energy and the neck height, δ_{fp}, must then follow (Barthel, 2008; Johnson, et al., 1971),

$$2\pi r\zeta = \frac{E}{1-\nu^2}\delta_{fp}^2 \tag{2.16}$$

Using the definition of a in Equation (2.10), the neck height can be derived from Equation (2.16),

$$\delta_{fp} = \left(\pi\zeta^2 R\frac{(1-\nu^2)^2}{E^2}\right)^{\frac{1}{3}} \tag{2.17}$$

The JKR model provides the contact equation for non-adhesive contact of a flat punch,

$$F(a) = F_H(r) + F_{fp}(r) \tag{2.18}$$

where F_{fp} is the term for flat-punch force and is given by

$$F_{fp}(a) = \frac{2r\delta_{fp}E}{1-\nu^2} \tag{2.19}$$

For homogeneous elastic spheres, the JKR model uses Equations (2.7), (2.8), (2.18), and (2.19) to derive Equation (2.20).

$$F(a)_{JKR} = \frac{4Er^3}{3R(1-v^2)} - 2\sqrt{\frac{2\pi E\Gamma r^3}{1-v^2}} \tag{2.20}$$

From Equation (2.20), the pull-out force can be calculated from the minimum total force (Barthel, 2008; Krupp, 1967),

$$F_{off} = \frac{3}{2}\pi\Gamma R_{1,2} \tag{2.21}$$

where Γ is the work of adhesion and $R_{1,2}$ is the mean radius of surface curvature of both particles. $R_{1,2}$ is defined by

$$R_{1,2} = \left(\frac{1}{R_1} + \frac{1}{R_2}\right)^{-1} \tag{2.22}$$

R_1 and R_2, are the radii of the two involved particles. For a contact between a sphere and a plate, R_2 turns to infinity, and thus, $R_{1,2} = R_1$. On the other hand, for two similar particles with equal particle diameters, $2R_{1,2} = R_1 = R_2$. The work of adhesion is then described by

$$\Gamma = \gamma_1 + \gamma_2 - \gamma_{1,2} \tag{2.23}$$

where γ_1 and γ_2 are the surface energies of the contacting particles and $\gamma_{1,2}$ is the interaction energy between the contacting areas. If the contact particles are of the same material, then $\gamma_{1,2}$ turns to nil, and $\Gamma = 2\gamma$ (Zafar, et al., 2017).

Contrary to the DMT model, the JKR theory is applicable when interacting forces are large and when the material deforms more easily. Both the

DMT and JKR models predict a larger contact radius in comparison with the Hertz model. On the other hand, it was demonstrated that the JKR model results in a higher contact radius compared to the DMT model (Barthel, 2008).

2.3.1.2 Plastic deformation

During plastic deformation, the applied stress/es modify the structure of the material without it being able to recover. Plastic deformation will result in higher contact areas, which cause an increase in adhesion forces. The higher adhesion forces result in unwanted agglomeration of powder (Zafar, et al., 2017). At the elasto-plastic deformation stage, the mean pressure of the indentation will increase linearly with ln($E.a/\ \tau'_o.R$), where τ'_o is the yield strength of the particle. Subsequently, in the full plastic deformation stage, the mean pressure becomes constant (Maugis & Pollock, 1984). The mean pressure, P_m, is then equal to the hardness, H, and can be related to the yield stress and applied pressure by

$$P_m = H = \frac{P}{\pi R^2} = 3\tau'_o \tag{2.24}$$

However, a significant contribution of surface forces will result in the following relationship:

$$r^2 = \frac{P + 2\pi\ \Gamma \mathrm{R}}{\pi H} \tag{2.25}$$

The adhesion force, or the pull-out force, was found to be dependent on the type of separation, whether ductile or brittle. A brittle separation results in some reduction in the contact radius (Maugis & Pollock, 1984; Cleaver

& Looi, 2007). The adhesion force, F_{adh}, can be determined using the Rumpf approximation (Zhou & Peukert, 2008),

$$F_{adh} = F_{adh,0} + p_{vdw} f_{pl} \tag{2.26}$$

where $F_{adh,0}$ is the adhesion force in the absence of deformation, and $p_{vdw} f_{pl}$ accounts for the vdW force around the contact area created by plastic deformation. In Equation (2.26), the f_{pl} represents the contact area, p_{vdw}, describes the vdW pressure between a plate and a half-space and it can be derived using Hamaker model,

$$p_{vdW} = \frac{C_H}{6\pi a_0^3} \tag{2.27}$$

Another adhesive model due to plastic deformation was developed by Tomas (2000). The model is based on characterising the hysteresis of the force–strain curve. Hysteresis is a result of an increase in the contact area due to irreversible deformation under high normal force. The model includes the friction coefficient and time consolidation in the prediction (Zhou & Peukert, 2008; Tomas, 2000). For instantaneous consolidation,

$$F_{adh} = (1 + \kappa) F_{H0} + \kappa . F_N \tag{2.28}$$

and under time consolidation, Equation (2.28) becomes

$$F_{adh} = (1 + \kappa + \kappa_t) F_{H0} + (\kappa + \kappa_t) . F_N \tag{2.29}$$

where κ_t is a constant related to the plastic deformation between the particles under time consolidation.

Unlike the models developed to predict the contact area and adhesion force between particles, there has been no theoretical model to quantify the effect of material properties on flowability, although it has been reported that the elastic modulus of various materials (such as ibuprofen, mannitol, paracetamol DC, β-lactose, etc.) increased with its yield pressure, which is proportional to the hardness (Sonnergaard, 1999; Yap, et al., 2008). Tomas (2001) compared the plastic contact failure between the particles with the flowability of the powder by using a mathematical derivation (Tomas, 2001).

2.3.2 **Surface roughness**

Previously it was mentioned that the surface roughness of the particles can affect powder flowability (Jones, et al., 2003; Johanson, 2009). Surface asperities are shown to influence the adhesion forces between particles, as described in Equation (2.2) (Tomas, 2000). It is therefore necessary to consider the surface roughness when understanding bulk powder transformations.

In a practical powder system, the powder will have asperities and not be perfectly smooth, which influences the inter-particle interactions. The asperities on the surface of the particles can also contribute to how the particles are in contact. For example, the asperities can either be in contact with each other or they can fit into a trough of another particle. In the right arrangement, asperities can increase the separation between particles, hence reducing the adhesion force contributed by vdW (Jones, et al., 2003; Johanson, 2009).

In addition to the above, asperities can affect the capillary condensation and influence the stress exerted on the contact area (Zafar, et al., 2017). It has been demonstrated using glass beads that there is a higher water adsorption rate on rough surfaces of particles than on the smooth surfaces. The condensed moisture will increase the plasticity of the material, resulting in a higher adhesion force caused by the plastic deformation, as previously mentioned (Landi, et al., 2011; Ganesan, et al., 2008). Furthermore, as previously mentioned, moisture can lubricate the contact among particles and weaken vdW forces by increasing the distance between particles by forming liquid bridges (Crouter & Briens, 2014; Emery, et al., 2009; Landi, et al., 2011).

2.3.3 **Shape**

Similarly to the smoothness of the particles, the shape of the granules in the powder system will also not be perfectly spherical. However, most of the models mentioned above rely on the assumption that the material is perfectly spherical, or in contact with a perfectly flat surface. Mullins *et al.* demonstrated that particle geometry was found to play a vital role in the adhesion force. The contact points among particles can either be increased or decreased according to the geometry of the particles (Mullins, et al., 1992).

2.4 Inter-Particle Adhesion Force

Increasing adhesive forces between particles are the condition for undesired agglomeration to occur. The interaction can be caused by the

formation of liquid bridges, electrostatic forces, sintering, vdW forces, and recrystallisation of material. As particles are in continuous contact with each other, electrostatic forces can be neglected, unless the particles have non-conducting plasticity characteristics (Hartmann & Palzer, 2011).

2.4.1 **Liquid bridges**

The formation of liquid bridges between particles is a function of the surface tension, contact angle, particle size and shape, and the spacing of the particles. The contact angle relies on the particles' surface morphology at the point of contact. Wetting of the particles may also complicate the geometry.

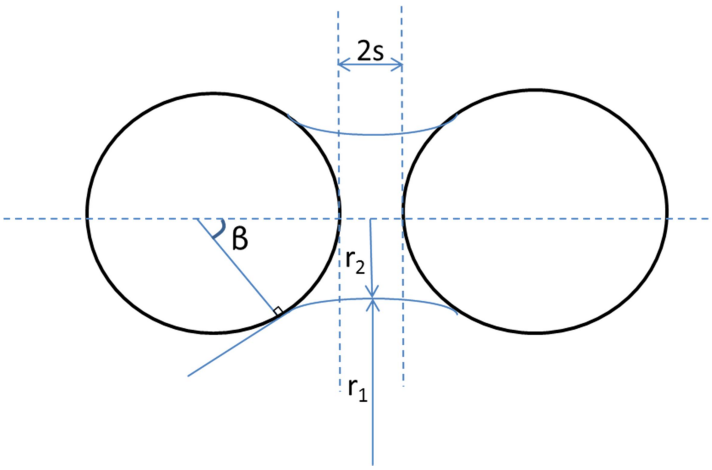

Figure 2.3 Diagram for analysis of a liquid bridge between two particles

Figure 2.3 shows two smooth spheres with radius R, separated by distance $2s$ and joined by a liquid bridge of half-angle β under perfectly wetting liquid conditions. Using the Young-Laplace equation, the pressure difference in the bridge (i.e., the pressure difference between the atmospheric pressure, P_V, and meniscus, P_L) can be equated to

$$P_L - P_V = \gamma\left(-\frac{1}{|r_1|} + \frac{1}{|r_2|}\right) \tag{2.30}$$

where γ is the surface tension of the liquid, and r_1 and r_2 is the characteristic length of the liquid bridge as shown in Figure 2.3.

Under humid air, vapour is allowed to contact a wettable surface. The surface tension and curvature will result in the condensation of the vapour. Menisci and liquid bridges in pores and particle junctions will be formed before the normal saturation value, P^{sat}, is achieved. The relative vapour pressure, P/P^{sat} is related to the curvature described by the Kelvin equation:

$$\left(\frac{1}{r_1} + \frac{1}{r_2}\right)^{-1} \equiv r_k = \frac{\gamma_{LV} V_{LM}}{R_G T \ln\left[\frac{P}{P^{sat}}\right]} \tag{2.31}$$

where γ_{LV} is the surface tension of the liquid in the vapour phase, R_G is the gas constant, r_K is the Kelvin radius, T is the temperature of the system, and V_{LM} is the molar volume of the liquid. Rearranging the equation will give:

$$\ln\left[\frac{P}{P^{sat}}\right] = \frac{\gamma_{LV} V_{LM}}{R_G T}\left(\frac{1}{r_1} + \frac{1}{r_2}\right) \tag{2.32}$$

According to the equation, capillary condensation will occur when $P_i < P_i^{Sat}$ in pores with curvature $\geq \left| 1/r_k \right|$. It will affect all porous media in contact with a wetting liquid. The cohesive behaviour observed between particles can occur at low humidity and the binding strength can increase with the humidity of the vapour.

Agglomeration by means of liquid bridges consists of three main mechanisms (Rough, et al., 2005):

- The resultant force of reduced hydrostatic forces in the liquid found in the bridge, F_{CP}.
- The surface tension force acting on the axial component at the interface, $F_{CT.}$
- The buoyancy force, which can be neglected if the particles are smaller than 1 mm.

Where

$$F_{CT} = 2\pi r_2 \gamma \tag{2.33}$$

$$F_{CP} = \pi r_2^2 (P_L - P_V) \tag{2.34}$$

In addition, the strength of the liquid bridge is affected by the amount of wetting. The amount of water in the system can be described by four different regions: pendular, funicular, capillary, and slurry. In that order, the pendular region has the least water content, and slurry has the most. In the pendular region, the number of liquid bridges formed is the highest and with adhesive strength also the highest. However, with increasing water content, the liquid fills up the pores among the particles, which results in a reduction in the bridge strength. In the slurry region, the particles are suspended and will be devoid of cohesive strength (Newitt & Conway Jones, 1958).

2.4.2 **Sintering bridges**

A sinter bridge is formed when two particles are in contact with each other, and in order to reduce the free surface area as the particles merge, molecules are transferred across the two primary particles. The bridge can also be caused by movement of materials due to diffusion and viscous flow (Seville, et al., 2000).

In order to estimate the adhesion between two particles under the sintering mechanism, a model of two similar spherical particles with diameter *R* in contact is shown in Figure 2.4.

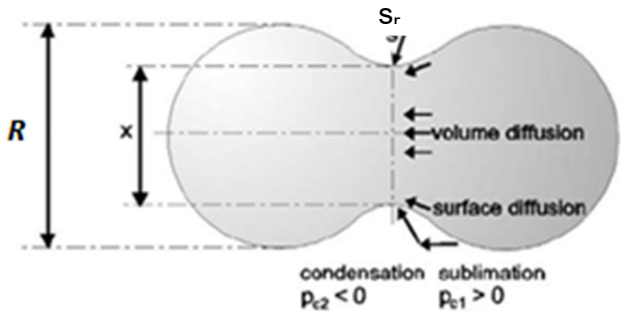

Figure 2.4 The adhesion of two particles under sintering mechanisms (Hartmann & Palzer, 2011).

In Figure 2.4, *R* is the particle diameter, *x* is the diameter of the sinter bridge, s_r is the radius of curvature between the particles, p_{c1} is the vapour pressure above the particles, and p_{c2} is the vapour pressure above the sinter bridge. The adhesion due to sintering can be determined by the ratio of the contact area between the particles and the surface area of the particle, *S.R.* (Hartmann & Palzer, 2011),

$$S.R. = \left(\frac{x}{2R}\right)^2 \tag{2.35}$$

Equation (2.35) assumes two similar prefect sphere particles.

Subsequently, the pressure difference between the two pressure points can be calculated using the Young-Laplace equation. The sintering process that occurs due to the capillary pressure difference across the point of contact can then be described using Equation (2.36) (Hartmann & Palzer, 2011):

$$p_{c1} - p_{c2} = \frac{4\gamma}{R} - \gamma\left(\frac{2}{x} - \frac{1}{s_r}\right) \tag{2.36}$$

where γ refers to the surface tension of the particles. The equation assumes two perfect spherical particles in contact with each other.

The formation of the sinter bridge is a time-dependent process, with the diameter of the bridge, x, increasing with time as shown in Equation (2.37) (Seville, et al., 2000):

$$\left(\frac{x}{R}\right)^2 = w\tau_{contact} \tag{2.37}$$

where $\tau_{contact}$ is the duration of contact between the two particles and w is described by Frenkel's equation for viscous sintering shown in the following equation (Seville, et al., 2000):

$$w = \frac{3\gamma}{2R\mu} \tag{2.38}$$

From Frenkel's equation, it is shown that the sintering mechanism is affected by the material's viscosity, μ. As a result, the consolidation rate and consolidation strength of the powder system are also a function of temperature (Seville, et al., 2000).

Alternatively, the deformation of two contacting particles by a force, F_t, can be based on the Navier-Stokes equation. With the assumption of a small contact between the particles and ignoring the changes in particle geometry during the deformation process, w, can be derived from (Hartmann & Palzer, 2011)

$$w = \frac{4}{5}.\frac{\gamma}{R} + \frac{2F_t}{5\pi R^2} \tag{2.39}$$

The above relationship between deformation and time is derived from the Hamaker summation method as shown in Equation (2.40) (Zhou & Peukert, 2008). The dispersion force, F_{Disp}, generated when the surfaces are slowly brought into contact to maintain the energetic equilibrium (among mechanical, elastically accumulated, and surface energy) is described by the JKR model (Zhou & Peukert, 2008):

$$F_{Disp} = \pi r^2 \frac{C_H}{6\pi a_o^3} \tag{2.40}$$

where the contact radius, r, is described in Equation (2.7) based on the Hertz theory. Equation (2.39) is only observed during the initial phase of the sintering process. As the surface tension and material viscosity vary with moisture content and temperature, the mechanism is constantly changing with environmental conditions. In addition, for contact between non-spherical particles, the radius of the particles is estimated from the curvature radius at the contact point (Hartmann & Palzer, 2011).

In addition, the deformation of the material will lead to an increase in cohesion between the particles, which can be due to all the

aforementioned inter-particle interactions. As the particles deform, the distance separating the centres of both materials reduces and the number of contact points increases (Hartmann & Palzer, 2011). This will also lead to an increase in vdW interactions between the particles.

2.4.3 van der Waal's force

The dispersion interactions between the atoms in two different particles due to dipole–dipole, dipole–non-polar, and non-polar–non-polar interactions are referred to as vdW forces (Seville, et al., 2000). These short-range forces are dominant in dry particulate systems and are dependent on the surface distances between the particles (Tomas & Kleinschmidt, 2009). These surface energies are caused by instantaneous fluctuation of the dipole within the atoms, which are also known as Columbic interactions. The vdW interactions between the particles are dependent on the dielectric properties of the materials and the medium between them. The interaction can be both attractive and repulsive (Martin, 2008).

With the assumption of perfectly frictionless and stiff particles that are not subject to deformation, the vdW interactions, F_{vdW}, can be estimated by Equation (2.41) (Tomas & Kleinschmidt, 2009):

$$F_{vdW} = \frac{C_H R_E}{6a^2} \tag{2.41}$$

where C_H is the Hamaker constant, a is the distance between the particles and R_E is the mean radius of surface curvature of both particles, as described in Equation (2.8). Particles attract when the Hamaker constant

is positive, while the interactions are repulsive when the constant value is negative (Martin, 2008).

2.5 Physical Storage Stability

Undesired consolidation of solid particles, *caking*, is a common phenomenon observed in many different powder systems. The caking of the powder is a critical measure of the undesirable transformation of the powder flowability to form cohesive bulk powders that possess a high level of resistance to flow. The process results in the reduction of the particles' flowability, product quality, and loss of functionality, and can cause segregation within the final product. Similarly to the flowability of the powder, this parameter is affected by many various characteristics of the powder (such as particle size, elasticity, and yield stress) and environmental conditions (such as temperature, humidity, stress, and vibration) (Griffith, 1992). The process can occur at different stages of powder production, storage, and transportation (Hartmann & Palzer, 2011).

When granulates are stored in a container, the particles are in contact with each other. Subsequently, under humid condition and stress caused by the weight of material above the bulk powders, alteration of the bonds between particles may occur. A significant increase in cohesive strength, undesired agglomeration, or caking may be the result of moisture migration, ageing, recrystallisation, or heating due to chemical instability within the powder system (Prescott & Barnum, 2000).

In addition to the above, caking is a major issue during the storage of powder in silos, where time-consolidation of the particles takes place. The consequence might be blocking of the entire silos, which will require manual mining techniques to recover the powder (Hartmann & Palzer, 2011). The quality of the powder will be further aggravated when external forces are applied to the bulk powder system, by vibration caused during transportation, or stacking of containers that deform. Fluctuation in storage condition can also exacerbate the unwanted agglomeration process (Prescott & Barnum, 2000).

The particle characteristics, such as cohesion, elasticity, hardness, degree of crystallinity, hygroscopicity, glass transition temperature, particle size, and particle shape, will also affect the tendency to undesired agglomeration (Prescott & Barnum, 2000; Aguilera, et al., 1995). Together with the effect of the external condition and the wide range of factors contributing to the storage stability, it is hard to model the behaviour of the bulk powder system during transportation, processing and storage.

2.5.1 **Caking mechanism**

Undesired agglomeration in a powder system can be caused by recrystallisation, surface wetting, and surface and field forces such as vdW forces, electrostatic and magnetic forces, and viscous flow. The interlocking of non-spherical particles can also result in caking (Aguilera, et al., 1995; Tomas & Kleinschmidt, 2009; Zafar, et al., 2017). Typically, caking is a homogenous process. However, it has been reported that

localised caking on several materials can occur, and this non-homogenous agglomeration is hard to detect (Freeman, et al., 2015).

The main mechanism responsible for the caking of water-soluble amorphous substances is sintering. The different stages of caking due to sintering are illustrated in Figure 2.5 (Hartmann & Palzer, 2011). Under the sintering mechanism, an external compressive normal force acts on a soft contact of two similar spherical particles and results in the deformation of the contact point to form a contact area. As a result, the adhesion between the two particles increases (Tomas, 2000). Eventually, brittle lumps are formed, and a stable powder cake is created (Hartmann & Palzer, 2011).

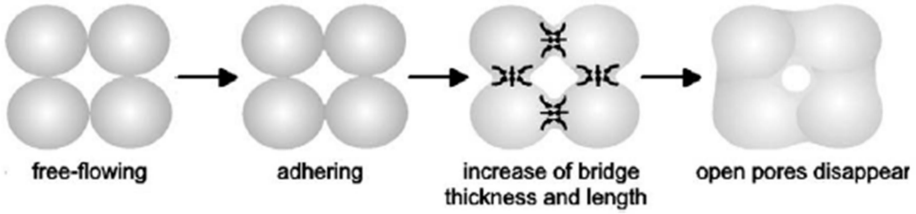

Figure 2.5. A schematic diagram of the caking process through sintering (Hartmann & Palzer, 2011)

When a cake is formed, substances with low dissolvability will lose their structure and shape due to the lack of a stabilised inner structure. Finally, this will result in an amorphous melt when the powder structure collapses. Occasionally, with compounds such as cellulose, silicate, fats or proteins, the insoluble matrix preserves the shape of the particles and the integrity of the structure (Hartmann & Palzer, 2011). The sintering mechanism requires contact for the plasticisation of both the particles' surfaces, which is a function of the viscosity. As a result, the rate of caking is greatly increased when the material is stored above its glass transition

temperature, which increases the mobility of the polymer content (Chung, et al., 2000).

Alternatively, under humid condition, caking can occur due to the formation of liquid bridges between particles. The consolidation of bridges can cause agglomeration while maintaining the high porosity of the system (Aguilera, et al., 1995). For a water-soluble powder system under humidity and temperature higher than critical conditions, the substance will partially dissolve and form low-viscosity liquid bridges. These bridges do not have a high cohesion force, but if the absorbed water evaporates, the recrystallisation of the dissolved material will create a strong bond between the particles (Hartmann & Palzer, 2011). Powder products stored in a closed system can hence still be prone to caking when temperatures fluctuate, which results in condensation and evaporation of any vapour in the system.

The vdW forces also play a role in encouraging the agglomeration process, especially for a dry powder system. However, the vdW forces can be negligible when the particles are larger than 100 μm. Particles sized over 100 μm will experience approximately more than 100 times more gravitational forces than vdW forces (Tomas & Kleinschmidt, 2009).

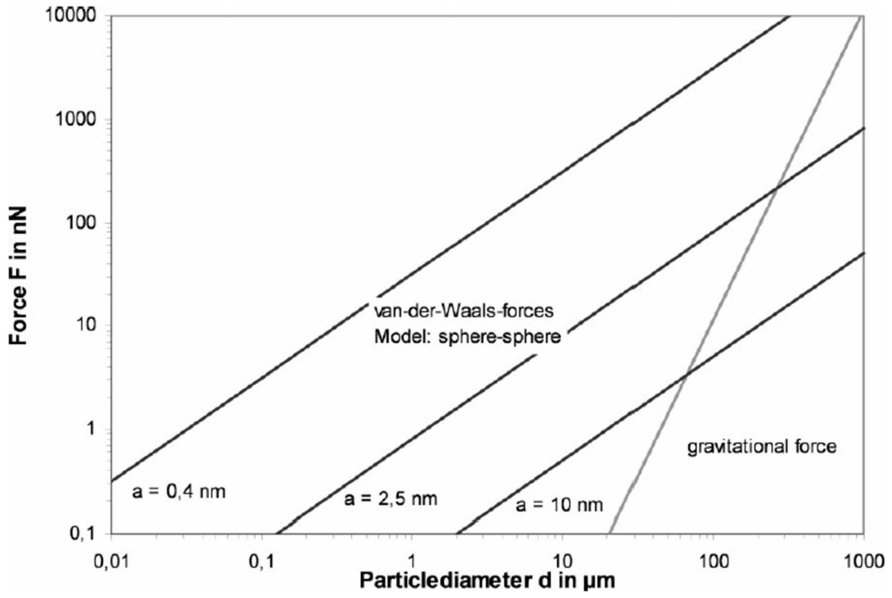

Figure 2.6 Interparticle force, vdW forces, relative to the gravitation force against the particle size of spherical SiO_2 particle (Tomas & Kleinschmidt, 2009).

2.6 Moisture Uptake

As mentioned previously, the moisture content in the powder system can cause drastic modifications to the physical and chemical properties. The aftermath of these changes is a reduction in the powder's flowability and storage stability (Mauer & Taylor , 2010). It is therefore important to understand the mechanism of water adsorption onto the surface of the particles. The simplest mathematical model of the sorption isotherm is the BET isotherm, which was named after Brunauer, Emmett and Teller in 1940, as shown in Equation (2.19).

$$\frac{P}{V(P^{sat}-P)} = \frac{1}{V_m W} + \frac{W-1}{V_m W}\left(\frac{P}{P^{sat}}\right) \qquad (2.42)$$

where V is the volume of the gas adsorbed at pressure P, V_m is the volume of monolayer of adsorbent on the surface, P^{sat} is then the saturated vapour pressure, and W is the ratio of equilibrium constants.

The model is based on the assumption that all of the possible sites for adsorption on the surface are equivalent and that all of the sites are available for higher layer adsorption. In addition, the adsorption strength and the probability of higher layer adsorption are independent of the coverage.

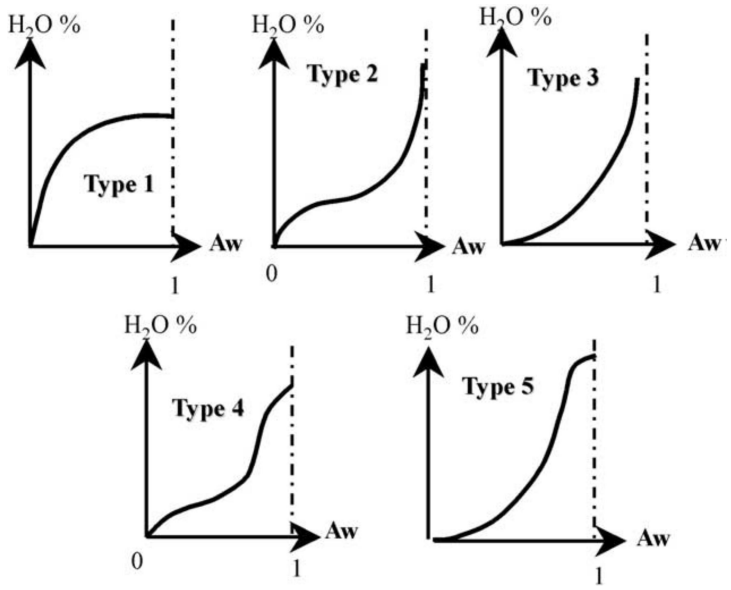

Figure 2.7 The five different types of isotherm described by Brunauer, Deming, and Teller (1940) (Brunauer, et al., 1938).

The isotherms can then be classified into five different behaviours, as shown in Figure 2.7. Type 1 is known as the *Langmuir isotherm*, which is obtained from the monomolecular adsorption of gas by porous solids in a finite volume of voids. Type 2 is known as the *sigmoid isotherm*, which describes soluble particles that exhibit an asymptotic trend as the humidity increases toward the saturation pressure. Type 3 is the *Flory-Huggins*

isotherm, which describes the adsorption of a solvent or plasticiser above the glass-transition temperature. The Type 4 isotherm accounts for the adsorption of a swellable hydrophilic solid until the maximum of hydration of sites is achieved. Lastly, Type 5 is the *BET isotherm*, in which multilayer adsorption takes place (Rhodes, 2013).

There are four types of liquid state, as shown in Figure 2.8. Depending on the amount of liquid present between groups of particles, the liquid state can be classified as i) pendular, ii) funicular, iii) capillary, or iv) droplet.

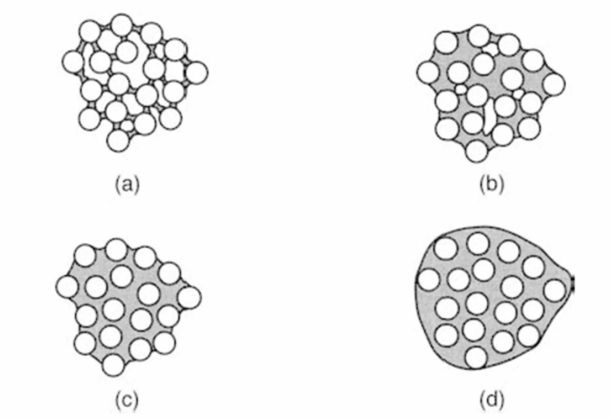

Figure 2.8. Different stage of wetting in a powder system (Rhodes, 2013)

Vapour adsorption behaviours are very useful for predicting caking. A wet surface can cause plasticisation and sometimes dissolution when the surfaces contain amorphous materials. Drying can also occur after wetting, which will form solid bridges leading to unwanted agglomerate.

On the other hand, the particles are also prone to the phenomenon known as deliquescence, whereby solids transform into solution, which occurs at a specific relative humidity (RH_0). This phenomenon is typically observed with food ingredients such as salts, sugars, organic acids, and vitamin C

(Lipasek, et al., 2012). The deliquescence point will also be lowered if two or more deliquescent materials are in contact with each other. The new RH_O at which the deliquescence occurs will be lower than any of the RH_O of the individual components. The lowering of the RH_0 can be explained by using the Gibbs-Duhem equation, in which the water activity of a saturated solution of one component will decrease as a second component is added, until the precipitation of component 2 occurs (Mauer & Taylor , 2010).

2.7 Improvement in Storage Stability and Flowability

As previously mentioned, agglomeration of fine particles to increase the particle size can be applied to improve the flowability of the powder. In addition, flow additives and coating have also been proven to be capable of improving the flowability of the powder.

2.7.1 Flow additives

Alternatively, flow agents can be added into the powder to reduce the inter-particle forces. This will enhance the flowability by reducing the cohesiveness and compressibility while increasing the bulk density. Chemicals such as silicates, stearates, and phosphates can be used as flow agents. It has been found experimentally that flowability was enhanced when the concentration of flow conditioners was less than 1%, while increasing concentration of flow agents above 1% had an insignificant impact on the flowability (Onwulata, et al., 1996). Nanoparticles, surface-active additives, and polymers can also be added as guest particles to improve the flowability of larger particles. The

additives added to the powder system reduced the effect of vdW forces in dry powder by increasing the distance between the particles (Tomas & Kleinschmidt, 2009).

2.7.2 **Coating**

the coating process can be used to modify the surface properties of the core particles. These modifications can improve the flowability and storage stability of the core material (Mei, et al., 1997). Furthermore, this technique can add functionalities, such as the controlled release of the desired chemical and an improvement in the aesthetics of the product.

Coating materials, such as those already mentioned as flow additives, can be attached to the core particles. By doing so, the coated particles increase the distance between particles by separating the particles, thus reducing the inter-particle interaction due to vdW forces (Blumel, et al., 2015). The coated materials can also alter the physical property of the core material.

This method can also be used to alter the hygroscopicity of the particle surface. This can also achieve improvement in storage stability by reducing the amount of surface moisture absorbed. Surface alteration using surface-active additives can also increase the void between the particles (Tomas & Kleinschmidt, 2009).

2.7.3 **Granulation**

Granulated detergent is made by agglomeration of particles into larger aggregates in order to improve its flowability, reduction of dust, and

cohesive properties with other materials, which improves product composition consistency as compared to the initial powder (Chateau, et al., 2005). A tumbling drum, a fluidised bed and a high-shear mixer are items of equipment that can be used for the process wherein the liquid binder is sprayed onto the particles (Iverson, et al., 2001). However, this method lengthens the manufacturing process, which causes an increase in production costs. Furthermore, it contributes to processing problems such as decreased powder tabletability, poor active release, and slower powder dissolution when applicable (Chattoraj, et al., 2011).

2.8 Particle Characterisation Techniques

2.8.1 **Mechanical properties**

As mentioned above, the mechanical strength of the undesired agglomerate is a strong function of the inter-particle interaction, and part of the mechanical properties of the materials. Furthermore, granules are also subject to attrition and/or fragmentation processes, and hence it is important to understand the mechanical properties of single particles and the correlation of individual properties to a bulk system (Yap, et al., 2008; Adams & McKeown, 1996).

2.8.1.1 Characterising Single Particles

In order to predict the deformation behaviour, mechanical properties such as Young's modulus and yield stress are important parameters to be known. The mechanical properties of the particles can be determined using diametrical compression, a technique that compresses a single

particle between two rigid platens. For micro-particles, micromanipulation and nano-indentation techniques can be used to investigate the mechanical properties (Yap, et al., 2008; Israelachvili, 2011). These methods will generate a stress/strain or force/displacement curve. The data can then be used to obtain the Young's modulus based on the Hertz equation as shown in Equation (2.43) (Marigo, et al., 2014).

$$F = \frac{4E\sqrt{R}}{3(1-\nu^2)}\delta^{\frac{3}{2}} \tag{2.43}$$

where *E* represents Young's modulus, *v* is the Poisson ratio of the particle, and *δ* is equivalent to half of the total displacement. The hardness of the material, *H*, can be determined from the gradient of the linear plastic region in the force/displacement curve using

$$F = 2\pi HR\delta \tag{2.44}$$

However, this equation underestimates the hardness when the contact radius, *r*, is roughly more than 20% of the particle radius. This usually occurs under high strain, also known as the finite deformation region (Yap, et al., 2008).

The nominal strength, τ_{0S}, can be determined from the first maximum force in the compression process, F_{max}. The nominal strength registers the pressure of the particle fracture during the compression. The nominal strength can be derived from

$$\tau_{0s} = \frac{4}{\pi d^2}F_{max} \tag{2.45}$$

where *d* is the diameter of the particle (Adams & McKeown, 1996).

Characterising a single particle's mechanical strength requires a large amount of time, and a wide range of parameters will affect the experiment results. For this reason, a confined uniaxial compression of agglomerate beds is preferred (Adams & McKeown, 1996).

2.8.1.2 Characterising Bulk Particles

As previously mentioned, a material's mechanical properties can also be investigated using a uniaxial compression test on the bulk powder (Samimi, et al., 2005; Yap, et al., 2008), including loading and unloading experiments. While loading, the force results in elastic and plastic deformation. Subsequently, while unloading, the material will recover from the elastic deformation only (Molenda & Stasiak, 2002; Oliver & Pharr , 2004).

When compressing bulk powder, three different mechanisms can be observed. Firstly, the particles will slide and rearrange without any deformation or breakage. However, this does not apply to soft or weakly structured particles where they might deform or fracture during the first stage. Subsequently, the particles undergo extensive plastic deformation and then fragmentation under the high normal stress. This process will reduce the interstitial volume until the bed porosity reaches its minimum value. At the minimum void, the material will exhibit some elastic behaviour under the high pressure (Samimi, et al., 2005). However, the

different stages of the process overlap each other, which makes it hard to distinguish the different mechanisms that are in play (Sonnergaard, 1999).

The compression process can be described using empirical models, such as those of Heckel, Walker, Kawakita, and Adams, to derive the hardness of the material and the apparent elastic modulus (Yap, et al., 2008).

Heckel Model

Heckel's equation deploys a first-order chemical reaction relationship between the bed porosity and the bed pressure (Samimi, et al., 2005; Sonnergaard, 1999),

$$-\frac{d\varepsilon}{d\sigma} = K\varepsilon \tag{2.46}$$

where ε is the bed porosity, σ is the applied stress, and K^{-1} is the Heckel parameter. From the equation, it can be seen that the rate of decompression is proportion to the bed voidage. This means that a powder bed with high porosity will be easier to compact than one with low voidage. As the voidage decreases during compression, the rate of compression decreases as the rate of change in porosity declines. The Heckel parameter is used to describe the material's ability to deform plastically and is inversely related to the hardness, H, and the uniaxial yield stress, σ_o (Yap, et al., 2008).

$$K \propto \frac{1}{3\sigma_o} \propto \frac{1}{H} \tag{2.47}$$

By letting initial bed porosity be ε_i, Equation (2.47) can be integrated to

$$\ln\frac{1}{\varepsilon} = \ln\frac{1}{\varepsilon_i} + K\sigma \tag{2.48}$$

where ε is the porosity at the applied stress. By replacing the bed porosity with the relative density, ρ^*, and substituting the term $ln(1/\varepsilon_i)$ by a constant parameter, C, Equation (2.48) becomes

$$\ln\frac{1}{1-\rho^*} = C + K\sigma \tag{2.49}$$

Although the Heckel equation has been widely used, especially in the pharmaceutical sector, it has been shown that the derived parameters are particularity sensitive to small variations in the particles' property parameters during the experiment, especially the density. Moreover, for the same material, different K^{-1} values have been reported in the literature. This is due to the different compaction pressures used under different experimental conditions (Sonnergaard, 1999).

Kawakita Model

The Kawakita equation, Equation (2.50), is another empirical model used.

$$\frac{\sigma}{h_0} = \frac{1}{ab} + \frac{\sigma}{a} \tag{2.50}$$

In the equation above, a and b are both constants, where a describes the initial bed voidage and b is related to the fracture stress of the single particles in the bulk powder system. The constant b was found to be related to the nominal strength, τ_{0s}, by

$$\frac{1}{b} = k_2\tau_{0s} \tag{2.51}$$

where k_2 is a proportional constant (Adams & McKeown, 1996).

In addition, h_0 is the degree of volume reduction using the height at the applied stress, h, as compared to the initial height, h_i. The correlation is

$$h_0 = \frac{h_i - h}{h_i} \tag{2.52}$$

Adams Model

On the other hand, Adams proposed a model based on an idealised set of particles arranged in a uniform manner. By using the Mohr-Coulomb macroscopic failure criterion, Adams demonstrated that

$$dP = -\frac{K_1 \tau dh}{h} \tag{2.53}$$

where K_1 is a constant and τ is the shear failure stress. Equation (2.53) can be integrated to derive Equation (2.54).

$$\ln P = \ln\left(\frac{\tau'_o}{\alpha'}\right) + \alpha' \varepsilon_n + \ln(1 - e^{-\alpha' \varepsilon_n}) \tag{2.54}$$

In this equation, τ'_o is the apparent strength of the single particles and α' is the apparent coefficient of friction. The natural strain in the packed bed, ε_n, is given as shown in Equation (2.55) (Yap, et al., 2008).

$$\varepsilon_n = \ln(\frac{h_i}{h}) \tag{2.55}$$

At high strain, the last term, $ln(1 - e^{-\alpha' \varepsilon_n})$, becomes negligible as the tend to zero, and a linear relationship can be established (Yap, et al., 2008).

2.8.2 **Flowability**

The flow behaviour of powders has systemically high importance in the industry, as poor flow performance can cause poor quality product or halts

in production. For this reason, a reliable technique for quantification of the flow performance is desired (Freeman, 2007). The measurement will have to account for the bulk particles' physical characteristics (such as density) which will affect the flow behaviour.

Measuring the angle of repose, α_M, is a simple way of characterising flowability where a smaller value of α_M represents a better powder flowability (Tomas & Kleinschmidt, 2009). Free-flowing powder will display an angle of repose less than 40° (Aguilera, et al., 1995).

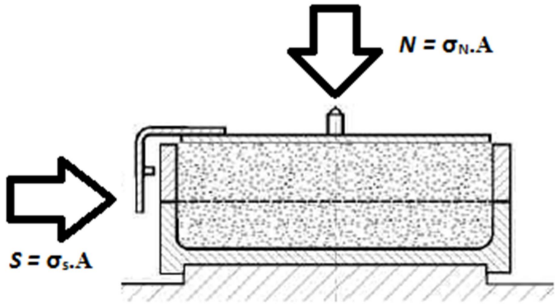

Figure 2.9 Depiction of a Jenike shear cell (Rock, 2006)

Alternatively to the angle of repose, a Jenike shear cell, shown in Figure 2.9, was developed in the early 1960s to quantify the flowability using the Mohr-Coulomb criterion. The shear cell works by applying a normal stress, σ, on the cell and deriving the maximum shear stress, τ_{max}, for the consolidated powder to fail. A set of data is obtained by applying a range of normal forces on identically pre-consolidated samples to acquire a set of the corresponding shear stress data. This relationship between the normal stress and strain can be plotted to derive the yield locus that

represents the bulk density, ε, of the pre-consolidated samples (Rock, 2006).

In the Jenike shear cell, the bulk material will be sheared in two steps: pre-shear and systemic shear. In the first step, the sample is made to flow steadily under a normal stress. Subsequently, the shear stress is reduced to nill and the normal stress is decreased to less than σ, and the bulk sample is sheared again (Rock, 2006).

Table 2.1 The flow index and its corresponding flow behaviour (Schulze, 2006)

Flow Function	Flow Condition
$ff_c < 1$	Not flowing
$1 < ff_c < 2$	Very cohesive
$2 < ff_c < 4$	Cohesive
$4 < ff_c < 10$	Easy-flowing
$ff_c > 10$	Free-flowing

The yield locus represents the critical flow condition, where the flow of the powder is not accompanied by a change in bulk density (Martin, 2008). As the bulk density of the sample increases, the yield loci move upwards due to the higher shear stress required for the consolidated particles to fail. The obtained set of yield loci can be used to derive the unconfined yield strength, σ_C, and the major consolidation stress, σ_1. The experiment is repeated with a range of different pre-consolidated bulk densities. By plotting σ_C against σ_1, the flow function, ff_c, can be attained from the plot. The relationship between the flow index and flow behaviour is shown in Table 2.1 (Rock, 2006).

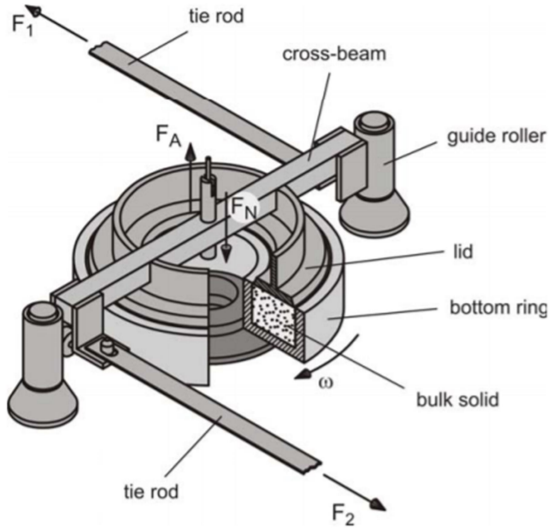

Figure 2.10 A schematic of a Schulze ring shear-cell tester cell (Schulze, 2011)

A Schulze ring shear tester (shown in Figure 2.10) is an alternative shear cell test to Jenike's which applies a similar measurement concept. The main difference is the involvement of a rotational axis, and the bulk solid is sheared by the rotation of the annular lid using the tie rod. Furthermore, the ring shear tester is capable of completing a yield locus with one specimen measured. This is achieved by increasing the pre-shear pressure again after the sample is sheared to failure.

The yield locus can be further analysed using Mohr's circle. Each point of the yield loci represents the stress applied for the powder to fail. The tangent to all the Mohr's circles thus represents the stress condition under which the powder will flow. The flowability of the material is best described with the effective angle of internal friction of the solid, θ. Although θ is not a real physical angle, it is the ratio of shear stress to normal stress for a free-flowing solid. The major and minor principal stresses on the element, σ_1 and σ_2 respectively, can be expressed by θ:

$$\frac{\sigma_1}{\sigma_2} = \frac{1 + sin\theta}{1 - sin\theta} = constant \tag{2.56}$$

It has been demonstrated that the ring shear cell tester developed by Dietmar Schulz has better reproducibility, is easier to operate, is less time-consuming, and eliminates the influence of the operators (Schulze, 2011). However, this piece of equipment is limited to powder-sized particles (Martin, 2008).

The compressibility can also be determined using a tapping technique, either manually or by mechanised tapping. The Hausner ratio, *HR*, is used as an indicator of the inter-particle friction, where the material exhibits a Geldart Type C property when *HR* > 1.40, and Type A when *HR* < 1.25 (Rhodes, 2013). The Hausner ratio is the ratio of the freely settled bulk density, ρ_B, to the tapped bulk density, ρ_T, of the material.

$$HR = \frac{\rho_T}{\rho_B} \tag{2.57}$$

The Kawakita equation can also be described by using a tapping technique:

$$\frac{N}{\varepsilon} = \frac{N}{a} + \frac{1}{ab} \tag{2.58}$$

where *N* is the number of taps, *b* and *a* are constants, and *ε* is the measure of compressibility by the change of voidage, given by

$$\varepsilon = \frac{V_O - V_N}{V_O} \tag{2.59}$$

where V_O is the initial volume of the bulk material and V_N is the volume of the material after *N* number of taps. The voidage in Equation (2.58) is the

same as the one mentioned in Equation (2.46), where Equation (2.46) uses the change of height of the powder bed during compression. The constant *a* is related to the particle size, compatibility, porosity and fluidity of the bulk, whereas constant *b* is related to the ease of tapping compression. 1/*b* can also be related to inter-particle forces that resist reduction in volume, as mentioned previously (Yap, et al., 2008; Rough, et al., 2005). Theoretically, the Kawakita constant, *a*, obtained from tapping test should be equivalent to the compression test when the packaging is similar. On the other hand, b^{-1} obtained from Equation (2.58) will be dimensionless while from Equation (2.50), b^{-1} will has a unit of [Pa].

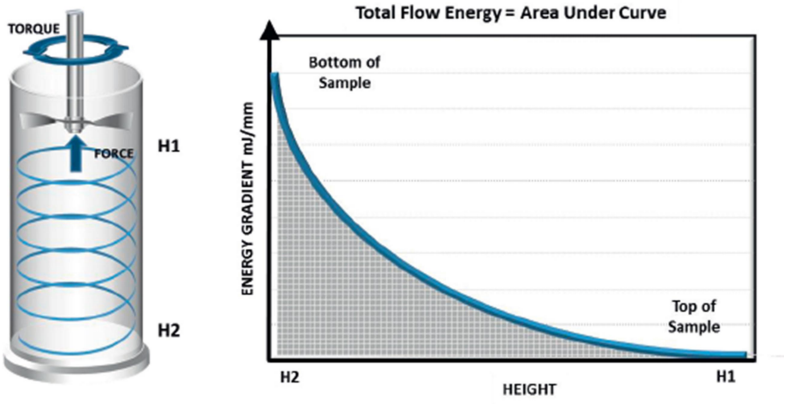

Figure 2.11 The schematic and curve used to calculate the total flow energy (Freeman, et al., 2015)

In addition to the above methods, the FT4 powder rheometer, developed by Freeman Technology, can be used to measure the flowability of the powder. It uses the measurement of flow energy of the bulk sample to quantify the caking behaviour. The design of the apparatus is shown in Figure 2.11. The degree of caking is analysed by evaluating the resistance that a specially shaped twisted blade sustains while passing through the

bulk sample along a prescribed path. Measurements are taken before and after the caking process, and the required torque and force are recorded to derive the total flow energy, as shown in Figure 2.11. The sample can be pre-conditioned under different environmental conditions before the testing. This method can be used to identify non-homogeneous caking behaviour.

2.8.3 **Storage stability**

The importance of the quantification of the powder storage stability is crucial in the industry for ensuring that the intermediate or final product quality remains consistent. There are many test methods available, including shear cell, uniaxial compression, tensile testing, ICI caking tester, creep testing, penetration testing, sieving, and environment uniaxial caking testing (Calvert, et al., 2013).

Schulze's ring shear-cell tester can be used to examine the caking behaviour of the particles. The test involves a customised shear-cell tester, which can be placed in an environmental chamber. Subsequently, the shear cell can be removed from the chamber and be placed in the ring tester, where the flowability of the wetted powder can be determined (Schulze, 2006).

In addition to the above, the uniaxial compression test can be used to investigate the storage stability of the powder. This method uses a confined wall to compact particles in order to reduce the voids and to create contact points between particles (Hart, 2015). Subsequently, the

caked powder bed is placed under an unconfined uniaxial compressive stress for the powder bed to fail, as shown in Figure 2.12. The unconfined yield strength obtained can be related to the cohesive force between the particles as the particles are made to contact each other. The method can be modified to investigate the effect of time consolidation and environmental conditions on the caking mechanism (Calvert, et al., 2013).

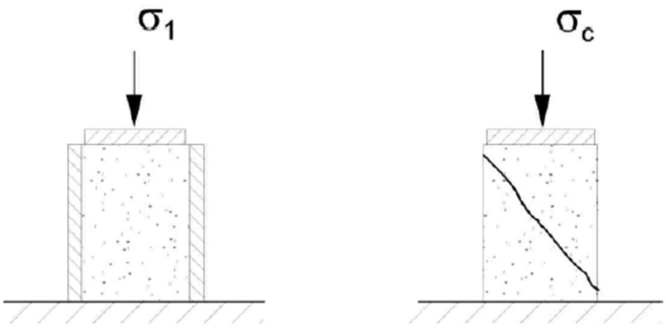

Figure 2.12 Uniaxial tester schematic (Rock, 2006)

Another method used to determine the unconfined yield strength of a bulk material is shown in Figure 2.13. The material is pressed into a tablet using a die, and the tablet is placed under a punch to obtain the force required for the tablet to fail. Using Equation (2.37), the consolidation strength, σ_c, of the tablet can be determined using the compression method shown in Figure 2.13.

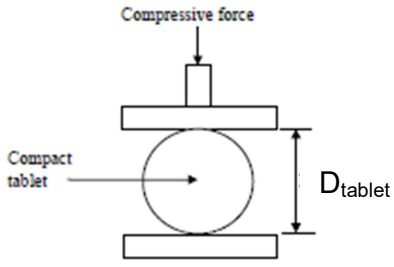

Figure 2.13 Illustration of a tablet compression method (Hart, 2015)

$$\sigma_c = \frac{2\tau}{\pi D_{tablet} t} \tag{2.60}$$

where τ is the force required for the structure of the tablet to fail, t is the tablet thickness, and D_{tablet} is the diameter of the tablet.

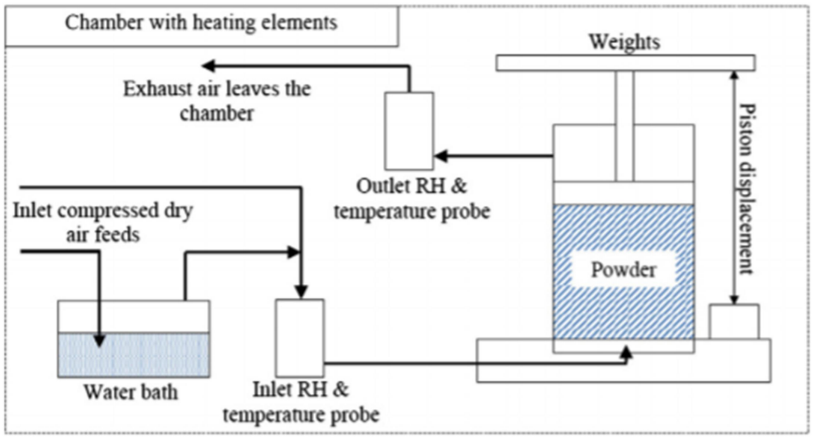

Figure 2.14 Schematic of the environmental caking rig (Calvert, et al., 2013)

Alternatively, an environment uniaxial testing rig, shown in Figure 2.14 can be used to investigate the storage stability of the powder. This technique builds on the uniaxial compression test that consolidates the powder in the environmental chamber with consistent compressive stress for a specified duration (Weigl, et al., 2006). Unlike a typical uniaxial compression test, the environmental uniaxial caking tester involves three different components: a heating element, production of conditioned air, and a consolidation rig in a chamber. Second humidity and temperature indicators were also installed after the consolidation rig to measure the moisture uptake by the consolidated powder bed. A weight was placed on the powder bed and was consolidated with constant conditioned air to

pass through the rig. The unconfined yield stress was then determined to represent the storage stability of the sample (Calvert, et al., 2013).

2.9 Conclusions

The flow behaviour of adhesive powders can cause processing and storage problems in many different industries. In this literature review chapter, the parameters that contribute to the flowability of powder are presented. It has been demonstrated that there are many factors that affect powder flow behaviour. Although several models have been developed to aid understanding of the flowability of powders, the complexity of powder systems has made the prediction of flow behaviour difficult. In order to understand the deterioration in powder flowability, the various mechanisms that cause a reduction in flowability of the powder have been discussed together with a description of the adhesion that the particles will experience. The moisture uptake behaviour of material is also discussed in this chapter.

Furthermore, this chapter also describes the various techniques used to quantify the mechanical properties, flowability, and storage stability of powders. The different models used to model bulk compression are described, together with the models used to investigate single-particle compression.

Chapter 3. Materials and Methods

In order to enhance flowability and storage stability, it was essential to study the particle characteristics of the raw materials and to understand how they affect the flowability and physical stability. Flowability was quantified with a Schulze's ring shear tester, while storage stability was analysed using a uniaxial compression test. Hardness was tested using a bulk confined compression test, while the hygroscopicity of the particles was investigated using a gravimetric technique. A single-particle compression test was also carried out to investigate the mechanical properties of the powder. In addition, the particle size, shape, density, and surface roughness were also investigated. These different characteristics of particles were then related to the flowability and the physical stability of the powder.

The raw surfactant powders were then coated with different materials in a fluidised bed coater. The coated products were subsequently characterised and compared. The coverage of the coating materials on the surface of the raw materials was also quantified. In this chapter, the details of the materials used, experimental techniques, and data analyses used are described.

3.1 Materials

Highly concentrated surfactants, HiLAS 33 and HiLAS 70 (linear alkylbenzenes), with LAS concentrations of 33 wt% and 70 wt%

respectively, were supplied by Procter & Gamble Mechelen (Antwerpen, Belgium). These particles were used as the adhesive and core particles. The aim of this project was to ultimately enhance the flowability and storage stability of HiLAS 70. The particles' characteristics were investigated and will be presented in Chapter 4.

Potassium chloride, sodium chloride, sodium sulphate, and EW base, also known as Sokalan CP 5 (acrylic acid and maleic anhydride polymer), were used as coating materials for the project. The potassium chloride was supplied by VWR Chemicals (Lutterworth, UK), while sodium chloride and sodium sulphate were supplied by Fisher Scientific (Loughborough, UK). Finally, the EW base, supplied by Procter & Gamble Technical Centres Ltd, was produced by BASF (Ludwigshafen, Germany) as Sokalan® CP5.

3.2 Preparation of Raw Material

The particles were sieved using test sieves (Retsch, UK) into four different size range: i) 100–212 μm, ii) 212–355 μm, iii) 355–500 μm, and iv) > 500 μm. Surfactant powder with sizes ranging from 212 to 355 μm was used as the core particles in all of the coating experiments. This was in an attempt to eliminate the vdW effect on the powder, as it was reported that the gravitation force of the silica powder overcame the vdW force when the size was greater than 100 μm (Seville, et al., 2000).

3.3 Particle Size and Shape

The particle size and shape were analysed using an image analysis sensor, QICPIC (Sympatec, Germany), whereby images were taken at a rate of 100 per second, with more than 50,000 particles analysed from one sample. The 10th percentile particle size of equivalent spherical volume ($d_{v,10}$), mean radius, Sauter mean diameter (d_{32}), and sphericity of the particles were determined using this method to represent the bulk sample size and shape. While d_{32} is defined by the average diameter of a spherical particle with the equivalent surface-to-volume ratio as the sample, the sphericity was determined by the ratio of the surface area of the sample particles to the surface area of the spherical particles of the same volume. Subsequently, r_{mean} was derived from half of the d_{32}. On the other hand, the range of the particle size distribution was calculated using Equation (3.1) (Saw, et al., 2013):

$$Span = \frac{d_{v,90} - d_{v,10}}{d_{v,50}} \tag{3.1}$$

where $d_{v,90}$, $d_{v,50}$, and $d_{v,10}$ are the particle size representing the 90th, 50th, and 10th percentiles of the particle size (based on volume distribution) respectively.

3.4 Particle Density

The absolute particle density was measured using helium pycnometry based on AccuPyc 1330 (Micromeritics Ltd, UK). The technique applies the gas displacement method in order to accurately determine the volume,

which is then translated into density. Particle density can be characterised into apparent, envelope, and tapped-bulk density. The gas pycnometer determines the apparent density of the particles by using helium gas.

The experiment was started by zeroing the balance (Sartorius GMBH Gottingen, Germany) with the sampling cup on it. The balance had a sensitivity of 0.0001 g. The sample was then loaded into the sampling cup, roughly half-filled, and the mass of the sample was measured before entering the pycnometer system.

The analytical results were obtained by applying the gas displacement method in order to accurately determine the volume, which was then translated into density. The inert gas, helium, will rapidly fill the void of the sample through the pores as small as one angstrom in diameter. Subsequently, helium was introduced into the chamber before being discharged into another chamber. The pressure measured during the discharge was used to derive the volume of the sample's solid phase, which was then used to calculate the particle density. Five analytical cycles were conducted for each sample.

The bulk sample bed voidage, ε, was derived from Equation (3.2) (Lozano, et al., 1983; El Hagrasy, et al., 2013). The initial bulk density obtained from a ring shear tester RST-XS (Dietmar-Schulze, Germany) was used as the bulk density, ε, of different particle samples. The particles were poured freely into a cell of known volume. The calculation was done by assuming that the density of air is negligible.

$$\varepsilon = 1 - \frac{\rho_{bulk}}{\rho_{particle}} \tag{3.2}$$

where $\rho_{particle}$ is the density of the particle.

3.5 Hygroscopicity

In order to obtain the isotherm of the powders, a dynamic vapour sorption (DVS) unit (Surface Measurement Systems, UK) was used. Dynamic vapour sorption is a gravimetric technique that measures differences in mass under different conditions. A schematic of the equipment is shown in Figure 3.1.

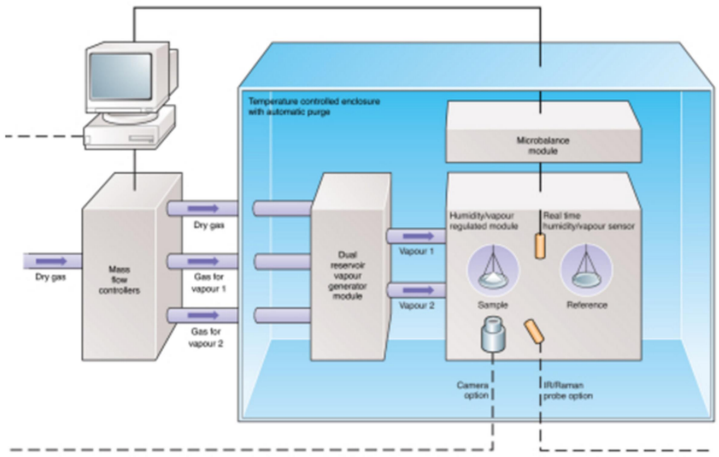

Figure 3.1 Schematic of a DVS (Sun, 2011)

The sample was placed in the sample basket after zeroing the balance. The initial weight of the sample placed in the basket was then inputted into the system. Before the samples were put under increasing relative vapour pressure from 10% to 90% with 10% intervals under 25˚C, the samples were dried under close to 0% relative vapour pressure until there was less

than 0.001% change in the mass per minute. The dried weight was then used as the reference weight for further analysis. The samples were then dried from 90% to 10% relative vapour pressure with 10% interval to complete an adsorption and desorption cycle.

3.6 Surface Roughness

An Interferometer (MicroXAM2,KLA-Tencor, USA) was used to characterise the surface topography of the samples. This technique divides a main beam of light into two, one of which is reflected onto the sample and the other in a mirror as a reference. Both reflections end up in a charge-coupled device detector where the beams cross each other to create white and black bands, known as fringes. These fringes form an interferogram that can be converted into a topographic map of the particle. A piezo-electric transducer can be added to the system to increase the amplitude of the measurement (Breakspear & Smith, 2004). The images were processed using a scanning probe image processor, developed by Image Metrology (Denmark), and a correlation, sphere fit, was used to correlate the plane of the particle surface. The surface roughness was described using the roughness surface average, S_a, and 30 images of each sample were taken and analysed to ensure the repeatability of the results.

3.7 Microscopy

A Hitachi analytical table-top scanning electron microscope (SEM) TM3030 (Hitachi, Japan) was used to obtain the images of the coated and uncoated samples. The particles were placed on the specimen stage, and a high level of vacuum (10^{-3} to 10^{-4} Pa) was created in the chamber. The images of the particles were created by firing an electron beam with 15 kV of energy from the electron gun onto the surface of the particles, and the scattered electrons from the specimen were detected by the collector system, or the secondary electron system. A condenser lens and an objective lens were placed under the electron gum to create a fine electron beam, which was required for the technique (JOEL, 2009).

Three different types of signals were generated: secondary electrons, back-scattered electrons, and X-rays from the specimen. The secondary electrons were used for quick, clear imaging as they were emitted from the atoms occupying the top surface. On the other hand, back-scatter electrons were the primary beam electrons emitted from the atoms in the sample, which were used to differentiate the different elements in the specimen. Lastly, the X-rays were the product of the interactions between the primary beam and the atoms caused by shell transitions. The energy characteristic and intensity of the reflected X-rays were used to identify and quantify the composition of each element on the surface of the sample. The X-rays can be detected using an energy dispersive detector. This technique is also known as energy-dispersive X-ray spectroscopy (EDX)

and was used to investigate the different chemical elements on the surface of the particles (Goldstein, et al., 2003).

3.8 Coverage

The coverage of the coating material on the core material was quantified using an SEM coupled with EDX as mentioned before. The cross sections of the coated particles were prepared for the imaging by placing the particles in a mould of 10 mm in diameter and 15 mm in height. The epoxy resin was then introduced into the mould and allowed to cure overnight. When the epoxy resin (Sigma-Adrich, UK) had cured, the mould was polished with sandpaper (starting with grit 60, then grit 100, and finishing with grit 320) until the cross section of the particles was exposed. This was ensured by visually checking them under an optical microscope. The image of the cross sections was taken and analysed using ImageJ by measuring the total perimeter of the particles and the perimeter that was covered by the coating material. The area coverage of the material was then derived from the square of the ratio of the covered perimeter to the total perimeter.

3.9 Hardness Test

3.9.1 Bulk-powder compression

An Instron MicroTester 5848 (Instron, UK) was deployed to determine the hardness of the samples. The load cell, 2530–100 kN, manufactured by Instron (UK), was used. The resolution of the load cell is 0.2 N with 0.25%

accuracy. Four different cylindrical moulds with aspect ratios of 0.1, 0.2, 0.3, and 0.4 (1.2 mm, 2.4 mm, 3.6 mm, and 4.8 mm) respectively were made for this purpose. The powder was loaded freely into the mould without any packing. The excess powder was scraped off carefully to ensure consistency in the voidage across all tests. The particles were then subjected to compression as the punch moved downwards at a rate of 0.1 mm min^{-1} until the particles had exhibited an irreversible plastic deformation characteristic (rapid increase in force over displacement). The compressed sample was subsequently extracted from the mould and weighed using a scale (OHAUS, USA) with a sensitivity of 0.001 g.

Subsequently, the collected data on applied stress versus displacement were fitted to the derived Adams, Kawakita, and Heckel equations, using Equations (2.31), (2.27), and (2.26) respectively, to obtain the coefficient of friction, α', and the apparent strength of the particles, τ_o', the a constant of the Kawakita model, the Kawakita parameter, b^{-1}, and the Heckel parameter, K^{-1}.

3.9.2 **Single-particle compression**

The mechanical properties of the single particles were examined using a micromanipulation technique. Firstly, a cylindrical probe of 1 mm in diameter was polished to a flat surface, which was used to compress the single particles. The probe was then attached to a force transducer with a sensitivity of 4.48 mN V^{-1}. The powder was then placed on the stage of the manipulation rig and the probe was positioned above a single particle with the help of an optical microscope. The probe was moved down slightly to

be in contact with the particle to ensure that the particle was directly under the probe.

After positioning the probe above the particle, the equipment was given the command to compress the particle at a speed of 2.07 μm s^{-1} (which is almost the same speed used for the bulk compression) and to travel downwards by 25 μm. The force versus sample time/displacement data was collected and was then fitted to Equations (2.20) and (2.21) to calculate the Young's modulus and the hardness of the single particle respectively.

3.10 Coating Process

Figure 3.2 An image of a Glatt fluidised bed

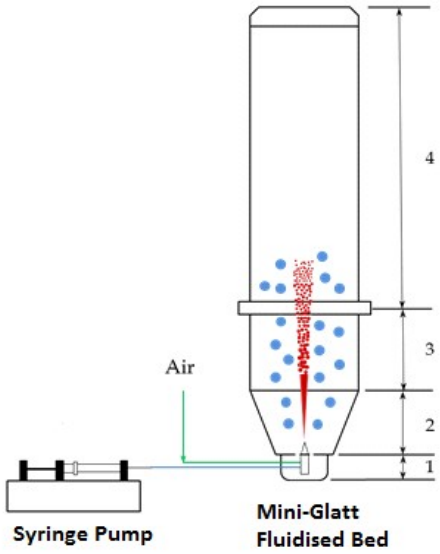

Figure 3.3 Schematic of a fluidised bed. 1-Lower plenum, 2-product container, 3-fluidised zone, 4- filter house

A Glatt® mini fluidised bed coater, as shown in Figure 3.2, was used for the coating process. The equipment can be set up into three different types of arrangement: top spray for the granulator process, bottom spray for the Würster Process, and tangential spray for the rotor process. Bottom spray is typically used for coating, and hence in this experiment, bottom spray was selected (Vesey, et al., 2014). The fluidised bed consists of four different parts: a lower plenum, a product container, a fluidised zone, and a filter house, as illustrated in Figure 3.3. An atomising nozzle with a diameter of 0.5 mm was placed at the centre of the lower plenum.

During the coating process, various coating solutions were injected into the bed via a syringe pump at a rate of 100 µl min^{-1}. The coating solution was atomised by mixing it with a stream of air, flowing at 0.5 m^3 h^{-1}, in the nozzle. The system was operated under a pressure of 5 bars and a temperature of 50°C. During the process, a stream of compressed air was introduced into the system at a flow rate of 30 m^3 h^{-1}. The high compressed-air velocity was chosen to ensure sufficient dispersion of the coating liquid in the fluidised zone and to provide energy to break any binding between core particles in order to prevent agglomeration and promote the coating process. In addition, the coating solution was only introduced into the coating process when the temperature of the chamber was higher than 45°C.

A set of blank samples was created to eliminate the effect of attrition and fragmentation due to the coating process. The control samples were produced by placing the raw material (weight varied with the different core particles used) in the fluidised bed without coating solution for a period of 1 hour, and its size distribution before and after the fluidisation for a given period of time was measured using QICPIC.

3.11 Flowability Testing

The flowability of the bulk solid was described by ff_c and was experimentally determined using a ring shear tester RST-XS (Dietmar-Schulze, Germany). Firstly, each sample was placed carefully into the loading cell of the equipment, and the excess powder was scraped off

from the cell without exerting any compaction force to the bulk powder. The cell was then placed in the apparatus and the sample was subjected to the cycle of pre-conditioning (pre-shear) and shearing at different normal pressure until it reached the set pre-shear pressure (Schulze, 2006).

Initially, the effect of the pre-shear pressure on the flowability of the HiLAS 33 and HiLAS 70 powders was examined by varying the pre-shear pressure (HiLAS 33: 2-20 kPa; HiLAS 70: 2-22 kPA). For the entire test, the first point was repeated to ensure that the bulk powder did not lose its characteristics during the process.

For all of the HiLAS 33-coated particles, the flowability tests were conducted with a pre-shear pressure set at 20 kPa and normal stresses, σ_N, of 4–16 kPa until a constant shear stress, τ, was obtained. On the other hand, the HiLAS 70-coated particles were investigated using the standard test wherein the pre-shear pressure was set at 2 kPa and the samples were then sheared under normal stresses of 400–1800 Pa until a constant shear stress was obtained. A lower pre-shear pressure was used due to the HiLAS 70 caking under high pre-shear pressure of 20 kPa. On the other hand, when using a lower pre-shear pressure for HiLAS 33 and the HiLAS 33-coated particles, the flowability of the powder was high (ff_c > 20). At high flowability, the results were not reproducible, and therefore it was difficult to use by way of comparison. For the entire test, the shear stress of the initial normal stress was reproduced to ensure that the samples did not lose their characteristics during the process.

3.12 Storage Stability

The effect of particles' characteristics on their storage stability was determined using the unconfined yield stress to describe the storage stability of the powder. Firstly, the effect of the height of the consolidated powder bed was investigated. In order to accomplish this, different aspect ratios (0.8, 1.3, and 1.8) of the powder beds were prepared in a 13 mm diameter tableting mould and were subjected to a constant force of 100 N (0.75 MPa) in a dried condition in a desiccator. The impact of duration of the consolidation (7, 12, 24, 72 hours) on the unconfined yield stress was also examined.

The unconfined yield stress of the powder was then determined under cyclic environmental conditions. This condition was obtained by firstly loading the powder freely into the die with a diameter of 13 mm to a height of 17 mm to achieve a powder/bed aspect ratio of 1.3. The powder in the tableting mould was then placed in a humidified condition of 50% RH at 30˚C in an environmental chamber (HCP50, Memmert, Germany) with a 100 g weight placed on top of the tableting punch. The samples were then retrieved from the mould and were placed in the desiccator for 24 hrs for drying. The sample powder beds were obtained before and after drying to examine the unconfined yield stress of the powder beds. The unconfined yield stresses of the powder beds were obtained by compressing the consolidated bed with a flat probe of 100 mm diameter at a rate of 0.5 mm s^{-1} until the powder bed failed. The compressor, Instron Microtester

(Instron, UK) was attached with a force transducer that had a maximum load of 10 N and a sensitivity of 0.0001 N.

3.13 Statistical Analysis

For the roughness and flowability of the particles (dependent variables) of various samples (independent variables), they were analysed by the ANOVA post-hoc Tukey test, to evaluate whether the mean values were similar among each other (confidence level of 95%, p = 0.05). SPSS software (version 23.0, IMB Statistical Package for the Social Sciences) was used to carry out the statistical analysis.

The standard error of the experiment was calculated using

$$Standard\ error = \frac{s_x}{\sqrt{n-1}} \tag{3.3}$$

where s_x is the standard deviation and n is the number in the sample population. The margin of error, at 95%, will be twice the standard error. For this reason, the margin of error will be used in this thesis to represent the error in the experimental results.

Chapter 4. Characteristics of Uncoated Particles

Surfactant is a fundamental building block in the formulation of many cleaning products (Boerefijn, et al., 2007). In terms of reducing logistical costs, it is preferable to ship the highly concentrated surfactant as granulate to liquid formulation to reduce the weight of the shipment. It is also desirable to centralise the production of this surfactant powder, and hence, the surfactant powder will have to endure a long period in the container and under different environmental conditions. There is also a requirement for the powder to be easily mixed into the formulation, and so the flowability and storage stability of the powder will be critical in this supply chain. In order to seek ways of enhancing the storage stability and flowability of the surfactant powder, the properties of the raw materials obtained from P&G Newcastle (UK) were characterised. The research presented in this chapter aimed to characterise the physical properties of the received materials and to relate them to their powder flowability and storage stability.

4.1 Materials and Methods

4.1.1 Materials and Properties Measured

The materials used, HiLAS 33 and HiLAS 70, were surfactant powders supplied by P&G (Newcastle). See Section 3.2 for more details.

The particle size and shapes (Section 3.3), particle density (Section 3.4), surface topography (Section 3.6), and hygroscopicity (Section 3.5) were

tested in this chapter. In addition, the compression test was carried and the data was fitted into Adams, Kawakita, and Heckel models as mentioned in Section 3.9.1.

4.1.2 Flowability

The flow behaviour of the samples was quantified using the Schulze's ring shear tester and was represented by the flow index, ff_c, which was described in detail in Section 3.11. Different pre-shear pressures were used to investigate the effect of the pre-consolidation stress on the powder flowability.

4.1.3 Storage stability

The storage stability was characterised by the unconfined yield stress of the consolidated powder bed as outlined in Section 3.12. In addition, the effect of the height of the consolidated powder bed on the unconfined yield stress was investigated. In order to accomplish this, different aspect ratios (0.8, 1.3, and 1.8) of the powder beds were prepared in a 12 mm diameter tableting mould and were subjected to a constant force of 100 N in dried condition in a desiccator. The impact of duration of the consolidation (7, 12, 24, 72 hours) on the unconfined yield stress was also examined.

4.2 Results and Discussion

4.2.1 Physical characteristics of granules

Table 4.1. Particle characteristics of HiLAS 33 and HiLAS 70.

	HiLAS 33	HiLAS 70
d_{32} [µm]	452.7	251.2
Span [-]	0.57	0.80
Sphericity [-]	0.61	0.84
Particle density [kg m^{-3}]	1810 ± 60	1370 ± 10
S_a [µm]	18 ± 4	12 ± 6

The particle size and shape were measured using a QICPIC particle analyser, which is based on the imaging of a large number of single particles. The results are tabulated in Table 4.1. Each sample was ensured to be well dispensed to prevent any particles being overlapped when the images were taken. The size and shape of both HiLAS 33 and HiLAS 70 were obtained through analysing roughly 125,000 and 91,000 particles respectively. It was shown that the Sauter mean diameter, d_{32}, of HiLAS 33 was much larger than that of HiLAS 70, while HiLAS 70 had a wider range of sizes.

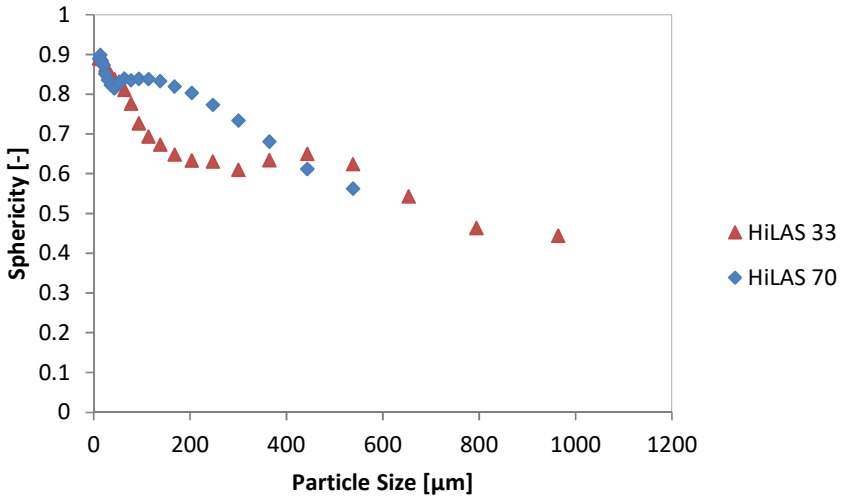

Figure 4.1 The sphericity of the surfactant powders. The particle size was presented by the equivalent diameter of the sphere, d_{32}.

In Table 1.1, the sphericity value of the particles from each sample presented corresponded to that of the 50 percentiles of the sample population. The results suggest that the particles in the sample with a higher surfactant concentration were more spherical. The shape of the particles was represented by their sphericity and was found to vary with particle size. It was demonstrated that as their size increases, the particles tend to become less spherical, as shown in Figure 4.1. It was also demonstrated that the HiLAS 33 particles were less spherical than those in HiLAS 70 when the particle size was less than 400 µm, and both samples had similar sphericity when the agglomerates were larger than 400 µm.

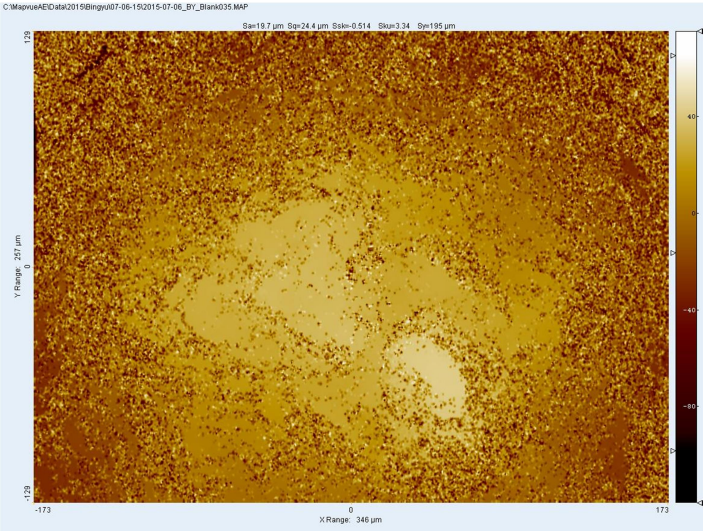

Figure 4.2 An example of the processed image obtained using the interferometer on the HiLAS 33 surfactant powder surface

The average surface roughness data of both HiLAS 33 and HiLAS 70 are also shown in Table 4.1. The surface roughness data obtained using the interferometer and the data were obtained from different parts of the surfaces of a particle. Twenty particles were used to characterise the surface roughness. An example of the image is shown in Figure 4.2. Table 4.1 shows that the less concentrated surfactant powder had a rougher surface.

a) b)

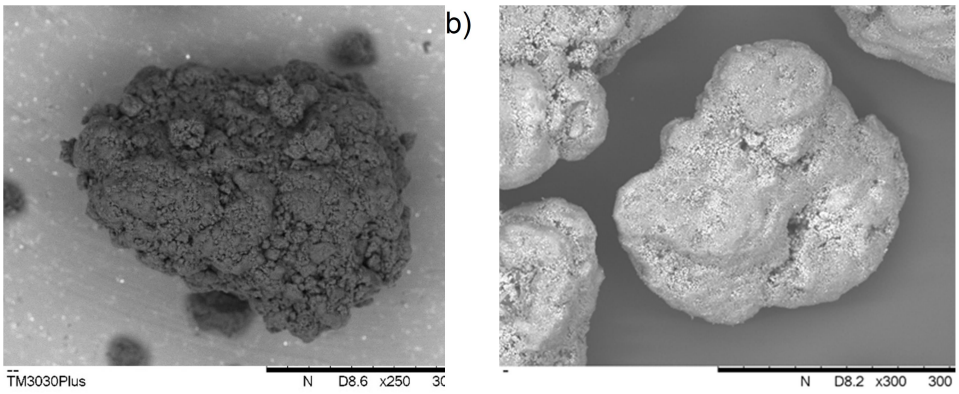

Figure 4.3 Image of a) HiLAS 33 and b) HiLAS 70 particle taken using SEM. The image was taken with backscattered electrons at 15 kV in a highly vacuumed environment.

Using the SEM, the images of surfactant particles were taken and are presented in Figure 4.3. The images show the irregularity in shape of the agglomerated particles, and cracks can be observed. These cracks were produced during the granulation of the surfactant powder. Furthermore, Figure 4.3 shows the rough surface on HiLAS 33 particles, which could be contributed by the crystalline structure of the salt content. The increase in concentration of the surfactant also reduced the composition of carbonic acid sodium salt in the formulation. This supports the roughness results obtained, as the higher salt content of the lower-concentration surfactant powder contributed to the high surface roughness. The images also show that the HiLAS 33 was less spherical than HiLAS 70. Furthermore, the images indicate that the HiLAS 70 was made up of smaller particles than HiLAS 33.

4.2.2 **Hygroscopicity**

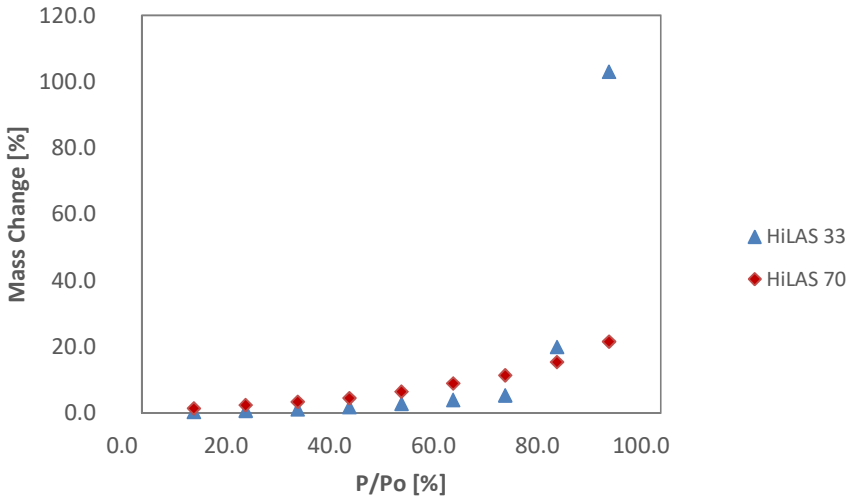

Figure 4.4 The adsorption curve of the surfactant powders, HiLAS 33 and HiLAS 70, under 25˚C

Figure 4.4 shows the adsorption curves of the HiLAS 33 and HiLAS 70 particles. By comparing the amount of moisture uptake by HiLAS 33 and HiLAS 70, the low-surfactant composition particles had a lower amount of vapour adsorbed at low humidity. However, under humidity of higher than 80% RH, the water uptake of HiLAS 33 increased dramatically. This suggests that increasing concentration of surfactant increased the hygroscopicity of the material as powder absorbed more water under humidity less than 80%. This finding concurred with Godridge (2009), who concluded that the increase in surfactant content resulted in more moisture uptake. Although a lower surfactant content resulted in less adsorption of moisture, the acetic acid salt, used as filler and structure support of the agglomerated particles, tended to deliquesce at high partial pressure of water (Calvert, et al., 2013). As a result, as the composition of the surfactant decreased, the amount of the acetic acid salt increased, which would deliquesce at lower humidity. The deliquescing humidity of HiLAS 33 was estimated to be approximately 70% RH, where the rapid increase in adsorption occurred (when P/P_o = 70%), while deliquescence was not observed with HiLAS 70.

4.2.3 **Hardness**

a)

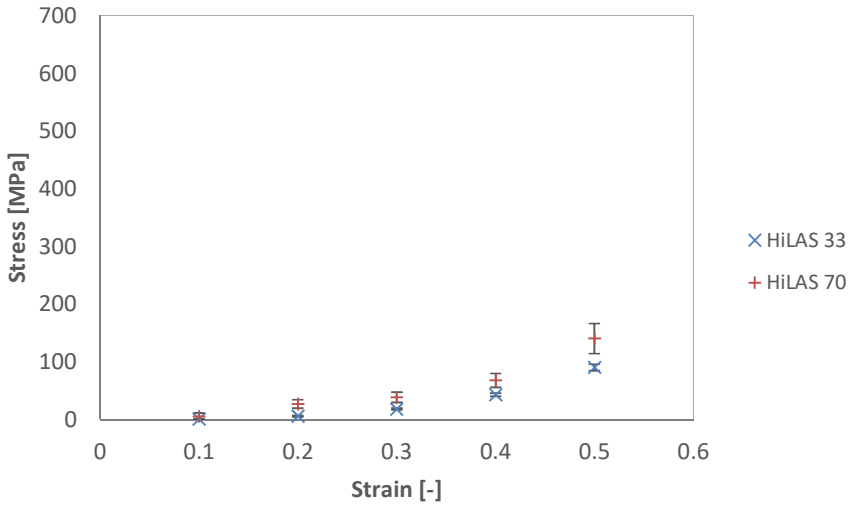

b)

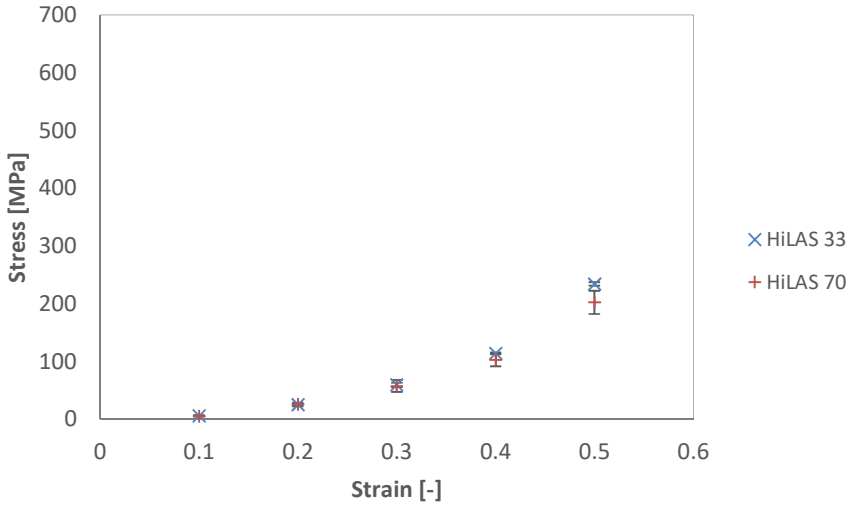

Figure 4.5 (Part 1) The stress and strain relationship of highly concentrated surfactant systems, HiLAS 33 and HiLAS 70s with different aspect ratios: a) 0.1 aspect ratio; b) 0.2 aspect ratio; c) 0.3 aspect ratio; and d) 0.4 aspect ratio. The error bars represent twice the standard error with five repetitions.

(Continued on next page)

c)

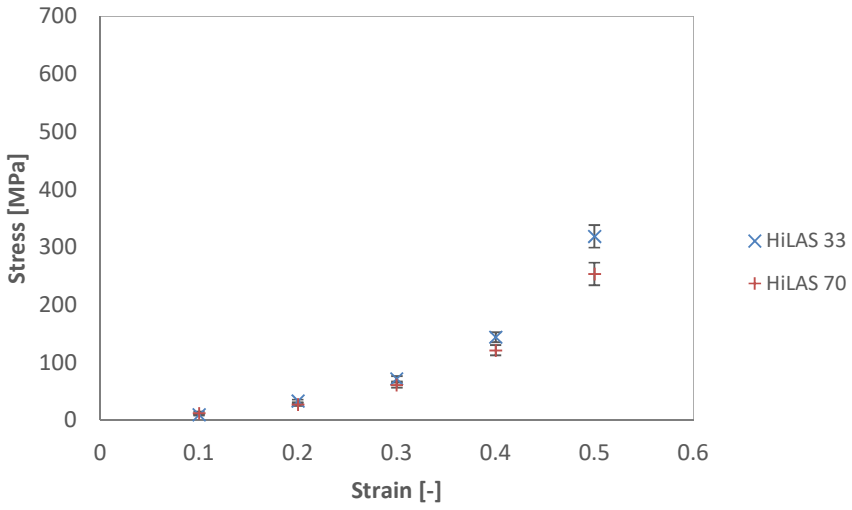

d)

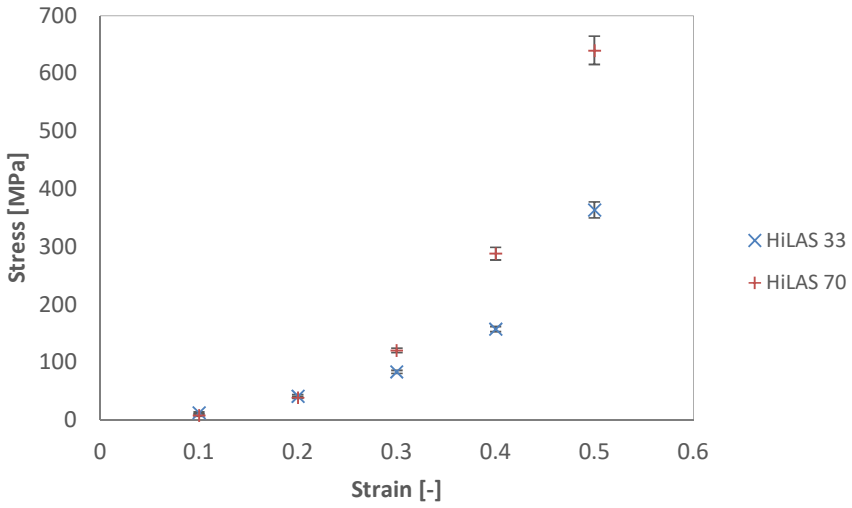

Figure 4.6 (Part 2) The stress and strain relationship of highly concentrated surfactant systems, HiLAS 33 and HiLAS 70s with different aspect ratios: c) 0.3 aspect ratio; and d) 0.4 aspect ratio. The error bars represent twice the standard error with five repetitions.

Figure 4.6 shows the compressibility of the surfactant powders of different concentrations through the stress vs strain obtained from the confined compression test using different aspect ratios in a compression mould. The force detected was normalised by using the average values of the force detected before the indenter made contact with the sample bed. It

was found that the aspect ratio of the compression mould affected the compression behaviour of both samples. As the aspect ratio increased, the stress required to compress the powder bed to a similar strain was greater. In addition, it was observed that the high-concentration surfactant powder, HiLAS 70, was clearly harder to compress for an aspect ratio of 0.4, as the compression stress required was higher. Furthermore, the stress required to compress HiLAS 70 particles to a given strain was similar in comparison with HiLAS 33 when the aspect ratio varied from 0.1 to 0.3, as the error bars overlap both curves. This was due to the friction force contributed when the particles were in contact with the wall. During the compression, the energy from the compression force was converted to particle deformation (both elastic and plastic), rearrangement of particles, and friction force (particle–particle and particle–wall) (Tomas, 2000). As the aspect ratio increased due to a larger number of particles being in contact with each other and with the wall, this resulted in higher required compression (Yap, et al., 2008). Furthermore, it was also discerned that the HiLAS 70 was affected by the aspect ratio more than HiLAS 33. This could be the result of the friction force being more dominant due to the HiLAS 70 having smaller particle sizes, as shown in Table 4.1. The smaller particle size would result in a higher surface area to volume ratio, which would increase the contact point among the particles, which in return increased the friction.

In addition to the above, it was observed that the compression stress required to achieve a strain of 0.5 for both HiLAS 33 and HiLAS 70

increased as the aspect ratio increased. It has been demonstrated that different compression stresses result in different mechanical behaviours (Sonnergaard, 1999), and in view of this, it would be desirable to quantify how the aspect ratio affects the values of the mechanical property parameters, which can be derived from the compression curves in order for them to be properly compared among different samples.

In this study, several mathematical models (Adams's, Kawakita's, and Heckel's models) were used to fit the experimental stress–strain data in order to determine the mechanical property parameters of different samples. The results also show how the aspect ratio could affect the values of these parameters.

4.2.3.1 Adams model

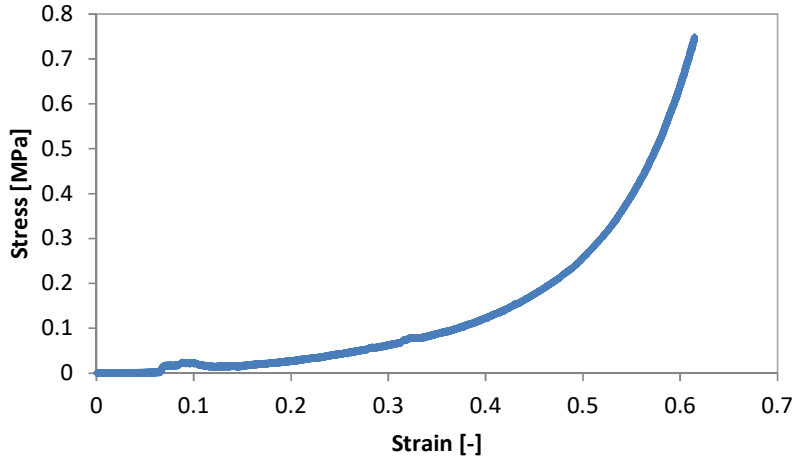

Figure 4.7 An example of the stress–strain curve obtained from compressing HiLAS 70 in a mould with an aspect ratio of 0.3

Figure 4.7 shows an example of the stress vs strain curve as a result of compressing surfactant powder, HiLAS 70, in a mould with 0.3 aspect ratio.

From the curve, it can be observed that the pressure did not increase in comparison to the later part, when the strain was less than 0.065.

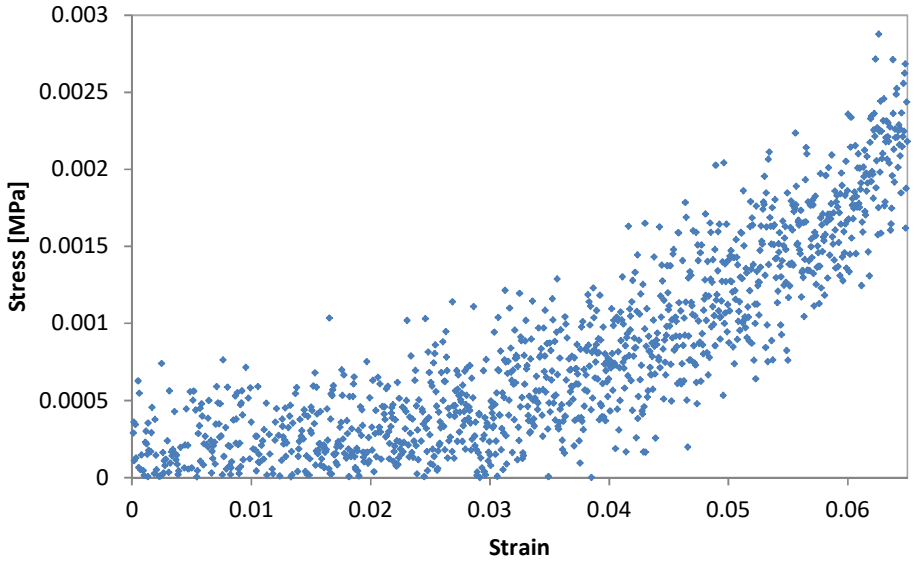

Figure 4.8 A close-up of the curve featured in Figure 4.7 when strain was less than 0.065

Close examination of the stress/strain curve in Figure 4.7, as shown in Figure 4.8, demonstrates that there was an increase in stress, even though it was at much smaller in magnitude in comparison to the later stage of the compression. At this earlier stage, the compressor probe was in contact with the surface of the powder bed, and the force caused the particles to rearrange in the initial stage, as previously mentioned in the literature review.

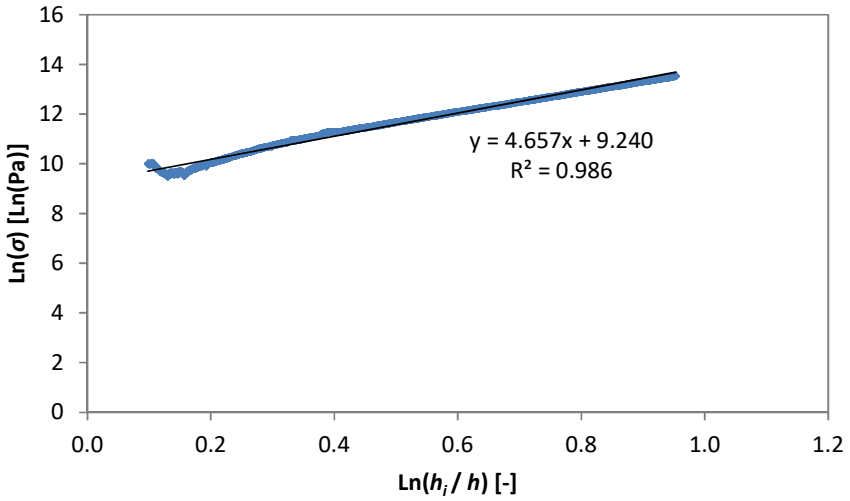

Figure 4.9 An example of the compression data of HiLAS 70 in a mould with an aspect ratio of 0.3 fitted by the Adams model, Equation (2.54), from the data displayed in Figure 4.7.

The stress/strain data obtained from the compression process was fitted to the Adams model described in Equation (2.54), and was displayed in Figure 4.9, which indicates a good agreement between them. The average coefficient of determination is 0.96 for all the results. It should be noted that the curve was trimmed to only show the section where compression stress greater than 1 MPa was measured. This was to ensure positive $ln\sigma$ values and eliminating the elastic region. It was thus assumed that the data were obtained from a high natural strain region, while the values of $ln(h_i/h)$ were greater than 0.2. The apparent coefficient of friction, α', and the apparent strength of the particles, τ_o', were then derived using the interception and the gradient of the line of best fit.

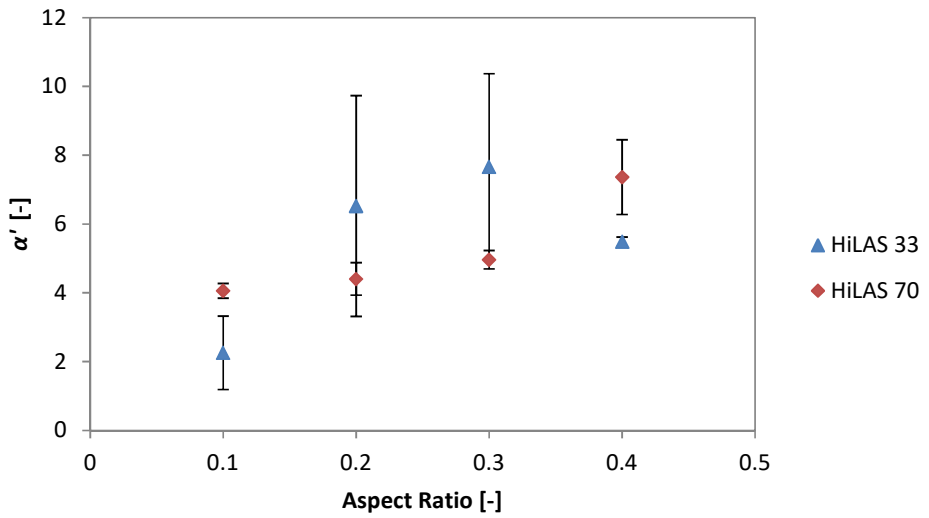

Figure 4.10 The derived friction factor against the aspect ratio in the compression mould. The error bars represent twice the standard error.

The interception of the straight line on the vertical axis, shown in Figure 4.9, was used to describe the friction the particles experienced during the experiment. The friction coefficients were then plotted against the aspect ratio, as shown in Figure 4.10. It can be observed that the data of HiLAS 33 had large errors for aspect ratios of 0.1, 0.2, and 0.3. These errors were caused by the large particle size, which resulted in difficulty in ensuring an evenly packed powder bed. Overall, both of the samples had similar friction coefficients due to the similar surface roughness demonstrated in Table 4.1.

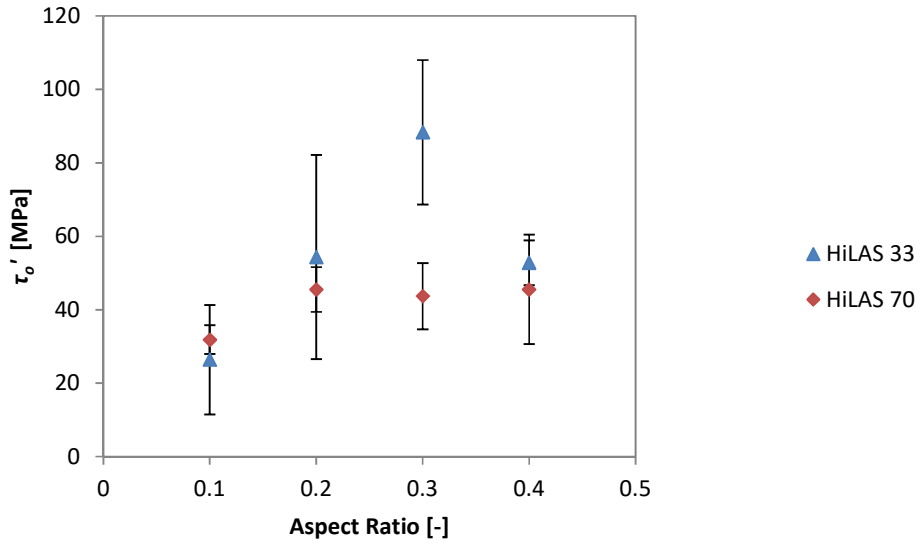

Figure 4.11 The particle apparent strength of the surfactant powder against the aspect ratio used in the compression. The error bars represent twice the standard error.

Subsequently, the gradient of the line of best fit as shown in Figure 4.9 was used to calculate the apparent strength of the particle. The derived values were plotted against the aspect ratio used in the compression, as shown in Figure 4.11. The results indicate that both samples had similar material strength, as the mean values with error bars overlap each other for a given aspect ratio, other than the result obtained with an aspect ratio of 0.3. For HiLAS 70 with different aspect ratios, the apparent strength appears to be the same, since the error bars on the means overlap each other.

Table 4.2 Standard error of the apparent strength and friction factor and the comparison of the errors. The gradient and y-axis standard errors from the best-fit curve were also tabulated in this table.

	Aspect ratio	Standard Error (%) Apparent Strength	Friction Factor	% Difference between Errors	Standard Error (%) Gradient	Y-axis Interception
HiLAS 33	0.1	56	47	19	47	10.5
	0.2	51	49	3.9	49	10.4
	0.3	22	35	-37	35	5.6
	0.4	12	2.6	351	2.6	1.3
HiLAS 70	0.1	12	5.3	129	5.3	1.4
	0.2	13	11	25	11	2.2
	0.3	21	5.4	285	5.4	2.5
	0.4	33	15	122	15	5.0

Comparing the error bars of the friction factors and apparent strengths in Figure 4.10 and Figure 4.11, it was observed that the errors of the apparent strengths were mostly larger than the friction factors. While the friction factors were derived from the gradient of the curve of best fit, the apparent strengths were calculated from the interception of the same curve and the friction factors. The errors could therefore have been carried forward from friction factors when obtaining the respective apparent strengths, resulting in the derived apparent strengths having higher errors.

However, there is no clear relation between the errors, as shown in Table 4.2. Moreover, there was also no clear correlation between the gradient and Y-axis interception errors. In the table, it shows that the standard errors of the Y-axis interception were much smaller than those of the gradients. It can be concluded that despite the complementary nature of the apparent strengths and friction factors, the unrelated errors between

the gradient and y-axis interception resulted in varying errors between the two derived parameters.

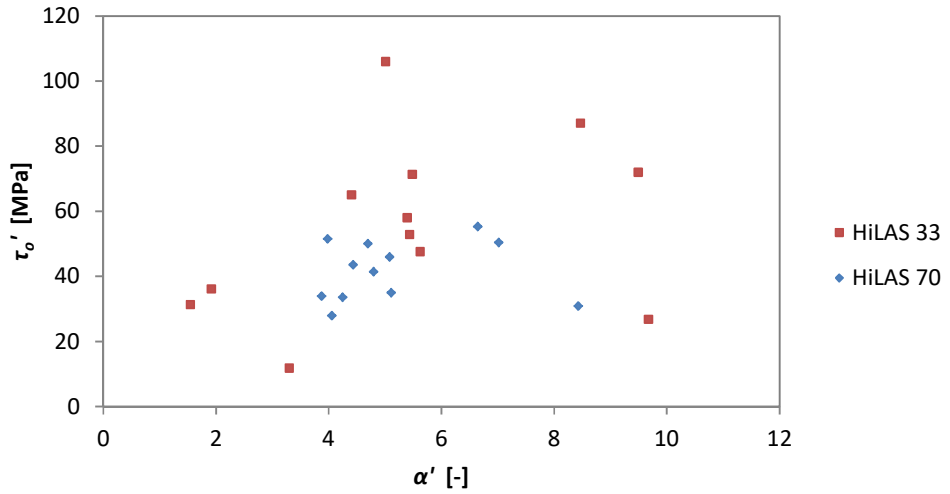

Figure 4.12 The relationship between the friction factors and the apparent strength

In Figure 4.12, it can be seen that the increase in the friction factors would generally increase the apparent strength of the particles. This was because energy applied to the powder bed was transformed into energy required to overcome the frictional force between the particles (Tomas & Kleinschmidt, 2009). The plot also shows that in general, the HiLAS 33 particles had higher apparent strength than those in HiLAS 70. The higher strength could be a result of the higher salt content, which provided structural support.

In conclusion, although the data can fit the model well and can provide crucial information on the particle physical properties, the results under given conditions showed large deviations. These deviations could be

caused by inconsistency in packing and the arrangement of the powder bed during compression, as described by Samimi et *al.*, 2005.

4.2.3.2 Kawakita model

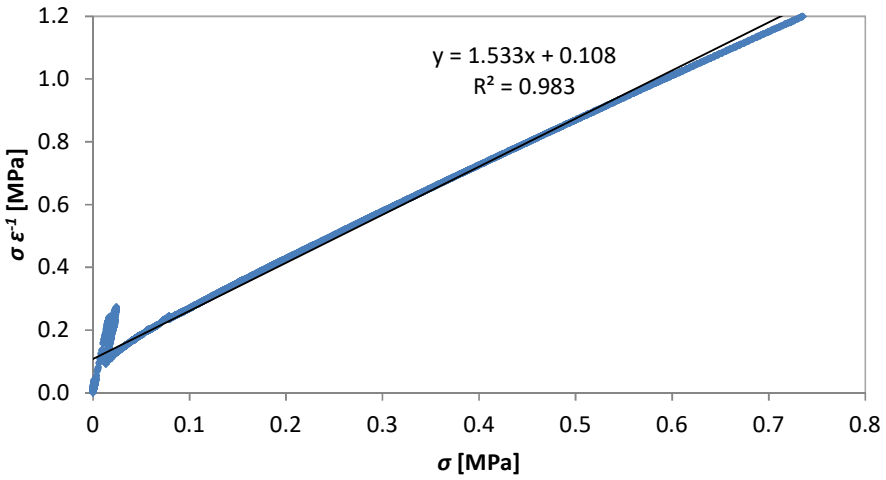

Figure 4.13 An example of the compression data fitted to the Kawakita model, Equation (2.50), for HiLAS 70 with an aspect ratio of 0.3. The curve was derived from the stress/strain curve in Figure 4.7.

The compression data was modelled using the Kawakita model exhibited in Equation (2.50), and a typical fit is illustrated in Figure 4.13. A linear relationship between the $\sigma\varepsilon^{-1}$ and σ for most of the data points can be seen, as predicted by the Kawakita model. However, there was an initial non-linear region with a rapid increase in stress. This could be due to the rearrangement of particles in the powder bed. The average coefficient of determination of the fitting using this model was found to be 0.96 ± 0.05.

The constants a and b^{-1} (also known as the Kawakita parameters) of the samples in the confined compression test were derived from the Kawakita model and are presented in Figure 4.14 and Figure 4.15 respectively.

While *a* describes the porosity of the powder bed, the Kawakita parameter *b* is related to the failure stress of the single particles in the powder bed.

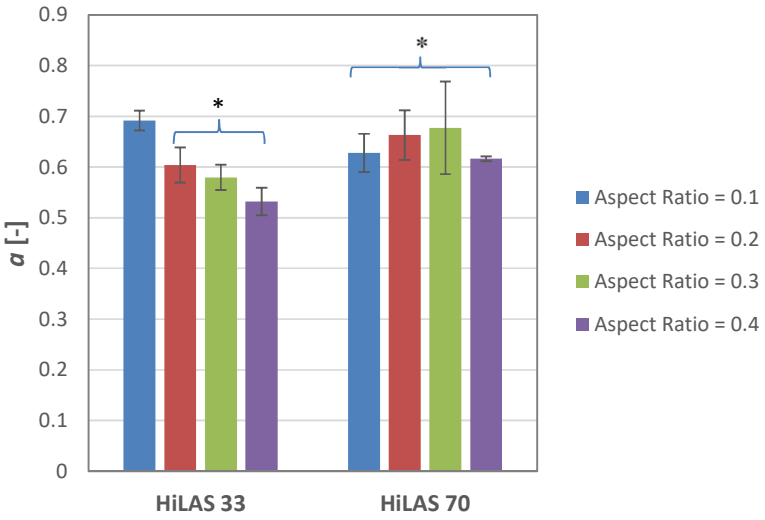

Figure 4.14 Derived *a* value of both samples. The error bars represent two standard errors of the mean from six repetitions. Data analysed with the ANOVA post-hoc Tukey test ($p < 0.05$, two-tailed) where * represents the similarity.

The result, in Figure 4.14, shows that for HiLAS 33 the mean value of *a* reduced as the aspect ratio increased from 0.1 to 0.2, and thereafter did not vary significantly; for HiLAS 70, the parameter *a* was constant for the aspect ratio investigated. The difference in the constant *a* value corresponding to the 0.1 aspect ratio could be as a result of the uneven filling of particles in the mould, due to the relatively large size of the particles and the small height of the bed.

Table 4.3 Initial bed porosity of the surfactant powder in the confined compression test, derived from the initial bed height, particle density, and weight of the powder bed. The errors presented represent twice the standard error in the calculated bed porosity.

	Bed Porosity, ε_b [-]	
Aspect Ratio [-]	HiLAS 33	HiLAS 70
0.1	0.68 ± 0.02	0.74 ± 0.02
0.2	0.64 ± 0.01	0.73 ± 0.01
0.3	0.67 ± 0.01	0.70 ± 0.01
0.4	0.63 ± 0.01	0.70 ± 0.01

Table 4.3 shows that the initial bed porosities of both the samples did not change significantly with the aspect ratio. The samples did not show much variation with the aspect ratio, as the samples were loaded into the compression mould freely and the excess powder was scraped off to ensure an evenly filled powder bed. In addition, it was found that the bulk density of HiLAS 33 was higher than that of HiLAS 70. This was due to the larger particle size of HiLAS 33 powder, although the surface roughness and shape were similar. As a result, the larger particles resulted in higher porosity among the particles.

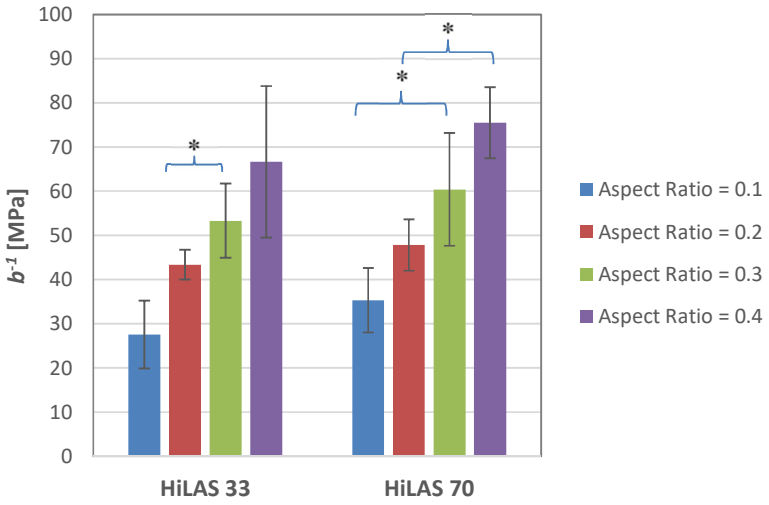

Figure 4.15 The derived *b* values of both the samples. The error bars represent twice the standard error of the mean from six repetitions. Data analysed with the ANOVA post-hoc Tukey test ($p < 0.05$, two-tailed) where * represents the similarity.

On the other hand, the b^{-1} mean values of the surfactant powder, displayed in Figure 4.15, increased as the aspect ratio of the compression mould increased for both samples. The wide error bars in the derived values were caused by the existence of imperfections in the agglomeration process, whereby cracks and cavities were produced as can be observed in Figure 4.3 (Yap, et al., 2008).

Despite the differences in mean values, statistically using a two-tail test with 95% confidence, there were some sets of data that had similarities, such as the b^{-1} values for HiLAS 33 with aspect ratios of 0.2 and 0.3. In addition, the set of b^{-1} values for HiLAS 70 were similar when comparing aspect ratios of 0.1 and 0.4. Overall, it was found that the results obtained using the 0.1 aspect ratio were different from the other data. The strength of the particles was thus not affected but the aspect ratio. In addition, there

was no clear relationship between the error in the packing and the deviation observed in the derived b^{-1} values.

4.2.3.3 Heckel model

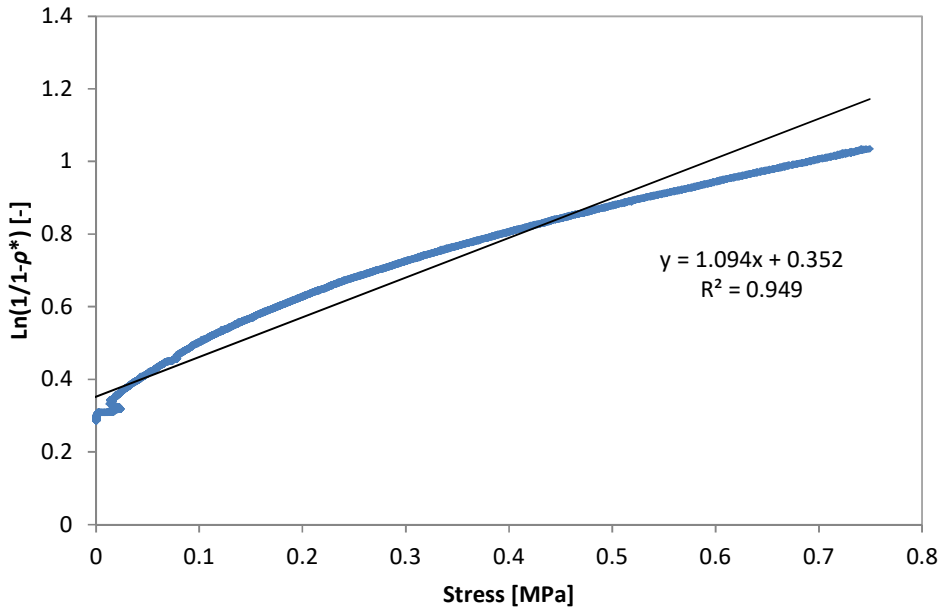

Figure 4.16 An example of compression data fitted to Heckel's model, Equation (2.49), (HiLAS 70, compressed in a confined 0.3 aspect ratio). The curve was derived from the stress/strain curve displayed in Figure 4.7.

The force/displacement data obtained from the compression processes were fitted to the Heckel model, as shown in Equation (2.49), with an example is presented in Figure 4.16. The derived compression parameters against stress follow a linear relationship until the material structure failed and a steep deviation was observed. The linear trend represents the elastic and plastic deformation during the compression, while the steep slope was contributed by the irreversible plastic deformation and particle fracturing. In the later stage, the porosity of the powder bed decreased

rapidly. The Heckel parameters were derived from the gradient of the linear section of the curve where both elastic and plastic deformation occurred. The average coefficient of determination for this model was 0.96 ± 0.02.

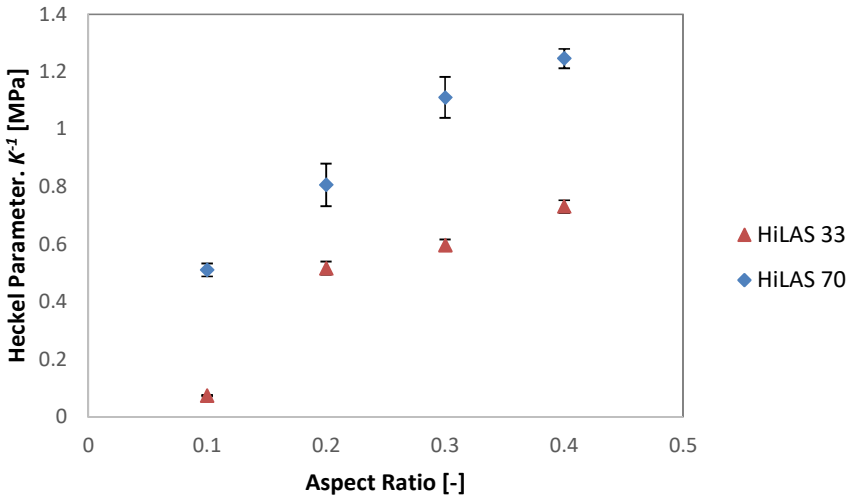

Figure 4.17 The derived Heckel parameter plotted against the aspect ratio of the powder bed used. The error bars represent twice the standard error of the experiment.

The acquired Heckel parameters of both samples were derived from the gradient of the linear part and were plotted against the aspect ratio used for the compression, as displayed in Figure 4.17. It is clear that the Heckel parameters were affected by the height of the powder bed, and as the aspect ratio increased, so the Heckel parameters increased. Likewise, in comparison to the other models, the number of particles increased when the aspect ratio increased. This resulted in more contact point between the particles where energy was lost in overcoming the frictional force among the particles and between the particles and the wall. Furthermore, the Heckel parameter value for HiLAS 70 is greater than for HiLAS 30 for a

given aspect ratio. Sonnergaard J.M (1999) stated that the Heckel parameter is sensitive to small deviations during the experiment and the porosity of the powder bed (Sonnergaard, 1999). With this in mind, the error bars of the derived Heckel parameter values can be related to the errors of the *a* values as shown in Figure 4.14. The relatively wide error bars of the Heckel parameter value for aspect ratios 0.2 and 0.3 of HiLAS 70 are consistent with the sizable error bars of the corresponding *a* values. Similarly, in comparison to the error bars of the *a* values and the error bars of the Heckel parameters, the smaller error bars of Heckel parameter values for HiLAS 33 and HiLAS 70 for an aspect ratio of 0.1 are correlated with the smaller errors in corresponding *a* values. The results thus concurred with observations in the literature.

The apparent densities of the particles were used to derive the Heckel parameters. These were used instead of envelope or tapped density, as the voidage within the particles will be more relevant during the compaction. As the structure of the particle collapsed during the compaction, the inner porous layer will play an important role affecting the structural strength of the particle.

4.2.3.4 Discussion on particle hardness

Table 4.4 The derived Adams (τ_o), Kawakita (b^{-1}), and Heckel parameters (K^{-1}).

	Adams Parameter, τ_o [MPa]	**Kawakita Parameter, b^{-1} [MPa]**	**Heckel Parameter, K^{-1} [MPa]**
HiLAS 33	67.5	19.6	292.8
Regression coefficient, R^2	0.311	0.997	0.979
HiLAS 70	44.8	19.8	395.9
Regression coefficient, R^2	0.924	0.953	0.97

In order to eliminate the effect of the wall during the compression, the parameters were derived from the intercept of the vertical axis of the linear line when the parameters were plotted against the aspect ratio (Yap, et al., 2008). The acquired values are exhibited in Table 4.4 together with the coefficient of determination of the linear line used to extrapolate. These values were used to represent the different material properties of single particles.

The results show that the coefficient of determination to extrapolate the Adams parameter to zero aspect ratio for HiLAS 33 is the smallest (0.311). In view of this, the Adams parameter obtained was discounted.

On the other hand, the Kawakita and Heckel parameters obtained show a reasonably good coefficient of determination of more than 0.95. It was found that the b^{-1} values of HiLAS 70 and HiLAS 33 are similar, which

suggests that the particles in both samples had similar fracture stress. While it was demonstrated in Equation (2.47) that Heckel parameter is directly proportional to the hardness of the material (Yap, et al., 2008). Hence, from the obtained Heckel parameter values, it was concluded that the higher surfactant composition resulted in greater hardness.

4.2.4 **Flowability**

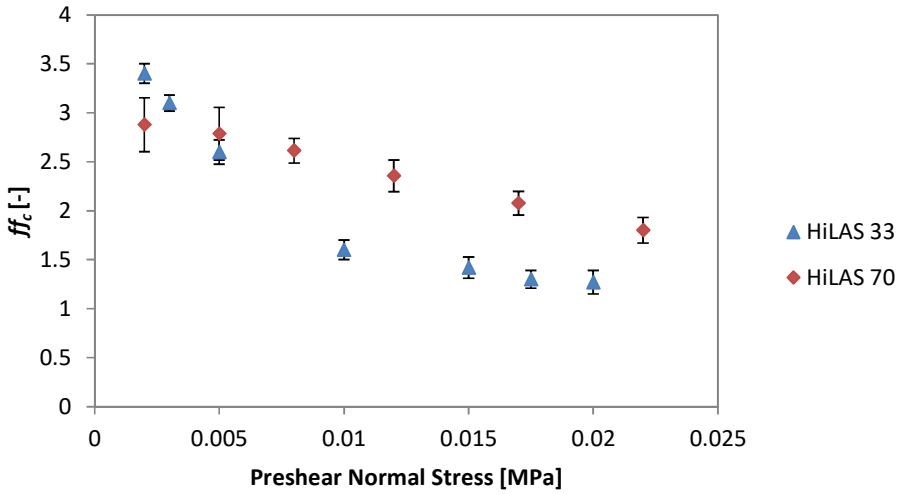

Figure 4.18 Flowability of HiLAS 33 and HiLAS 70 against the different pre-shear normal stress obtained using a Schulze's ring shear cell tester.

The effect of pre-consolidation normal force on the surfactant powders on their flowability was investigated. As shown in Figure 4.18, both samples exhibited reduced flowability as the pre-shear pressure increased. It was noticed that both the surfactant powders possessed cohesive flow behaviour under low pre-consolidation stress and tended towards the very cohesive flow region as the pre-shear pressure increased. This was expected, as the closely packed particles will consolidate and the

adhesion between the particles will increase, reducing the flowability of the powder (Tomas, 2000).

It was also observed that the flowability of HiLAS 70 deteriorated constantly as the pre-shear stress increased. The rate at which the flowability of HiLAS 70 reduced was gentler than the flowability of HiLAS 33 against the increasing pre-shear pressure.

This was because the HiLAS 70 powder was harder to compact, as suggested by the higher Heckel parameter presented in Table 4.4. When the powder was easier to compact, it resulted in a higher surface area per volume, which increased the adhesion force between the particles and the friction among the particles, which in turn, reduced the flowability.

On the other hand, there was a critical pre-shear stress for HiLAS 33 (10 kPa) where the flowability of the sample did not deteriorate much with increasing pre-shear stress. This suggested that at normal stress higher than 10 kPa, the powder bed did not change much in bulk density with the increasing normal stress.

The flowability of HiLAS 33 was initially higher than HiLAS 70 at low pre-shear pressure of 3000 kPa. However, as the pre-shear pressure increased, the HiLAS 70 exhibited better flowability than 3000 kPa. As previously mentioned, HiLAS 70 was more resistant to compaction and the reduced rate of flowability with increasing pre-shear was more gradual.

Overall, the pre-shear condition can affect the flowability of the powder. It is therefore important to determine the pre-shear condition of the test in order to carry out accurate comparisons between samples.

4.2.5 **Consolidation test**

In order to quantify the storage stability of the powder, a consolidation test, as described in Section 3.12, was carried out to determine the unconfined yield stress of the consolidated powder bed. The unconfined yield stress is related to the adhesion among the particles during the consolidation. Higher adhesion results in degraded storage stability, and it is thus desirable to achieve a product with low unconfined yield stress after the consolidation. In this experiment, 100 g of powder was measured and placed in the tableting mould to be consolidated. 100 g was calculated to be the force that the particles at the bottom of a 10 kg bag of raw material will experience. The amount of HiLAS 70 was then used to investigate the effects of the aspect ratio of the powder bed and the duration of consolidation on the unconfined yield stress. Subsequently, the consolidation stresses for both raw materials were examined.

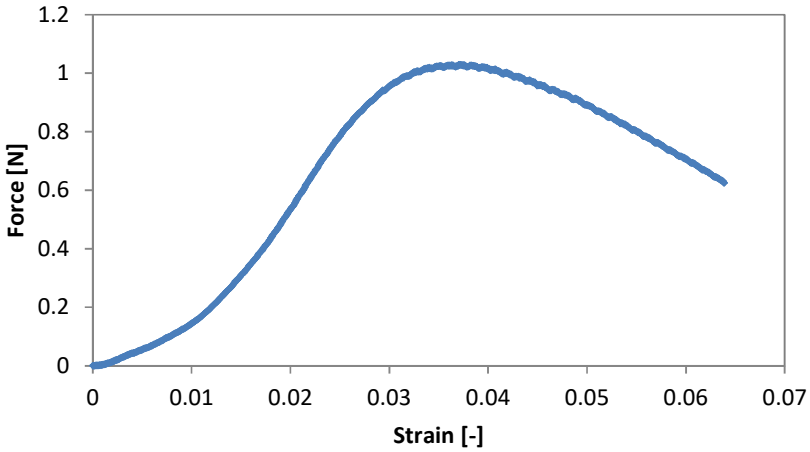

Figure 4.19 An example of the force vs strain curve obtained from compressing a consolidated HiLAS 33 powder bed

In Figure 4.16, a typical force vs strain curve, obtained from compressing a consolidation powder bed of HiLAS 33, is plotted. Firstly, the critical force was determined as the maximum force during the compression where the powder bed structure failed. Despite the structural failure, the powder bed did not collapse, and hence, there was an entailing trail of reducing force recorded subsequently. The unconfined yield stress was then calculated from the critical force per contacted area. It was assumed that the powder bed did not deform during the compression as the strain was small.

4.2.5.1 Unconfined yield stress vs aspect ratio

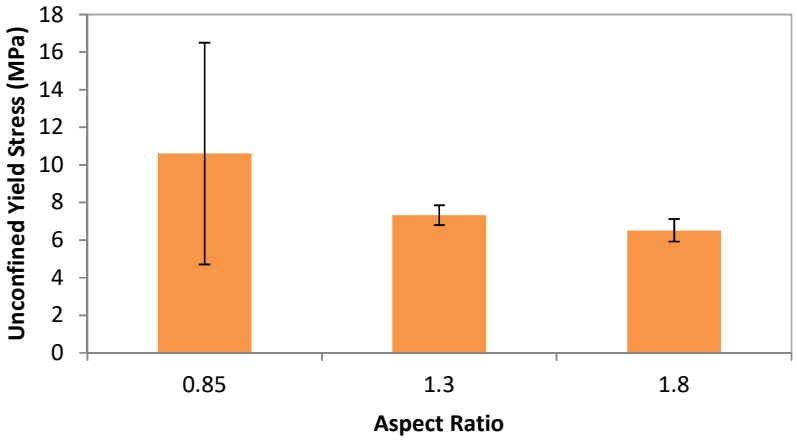

Figure 4.20 The stress of the powder bed, using HiLAS 70, when the consolidated bed failed under compression. The error bars represent double the standard error of the mean from 5 repetitions.

The obtained unconfined yield stress is plotted against the aspect ratio in Figure 4.20. It shows that as the aspect ratio increased, the unconfined yield stress reduced. The results concurred with those reported by Calvert *et al* (2013). Furthermore, it is notable that the unconfined yield stress of the powder bed with an aspect ratio of 0.85 had a large error. This was because the force where the powder bed failed under compression could not be easily determined, as shown in Figure 4.21. It was found that during the compression of the consolidated bed, the powder bed underwent plastic deformation (cracking) rather than collapse as previously reported.

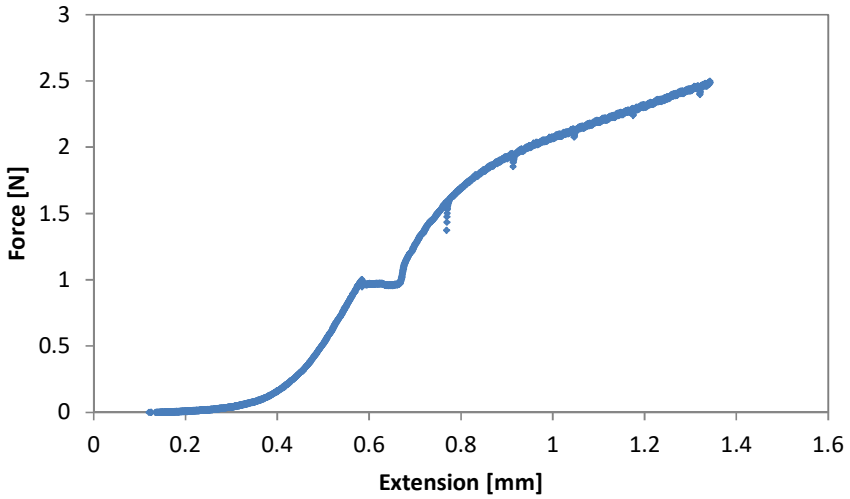

Figure 4.21 An example of the force vs displacement curve for compressing a powder bed with an aspect ratio of 0.8. HiLAS 70 was used in this experiment.

4.2.5.2 Unconfined yield stress vs time

It can be seen in Figure 4.22 that the unconfined yield stress increased by more than 50% between 7 and 24 hours. However, the rate reduced between 24 and 72 hours as the force required for the failure of the powder bed increased by roughly 25%. Despite using a different time scale, the unconfined yield stress obtained by Calvert *et al.* (Calvert, et al., 2013) showed that the powder caking strength increased with the duration and a reduction in the increment was observed between 72 and 96 hours.

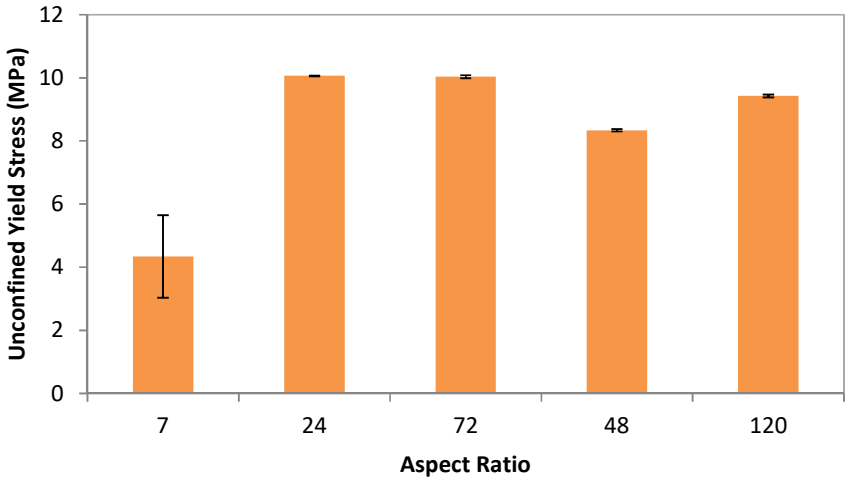

Figure 4.22 The relationship of the unconfined yield stress of the powder bed versus time. The error bars represent twice the standard errors derived from the experiments from three repetitions. HiLAS 70 was used in this experiment.

4.2.5.3 Unconfined yield stress of different samples

After examining the effect of aspect ratio and consolidation duration on the unconfined yield stress of the HiLAS 70, the powder bed with an aspect ratio of 1.3 was consolidated for 24 hours. This was to ensure reproducible data with the least sample and time required. In this case, the storage stability of both samples was investigated under 50% RH, as it was reported to be the highest humidity the samples would experience in the packaging (Godridge, 2009). The samples were also dried in a desiccator. A control test with just consolidation of the powder for duration of 24 hours was also conducted.

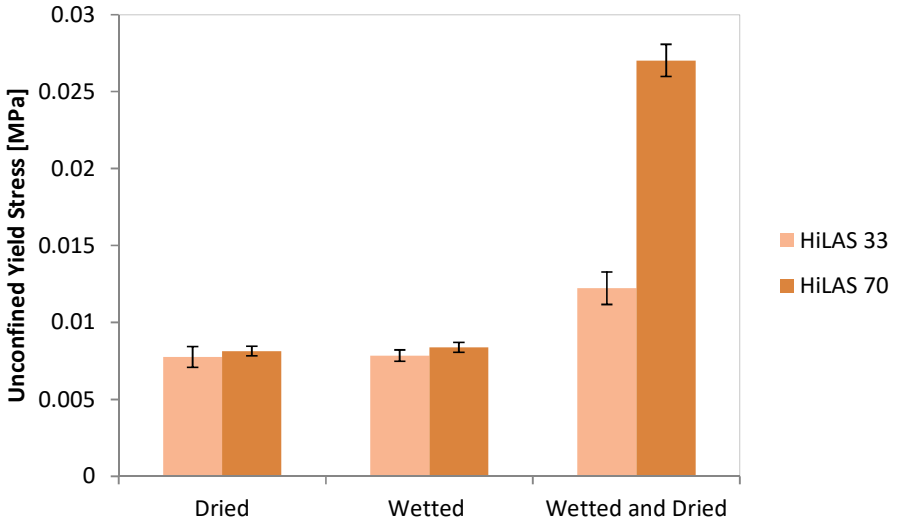

Figure 4.23 The unconfined yield stress of the different samples under various environmental conditions (dried and wetted).

Figure 4.23 presents the results of the consolidation test as mentioned above. It was found that the unconfined yield stresses of both samples were similar under dried and wetted conditions. However, the consolidation strength increased significantly for both samples when they were wetted and dried. This suggests that the wetted samples did not increase the inter-particle force. Instead, when the moisture adsorbed during the wetting process was removed, a solid bridge made of water-soluble materials (such as surfactant) on the surface of the particle contributed to the higher adhesion among the particles (Aguilera, et al., 1995).

In addition, in Figure 4.23, it shows that the powder with higher surfactant composition had much higher consolidation strength after drying. This was related to the higher amount of moisture uptake of HiLAS 70 particles, which was previously shown in Figure 4.4. The higher amount of moisture

would result in more soluble material dissolving to construct the solid bridge, which increased the unconfined yield stress. It was thus important for the surface of the particles to be less hygroscopic, especially under 50% RH, in order to promote prolonged storage stability.

4.3 Conclusions

In this chapter, the surfactant powders supplied by P&G were characterised by their size, shape, density, hygroscopicity, and several mechanical properties. It was found that the received HiLAS 33, which had lower surfactant content, had larger particle size, more irregular shape, rougher surface, wider particle size range, and higher density than HiLAS 70. Furthermore, it was also shown that HiLAS 70 particles were more hygroscopic, despite HiLAS 33 tending to deliquesce under high humidity.

Confined compression tests were carried out on both samples to quantify the mechanical properties of each sample. The compression data were fitted to three different models (Adams, Kawakita, and Heckel), in order to obtain the parameters that describe different physical characteristics of the powder. It was found that HiLAS 33 had higher apparent strength, while HiLAS 70 was more elastic and could withstand higher fracture stress. In addition, it was found that the increasing aspect ratio resulted in higher maximum compression stress to achieve the same strain. To address this, the obtained parameters were corrected by extrapolating the respective parameters to those when the aspect ratio of the compression was zero.

The flowability and storage stability of both samples were also studied using the Schulze's ring shear tester. It was found that the HiLAS 33 powder had higher flowability at low pre-shear pressure, whereas HiLAS 70 exhibited better flow behaviour at high pre-shear pressure. Both powders were initially in the cohesive flow region, which deteriorated into the very cohesive flow region under higher pre-shear pressure. The storage stability had also been characterised using a consolidation test. It was established that the storage stability of both samples was similar under dry conditions. The result obtained from the consolidation test agreed with the data obtained from the ring shear tester, whereby the unconfined yield stress values for both samples were similar. On the other hand, under humidity of 50% RH, the HiLAS 70 displayed significant deterioration in its storage stability. This was due to the natural hygroscopicity of HiLAS 70, which picked up more moisture than HiLAS 33.

Overall, this chapter demonstrates the effect of the particles' characteristics on the flowability and storage stability of the powders. These results will be carried forward to the next chapter to further investigate the effects of the particle size and Heckel parameter on flowability.

Chapter 5. Understanding Flowability of Adhesive Soft Powders

Chapter 4 shows the different particle characteristics (mechanical properties and hygroscopicity) and how they impacted on the flowability and storage stability. However, as there are several parameters that can impact on the flow behaviour, the product's flow characteristics cannot easily be determined by a single correlation (Ganesan, et al., 2008; Schulze, 2011; Stoklosa, et al., 2012). Since there is no theoretical model to quantify the effect of the material properties on the flowability, the aim of the research presented in this chapter was also to establish a new model to describe the relationship between the flowability and the mechanical properties of the powder system to further understand the flow behaviour of the particles.

5.1 Material and Methods

5.1.1 Materials and Properties Measured

HiLAS 70, supplied by P&G (Newcastle, UK), was used for the experiment. More information on the material can be found in Section 3.1. The raw powder was sieved into four different size ranges: 100–212 μm, 212–355 μm, 355–500 μm, and > 500 μm.

In this chapter, the images of particles were taken using method found in Section 3.7. Furthermore, the particle size, shape, size span (Section 3.3), and bulk mechanical properties (Section 3.9.1) were investigated.

5.1.2 Mechanical properties of single particles

The mechanical properties, Young's modulus, and hardness were also examined using a micromanipulation technique. See Section 3.9.2 for more detail on the technique.

In addition, the particle initial height, x_{height}, and width, x_{width}, were measured. The surface area of the particles was then estimated by assuming that the particles had the shape of an oblate spheroid with a surface area, S_{oblate}, by

$$S_{oblate} = \pi x_{width} x_{height} + \frac{\pi x_{height}^2}{4e} \ln\left(\frac{1+e}{1-e}\right) \quad (5.1)$$

where e is the ellipticity of an oblate spheroid and is defined by

$$e = 1 - \frac{x_{height}^2}{x_{width}^2} \quad (5.2)$$

The compression data were then fitted to the Hertz model. The width of the particles was also used as the Feret diameter (longest side) (Weisstein, n.d.).

5.2 Results and Discussion

5.2.1 Size, shape, and density of particles

In order to build a new model of the flowability of a highly concentrated surfactant powder system, the physical properties of the particles were characterised, including size, shape, particle density, bulk porosity, the moisture content of the powder as received, and different particle size ranges obtained by sieving the received sample. The results are

presented in Table 5.1 (referred to as “Experimental Results”). The values for the bulk samples’ span and porosity were then calculated using Equations (3.1) and (3.2) respectively. These are also shown in Table 5.1 (referred to as “Derived Results”).

Table 5.1 The particle properties (size, shape, density, moisture content, sphericity, span, and voidage) of the surfactant powder, HiLAS 70, of various size ranges and “as received”

	Experimental Results				**Derived Results**			
Sieve Size Range [μm]	d_{32} **[μm]**	r_{mean} **[μm]**	$d_{v,10}$ **[μm]**	ϕ **[-]**	ρ_p **[kg m^{-3}]**	ρ_b **[kg m^{-3}]**	ε **[-]**	**Span [-]**
As Received	207.1	154.7	92.6	0.60	1350 ± 2	442 ± 7	0.67 ± 0.01	3.03
100–212	130.3	76.4	76.3	0.60	1400 ± 1	380 ± 17	0.73 ± 0.03	1.31
212–355	251.2	142.1	174.6	0.55	1370 ± 1	391 ± 6	0.71 ± 0.01	0.80
355–500	473.0	259.3	379.3	0.70	1320 ± 1	367 ± 27	0.72 ± 0.05	0.75
> 500	742.3	448.9	556.7	0.60	1270 ± 2	382 ± 11	0.70 ± 0.02	0.96

In Table 1, as the particle sizes, d_{32}, r_{mean}, and $d_{v,10}$, were determined using a wide range of different particle sizes, the span value rather than the standard deviation was used instead to describe the distribution of the particle size. It was found that the span value of the particles in a size range of 100–212 μm was wider than that of the other sieved samples. Furthermore, the sphericity (Φ) was estimated from the plot of particle size versus shape, where the sphericity of a particle with the size of d_{32} was recorded with ± 0.005 accuracy.

In addition, it was observed that the particle density decreased with increasing particle size. The reduction in density with increasing size of the particle seemed likely to be due to the porous structures created during the agglomeration process used to manufacture these granulates (El Hagrasy, et al., 2013; Faure, et al., 2001). Theoretically, the bulk porosity for neatly arranged spherical particles of the same size in a cube is 47.6% (Haughey & Beveridge, 1966); however, the porosity of the samples was found to be more than 67%. This is because the particle density used for the calculation of the bulk porosity based on Equation (3.1) was the absolute density, which accounts for all the porosity within the samples.

5.2.2 **Surface roughness of particles**

As shown in Equation (2.3), surface asperity can also contribute to the adhesive force among the particles. In view of this, in addition to the parameters mentioned above, the surface topographies of the particles were also investigated. The experimental results of different samples, S_a, were used to describe the surface asperity, as presented in Figure 5.1.

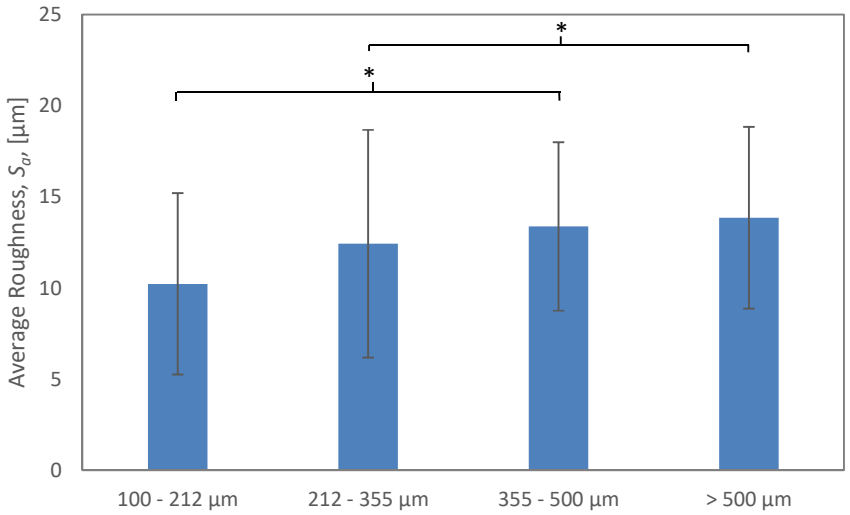

Figure 5.1 Average surface roughness of the different HiLAS 70 samples. The error bar represents twice the standard error with a population size of 30. Data analysed with the ANOVA post-hoc Tukey test ($p < 0.05$, two-tailed) where * represents similarity.

Due to the non-uniform surface of the particles, the standard deviations of the data were relatively large (about 35–50% of the arithmetic mean). By applying the statistical analysis with a confidence level of 95%, it was found that only particles of 100–212 µm and > 500 µm had different average surface roughness, based on a population of 30 particles in each size range. Furthermore, particles of 100–212 µm, similarly to those of > 500 µm, had similar roughness to those of 212–355 µm and 355–500 µm.

5.2.3 Mechanical properties of particles estimated using bulk powder compression

It has been reported that the elastic modulus of various materials (such as ibuprofen, mannitol, paracetamol DC, β-lactose, etc.) increased with its yield pressure. The yield pressure was later demonstrated to be proportional to the hardness (Sonnergaard, 1999; Yap, et al., 2008). The hardness of the particle can thus be related to the elasticity of the material,

whereby the hardness increases when the material is more elastic. Between the two material property parameters, it was relatively easier to determine the hardness of particles. The hardness can be represented by the Heckel parameter, which can be calculated from the stress-against-displacement data generated from compaction of a powder bed (Yap, et al., 2008). Accordingly, in order to quantify the material property of the particles, a confined compression test was carried out with different aspect ratios in a compression die. The stress and displacement data obtained from different samples were then fitted to Equation (2.49) to calculate the Heckel Parameter, K^{-1}. Subsequently, the Heckel parameters of particles in different size ranges and “as received” are plotted against the aspect ratio, as displayed in Figure 5.2.

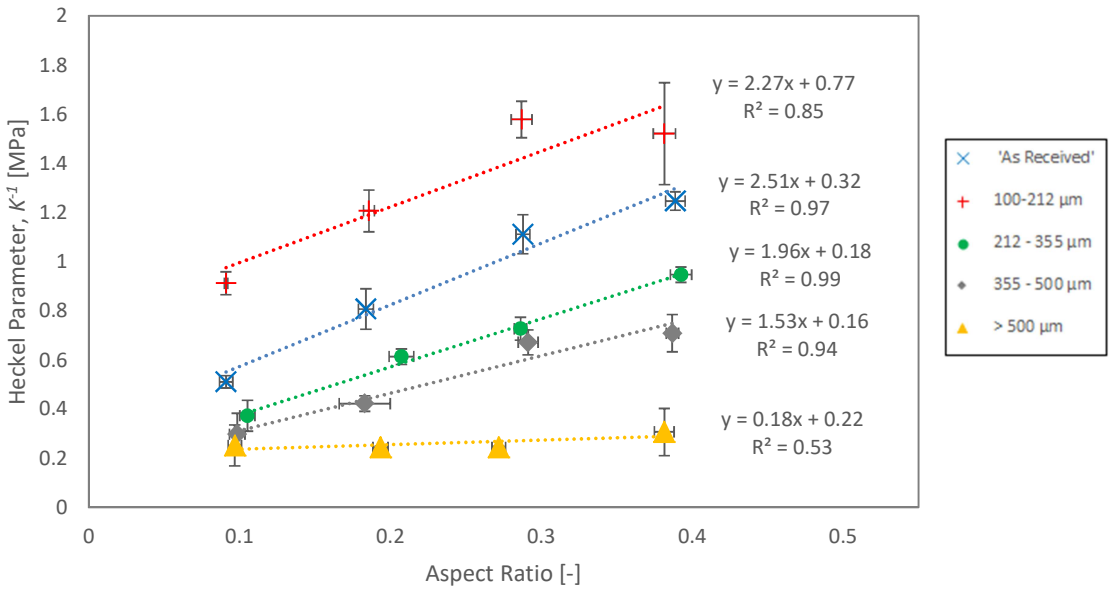

Figure 5.2 The hardness of HiLAS 70 particles in different size ranges and “as received”, obtained by using a confined compression test. The error bars represent twice the standard error of the mean from five repetitions.

As expected, the K^{-1} values increased with aspect ratio linearly, but the slope seems to decrease with the increase in the mean particle size. The smaller particles would have more contact points with the wall as their surface area per volume is larger, and hence would be more significantly affected by wall friction than the larger particles. Nevertheless, the K^{-1} values at the vertical axis (Y) interception can be used to describe the hardness in order to eliminate the effect of the friction force between the particles and the surface wall (Yap, et al., 2008).

Table 5.2 The Heckel parameters derived from the equation of the best fitted line, which described the relationship between the Heckel parameters and the aspect ratio of the HiLAS 70 powder bed

Samples	**Heckel Parameter [MPa]**	
	Y-Intercept	Corrected with Particle Size (d_{32})
As received	0.32	0.34
100–212 µm	0.77	0.78
212–355 µm	0.18	0.21
355–500 µm	0.16	0.20
> 500 µm	0.22	0.13

However, it was observed in this work that using the intercept of the linear fitting was not the best way to determine the Heckel parameter of the material. In Figure 5.2, the particles in the 212–355 and 355–500 µm size ranges showed greater resistance to compression, leading to a higher Heckel parameter in comparison to values of the particles larger than 500 µm for all different aspect ratios. However, the intercept of K^{-1} value for > 500 µm was larger than the other two size ranges, as shown in Table 5.2. It should be noted that the corresponding value for the coefficient of

determination is not great (R^2=0.53). In view of this, the Heckel parameters were derived from the equation of the linear line of best fit for each sample, and the Heckel parameters were calculated by the aspect ratio of the particle size (using d_{32}) to the diameter of the compression die (12 mm) used. The d_{32} of the samples were inputted into the equation as "*x*" value from the linear line of best fit equation to calculate the "*y*" value from the linear line of best fit equation, which represents the corresponding Heckel parameter. This approach has a more significant impact on samples with bigger particles than smaller ones. The obtained respective Heckel parameters for each particle size are presented in Table 5.2.

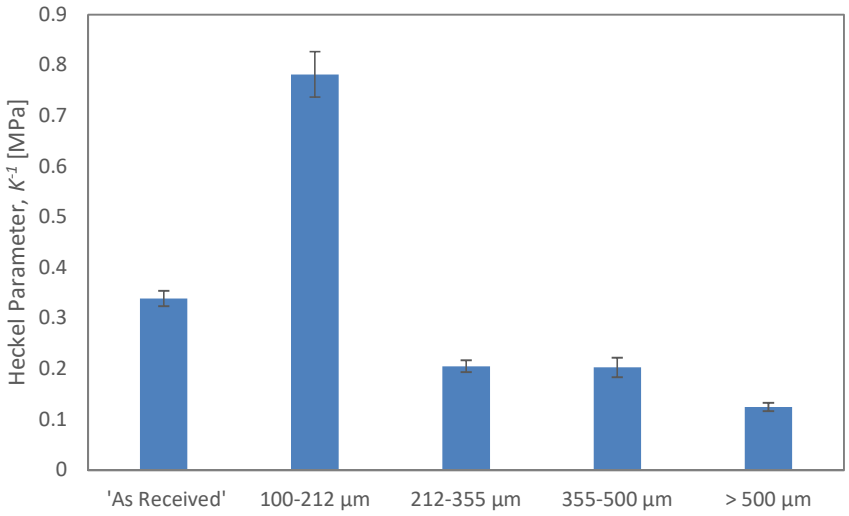

Figure 5.3 The derived Heckel parameter of particles of different size ranges and "as received". HiLAS 70 particles were used.

The Heckel parameters derived from the particle size are presented in Figure 5.3. With this method, it was found that the derived Heckel parameter values represent the mechanical properties of the powder

system better where the > 500 μm particles were the softest, while the particles in 212–355 and 355–500 μm size ranges were of similar hardness. In addition, the particles in the smallest size range (100–212 μm) showed considerably greater hardness than the other samples.

The higher Heckel parameter of the smaller particles was due to the higher particle density, as shown in Table 5.1. It is also shown in the same table that the particle density reduced as particle size increased. It has been shown that as the growth rate of the particle increases, the porosity of the shell will reduce (Rieck, et al., 2015), and therefore, as the surfactant particle size increases, the particle density reduces, as reflected in the experimental results in Table 5.1.

5.2.4 Mechanical properties of particles using single-particle compression

The mechanical properties of the single surfactant particles were also examined using the micromanipulation technique, which allows evaluation of the deformation behaviour and the mechanical strength of the individual particles (Yap, et al., 2008).

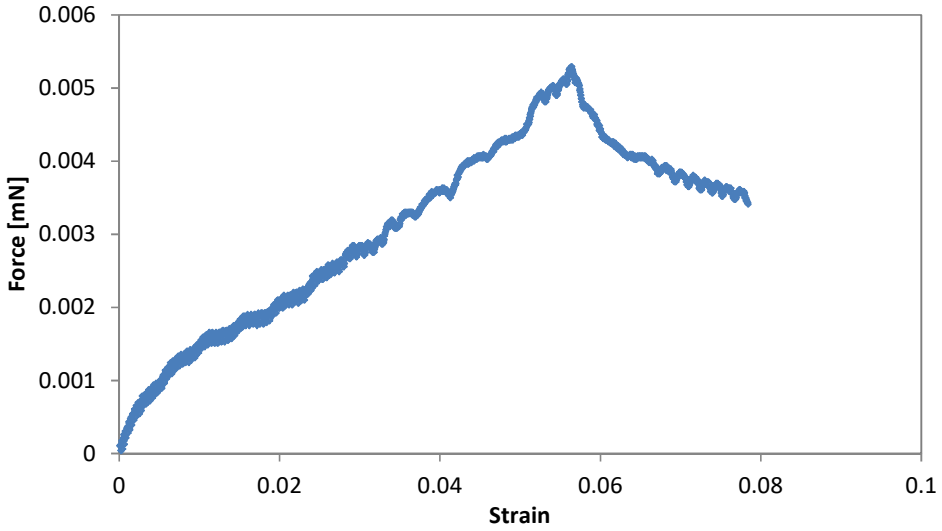

Figure 5.4 An example of the force and displacement curve obtained from compressing a single highly concentrated surfactant particle, HiLAS 70, with a Feret diameter of 525 μm

The acquired example of the force and strain relationship of the HiLAS 70 particle is presented in Figure 5.4. Firstly, it was observed that the data obtained were noisy. The noise might be caused by the rough surface of the particle. It could also be caused by the rearrangement of the particle on the stage when it was being compressed. The rearrangement of the particle might result from the non-spherical shape of the particle, as was shown in Chapter 4.

In addition to the above, two different behaviours in the compression were noted. Initially, the force increased sharply at low displacement. As the displacement reached about 1 μm, the gradient decreased. The compression force in the initial stage (strain < 0.01) was probably generated from elastic deformation. Subsequently, plastic deformation occurred in the later stage of the compression when the strain was higher than 0.01, until the particle structure failed when the strain reached around

0.06 (Tomas, 2000). The compression data of the single particle was subsequently fitted to the Hertz model to estimate the elastic modulus of the particle.

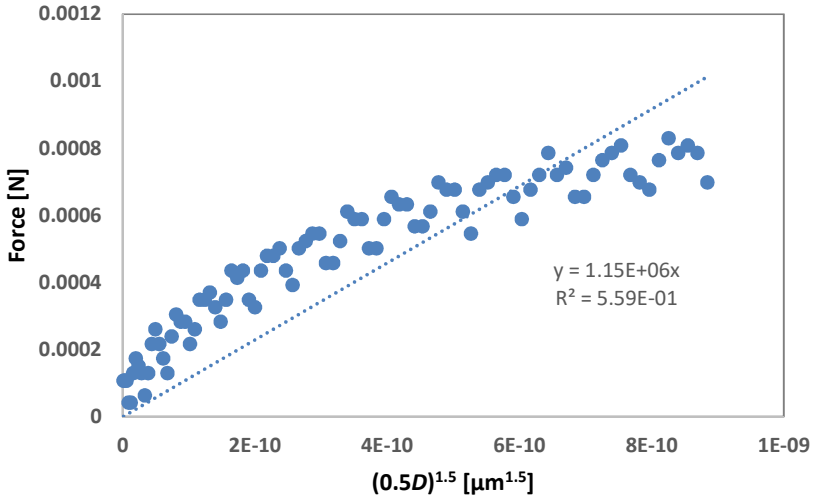

Figure 5.5 The fitting of the Hertz model to the compression data of a single surfactant powder, HiLAS 70, with a Feret diameter of 525 µm. The plot shows the curve up to 0.003 of the strain and the equation of the linear line of best fit.

An example of the fitting of the Hertz model to the compression data is displayed in Figure 5.5 in the initial elastic deformation region, when the strain was less than 0.2 (Yap, et al., 2008). The line of best fit that passes through the origin is also included in the figure. The width and height of the particle were measured. The particle was assumed to be an oblate spheroid, and by using the sphericity (ϕ_x) of the particle of the measured Feret diameter, the area equivalent diameter, x_A, was calculated from

$$\phi_x = \frac{\pi^{\frac{1}{3}}(6V_p)^{\frac{2}{3}}}{S_a} \tag{5.3}$$

where V_p is the equivalent volume of a sphere and S_a is the surface roughness of the particle. Subsequently,

$$x_A = 2 \times \left(\frac{\phi_x S_a}{4\pi}\right)^{\frac{2}{3}} \tag{5.4}$$

The Feret diameter of the particle was used to determine the sphericity of the particle, as that was what could be measured with the optical microscope during the compression. The sphericity of the particles was plotted against their Feret diameter, as shown in Figure 5.6.

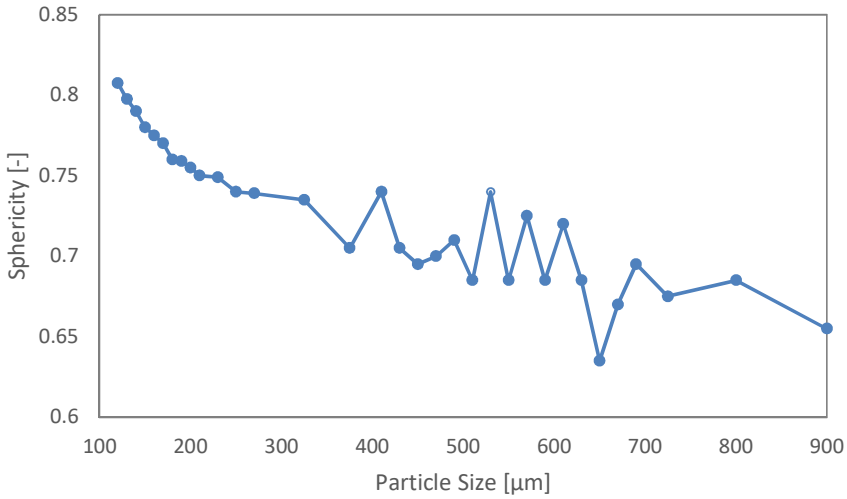

Figure 5.6 The sphericity chart of HiLAS 70 powder obtained from QICPIC particle size analyser. The particle size was represented by the Feret diameter.

It was observed that the line of best fit did not have a high coefficient of determination, which suggests that the model did not fit the compression data very well in this instance. This might be due to the irregular shape of the particle, as can be observed in Figure 4.3, where the contact of the probe with the particle was not how the model assumes. This resulted in high uncertainty in the prediction of the surface area of the probe in

contact with the particle. On the other hand, there were also instances where the fitted line extended through the origin had a coefficient of determination values as high as 0.9. The average coefficient of determination was 0.62, with twice the standard error of 0.08 after 50 particles were measured.

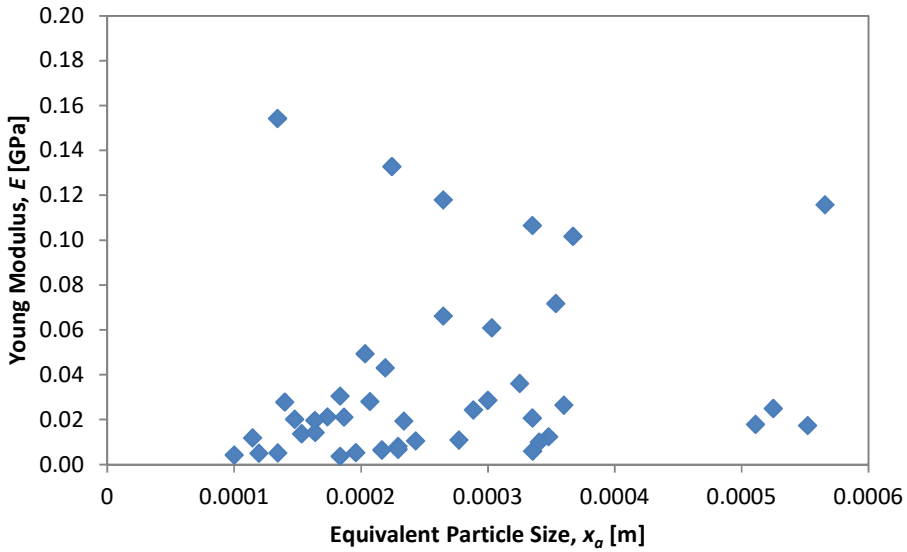

Figure 5.7 The calculated Young's modulus versus its respective particle size of HiLAS 70 particles

The *E* derived from Equation (2.6) was plotted against the equivalent diameter of the compressed particle (Figure 5.7). It is noted that there is no clear trend between the Young's modulus estimated with the Hertz model and the particle size, and the results are scattered across the particle size range. This was probably due to the poor fit of the Hertz model, which resulted in the deviation from the experiments as previously mentioned. In view of this, the Young's modulus of the single surfactant particles can only be considered to be very appropriate.

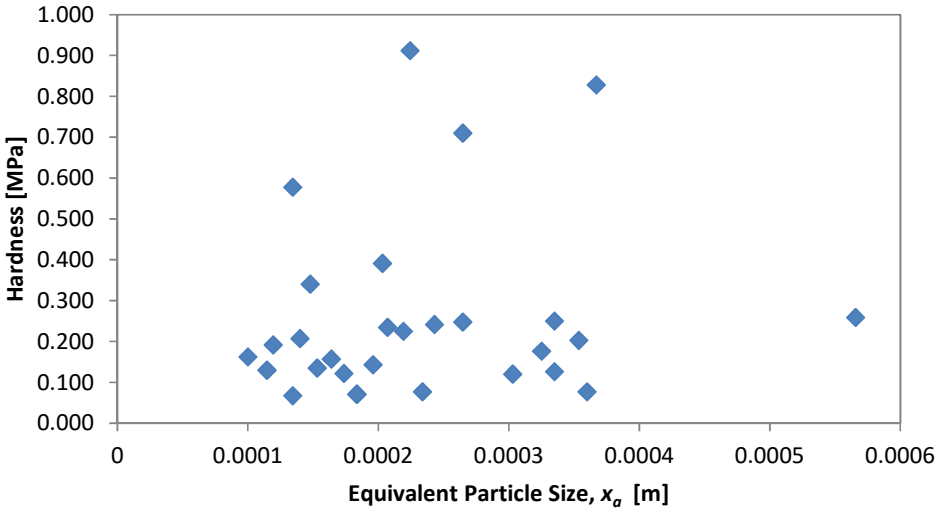

Figure 5.8 The derived hardness of the particle, based on measurement of 30 HiLAS 70 particles.

The gradient of the line of best fit for the first part of the compression data (strain < 0.2) of the single particles was used to calculate their hardness using Equation (2.24), and the results are presented in Figure 5.8. Similarly, with the calculated Young's modulus, the results are scattered across the range of different particle sizes. In view of this, in order to eliminate the variations resulting from the compression of the single particles, bulk compression was used instead. Furthermore, the micromanipulation system can be upgraded in order to better quantify the surface area in contact with the compressing particle.

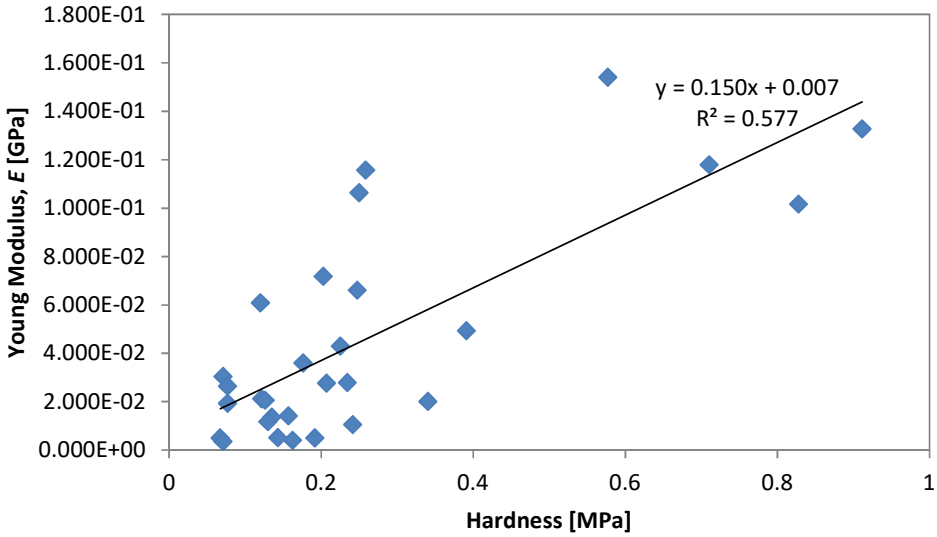

Figure 5.9 Derived Young's modulus and the respective hardness of HiLAS 70 powder

In Figure 5.9, the Young's modulus values obtained for the HiLAS 70 powder were plotted against the calculated hardness values, and a proportional trend can be observed, although the linear line of best fit had a low regression value. This was due to experimental error, as previously reported. The plot shows that the Young's modulus increased as the hardness of the particle increased. A similar proportional relationship between hardness and Young's modulus was also observed by Sonnergaard (1999) and Yap *et al.* (2008), with various powdered materials. It was previously shown by Yap *et al.* (2008) that an increase in hardness will result in an increase in Young's Modulus.

5.2.5 Flowability of the highly concentrated surfactant powder

Subsequently, the flow behaviour of the different powder systems was experimentally quantified by measuring the flowability index, ff_c. The results are presented in Figure 5.10.

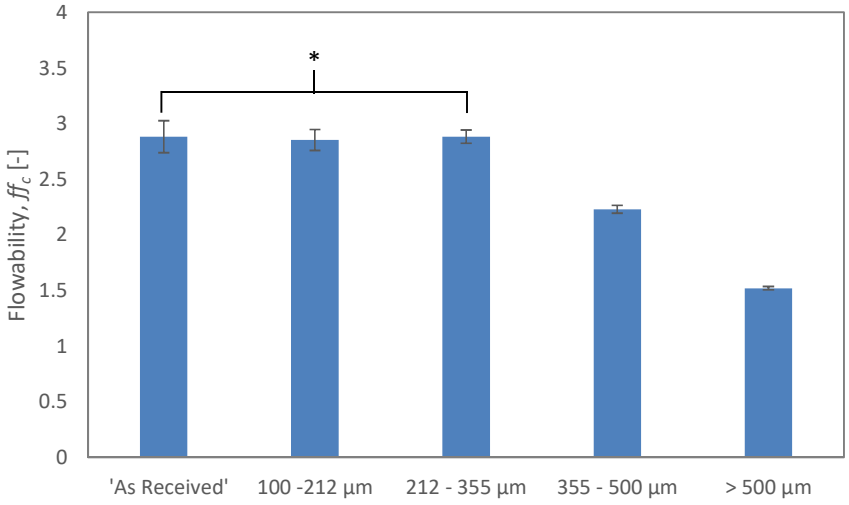

Figure 5.10 The flowability of the different size ranges and "as received". Data analysed with the ANOVA post-hoc Tukey test ($p < 0.05$, two-tailed) where * represents similarity.

By using statistical analysis with a 95% confidence level, it was found that particles with size ranges 100–212 µm, and 212–355 µm had similar flowability, while those of 355–500 µm had a lower flowability, and those > 500 µm had the least. Based on Equation (2.40), larger particle sizes will have better flowability (Liu, et al., 2008; Seville, et al., 2000), but the results in Figure 5.10 show otherwise. These results concur with the data presented by Hart (2015) where smaller washing powder granulates had better flowability. He also showed that the flowability of the powder was related to the hardness of the particles. In Hart (2015), the flowability of

the powder was compared with the compressibility of the particles, and it was found that the flowability decreased as the compressibility of the particles reduced. In addition, it was found that the flowability of the highly concentrated surfactant powders was in the cohesion regions ($1 < ff_c < 4$).

5.2.6 Correlation between particles' characteristics and flowability

An existing correlation (2.3) was first employed to fit the experimental data (see Figure 5.11). The minimum diameter $d_{V,min}$ in Equation (2.4) was represented by $d_{v,10}$ for the calculation. It is based on the fact that the smaller particles contribute more to the flowability issue than large particles, as their larger surface area per volume results in higher vdW force (Seville, et al., 2000).

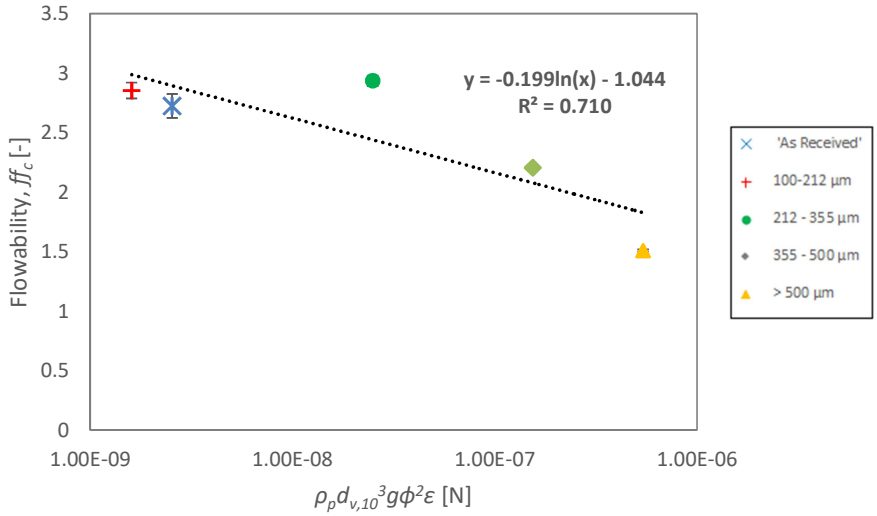

Figure 5.11 The flowability of the surfactant granulates of different size ranges in relation to the particle property parameters, as shown in Equation (2.4).

Contrary to the observation made by Liu et al. (2008), the results in Figure 5 show that for the same material (surfactant powder) with different size

ranges, the flowability decreased with the natural log of parameters, $\rho_p d_{v,10}^3 g\phi^2\varepsilon$. This could be due to a significant difference in powder cohesive characteristics between both experiments. Whilst Liu et al. (2008) demonstrated that the flowability of the powders used was between the easy-flow and free-flow regions, the particles used in this experiment were in the very cohesive region (ff_c between 1.5 to 3).

The cohesiveness of the particles could also be due to a sintering mechanism, whereby particles deform elastically and then plastically, which contributes to the inter-particle force. As a result, as shown in Figure 5.3, the particles in the smallest size range had the highest K^{-1} value (highest resistance to deformation), and thus these particles theoretically generated less adhesive force than particles larger than 500 μm, according to Equation (2.3).

The experimental results suggest that deformation of the surfactant powder might play an important role in its flowability, and hence, the correlation between the particle characteristics and flowability shown in Equation (2.3) would not be sufficient. It is therefore proposed to estimate the adhesive force generated using the Hamaker summation method to predict the adhesion due to the deformation of the particles, as shown in Equation (2.40). Along with Hertz's estimation of the contact radius from Equation (2.7), the following correlation can be derived:

$$F_D = \frac{\left(\frac{R_E}{E} F_N\right)^{\frac{2}{3}} C_H}{6a_o^3} \tag{5.5}$$

Subsequently, for the same material (LAS and acetate acid salt), the Hamaker constant and the minimal contact distance are considered to be similar among the different samples. Thus, by neglecting C_H and a_o and also assuming that the weight of the powder itself is the only normal force that the powder bed is experiencing, the following Equation (5.6) is obtained.

$$F_D \propto \frac{\left(\frac{R_E}{E} F_N\right)^{\frac{2}{3}}}{6} \tag{5.6}$$

Following this, it can be assumed that the normal force experienced by the powder is only contributed by its own weight ($r^3_{mean} \times \rho_p \times (1-\varepsilon) \times g$), and that by replacing the elastic modulus with hardness (represented by the Heckel parameter) since the former increased with the latter (Sonnergaard, 1999; Yap, et al., 2008), Equation (5.4) can be further modified to Equation (5.7):

$$x_{ad} = \left(\frac{r^4_{mean}}{K^{-1}} \rho_p (1-\varepsilon) g\right)^{\frac{2}{3}} \tag{5.7}$$

where x_{ad} represents the coefficient of adhesion due to plastic deformation.

Herein, r_{mean} is used to represent the wide particle size range instead of R_E, as it is more representative of the different particles in contact with each other. Subsequently, the flowability values of all the particle samples versus the derived x_{ad} values were then plotted, as illustrated in Figure 5.12.

Because the particle surfaces of the samples were chemically similar, and their surface roughness were not significantly different except for the sample with size > 500 μm (see Figure 5.1), the decreasing flowability with increasing particle size was attributed to greater deformation at their contact between bigger particles, resulting in greater adhesion. In line with the sintering theory, particles that deform more easily can be more adhesive, as the inner structures collapse and the particles' structure and shape will be lost. The deformation can result in a stronger vdW force and the creation of amorphous bridges, leading to a decrease in flowability.

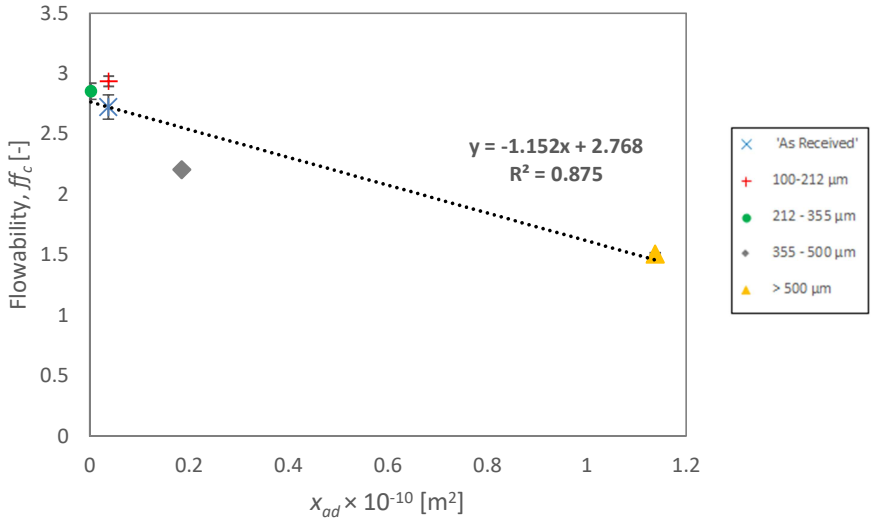

Figure 5.12 The correlation between the flowability and the adhesive term, described by Equation (5.7).

In addition, it was observed from Figure 5.12 that particles with a size range of 100–212 μm had a similar adhesion value to the 212–355 μm particles and the powder as received. This is probably due to the greater influence of the particle size rather than the material properties of the powder. As a result, even with relatively higher resistance to deformation,

the particles in the size range of 212–355 μm, “as received” (as shown in Figure 5.3), and those of 100–212 μm had similar adhesion and flowability values.

In order to develop a new model to predict the flowability of particles with different sizes, it is suggested to compare the adhesion between particles and the ability of them to flow due to gravity. In theory, if the gravitational force is greater than the adhesion, the powder should flow. Accordingly, Equation (5.8) was derived to represent the ratio between the driving force and the resistance to flow:

$$ff_c \alpha \frac{\rho_p d_v^3 g \phi^2 \varepsilon}{x_{ad}} \tag{5.8}$$

The equation also accounts for the particles’ sphericity, which can lead to a possible interlocking mechanism and their voidage. In addition, this model predicts that the particles should flow more easily if the ratio on the right-hand side is greater. The experimental flowability data were plotted against particle property parameters described in Equation (5.8), as shown in Figure 5.13.

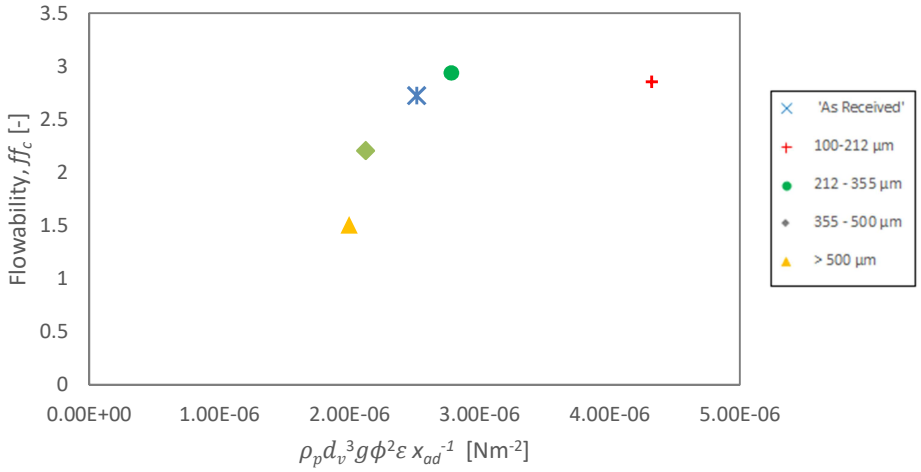

Figure 5.13. The flowability versus the ratio of the gravitational driving force to the deformation resistance force described in the correlation (5.8).

As predicted, the increase in the ratio on the right-hand side of Equation (5.8) enhanced the flow of the particles. However, the rate of increase declined as the ratio increased. When the ratio was approximately 2.8 × 10^4, the increase in ratio did not improve the flowability anymore. Again, as mentioned in the previous discussion, the particles in the 100–212 µm sample had similar x_{ad} values to the 212–355 µm and "as received" samples, although they had the highest material hardness. It can therefore be deduced that when the particle size reduced, the vdW force became the dominant factor on the flowability over the gravitational force, as discussed by Seville (2000). It is indicated that when the size, r_{mean}, of the highly concentrated surfactant particles was smaller than approximately 125 µm, vdW force was the dominant factor in determining the flowability of the powder.

It has been demonstrated that the new correlation was more robust than Equation (2.4) in modelling the flowability of the soft particles. The novel

correlation includes an additional material property, namely the hardness, in the prediction of the flowability by comparing the adhesion and the ability of flow due to gravity. It should be noted that the surface roughness was not considered in this correlation, as the difference between the different samples was not significant enough for such a comparison

Despite the above, the novel model does not account for the different chemical properties of the particles. Different composition of the particle surface can result in a change in adhesion due to vdW forces. Another shortcoming using this correlation is a lack of consideration of the crystalline structure on the surface. These parameters can also contribute to the adhesion between the particles. In addition, the effect of humidity on flowability has not been considered. Further research is required to improve the model by including different chemical properties, crystalline structure, surface topology, and also to understand the impact of humidity on the material property of the particles.

5.3 Conclusions

The effects of the physical characteristics on the flow behaviour of highly concentrated surfactant granulates of different size ranges were studied. The results showed that the correlation between the flowability and the particle characteristics developed by Liu *et al.* (2008) was not sufficient. It was also found that the larger particles in a powder sample (> 500 μm) had the worst flowability. These results were likely to be due to the difference in the material hardness of the surfactant particles between

samples, where the > 500 μm particles appeared to deform more easily. The low Heckel parameter value possibly resulted in increased adhesion among the particles via a sintering mechanism.

An improved correlation was developed, which takes the material hardness of the powder system into consideration. Subsequently, it was demonstrated that the newly derived correlation (5.8) better fitted the relationship between the flowability of the particles and their physical characteristics. It was found that for the highly concentrated surfactant powder system, the vdW force was not significant when the particle size was smaller than 250 μm. In addition, it has also been shown that adhesion due to deformation might be less significant as particle size decreased, since smaller particles showed greater hardness. The mechanical properties of the surfactant powders were also investigated by compressing single particles. It was found that the irregularity in shape and uneven surfaces resulted in a low coefficient of determination for the line of best fit. As a result, no trend could be identified from the experiments, and the results were scattered across the different particle sizes.

Future work includes understanding the effects of the surface chemical properties, crystalline structure, surface roughness, and humidity of particles on their flowability.

Chapter 6. Improving the Flowability of Adhesive Soft Powders

In previous chapters, it has been shown that the flowability of adhesive surfactant powders is affected by hardness, and hence, in order to improve the flowability of the highly concentrated surfactant powders, the hardness of the powders has to be enhanced. This will reduce the deformation (elastically and plastically) and reduce the adhesion caused by the sintering mechanism. In this chapter, the research presented aims to investigate the possibility of achieving improvement in powder flowability through salt coating using a fluidised bed. The salt chosen for this experiment was potassium chloride, as it is readily available and can be easily integrated into the formulation.

6.1 Materials and Methods

As previously mentioned, many parameters could affect the quality of the coating. However, in this study, the focus was not on the effects of the fluidised bed parameters on the coating quality, and so a constant set of parameters were implemented across all the coating experiments.

6.1.1 Materials and Properties Measured

HiLAS 33, supplied by P&G (Newcastle), was used as the surfactant powder and the core particles for the study presented in this chapter. Potassium chloride was used as the coating material. (See Section 3.1 for more details.) The physical properties, such as size (Section 3.4),

mechanical properties of the bulk powder (Section 3.9.1), surface roughness (Section 3.6) and hygroscopicity (Section 3.5) were investigated. Images, composition and coating coverage were also determined using method found in Section 3.7.

6.1.2 **Coating of the surfactant powder**

A Glatt® mini fluidised bed coater, as previous mentioned in Chapter 3, was used for the coating process where a coating solution (20 wt% KCl solution) was injected into the fluidised bed via a syringe pump, Pico Plus Elite (Harvard Apparatus, USA), at a rate of 100 µl min^{-1}. The coating solution was atomised by mixing with a stream of air flowing at 0.5 m^3 hr^{-1} in the nozzle (nozzle diameter = 0.5 m). In addition, 30 g of the HiLAS 33 (core particle) was placed in the product container before the coating process. The system was operated under a pressure of 5 bars and a temperature of 50°C. During the process, a stream of compressed air was introduced into the system at a flow rate of 30 m^3 hr^{-1}. The compressed air velocity was set to ensure sufficient distribution in the fluidised zone and enough energy to break any binding between core particles, in order to prevent agglomeration and to promote coating process.

Different amounts of coating material were applied onto the core material. The range of KCl (shell) to HiLAS 33 (core) weight ratios used was 0.01–0.2. Triplicate coating experiments were undertaken to ensure reproducibility. In order to ensure consistency in the results, the samples were stored and conditioned in a controlled environment at a temperature of 30°C and a relative humidity of 30% before being analysed.

A set of blank samples was created to eliminate the effect of attrition and fragmentation due to the coating process. The controlled sample was produced by placing 30 g of the core material in the fluidised bed under the same conditions without coating solution for a period of 1 hour.

6.1.3 Flowability

The flowability of the bulk powder under high consolidation stress was determined using the ring shear tester under a pre-shear pressure of 20 kPa. Refer to Section 3.11 for more detail on the equipment and procedures.

6.2 Results and Discussion

6.2.1 Particle surface coverage

In an attempt to enhance the flowability of the surfactant powder, the particles were coated with potassium chloride in a fluidised bed coater (Glatt® Mini, Germany). In Figure 6.1, an example of the coated particles with potassium chloride is shown. The image was taken using an SEM with 15 kV charged electrons. With back-scattered electrons, two different contrast surfaces could be clearly observed. The patch with brighter contrast was the potassium chloride coating, as the elements have higher atomic numbers, which will appear brighter (Voutou, et al., 2008). A close-up image of the coated region is shown in Figure 6.2. It appeared as if the coated salt crystallised through a tetragonal crystal system during the process.

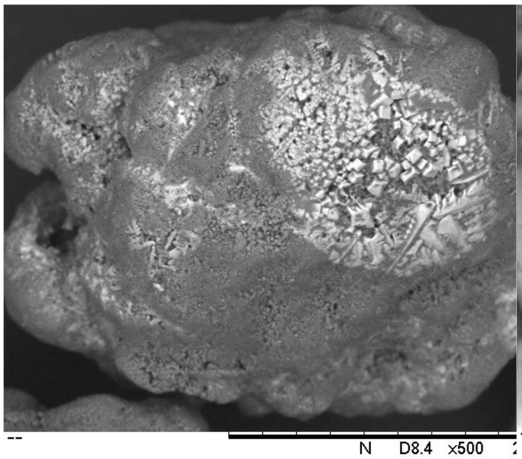

Figure 6.1 SEM image of a HiLAS 33 particle with coating (shell-to-core mass ratio 0.07). The scale bar is 200μm in total.

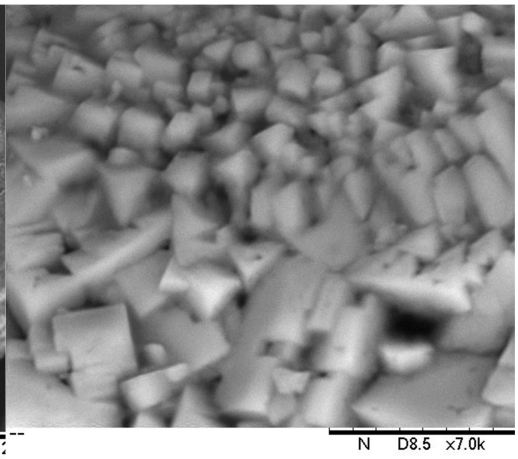

Figure 6.2 A closer-up SEM image of a HiLAS 33 particle with coating (shell-to-core mass ratio 0.07). The scale bar is 10 μm in total.

Furthermore, the image of the full particle shows that it was difficult to determine the total surface area of the particle and the area that was covered by the salt through the coating process. In view of this, an image of a cross section of the particle was taken, as displayed in Figure 6.3 and Figure 6.4, in order to qualify the coverage of the coating. Both of the images were taken using SEM coupled with energy-dispersive X-ray spectroscopy. In addition, the coating thickness was quantified by averaging the measured distance perpendicularly away from the surface of the particles, with 20 of such measurements for each particle analysed.

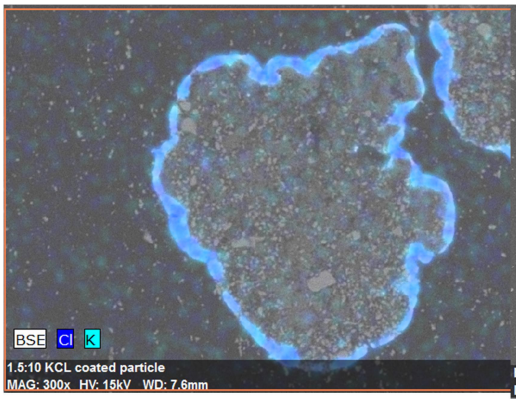

Figure 6.3 Cross-sectional EDX image of a HiLAS 33 particle with coating (shell-to-core mass ratio 0.15)

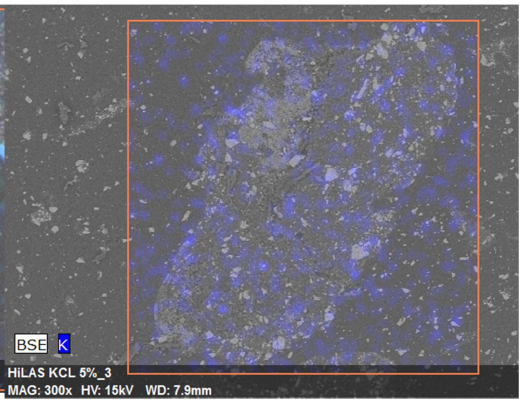

Figure 6.4 Cross-sectional EDX image of a HiLAS 33 particle with coating (shell-to-core mass ratio 0.05)

Figure 6.4 and Figure 6.5 show the cross-section of the HiLAS 33 after the cured moulds that the particles were placed in were polished with sandpaper. In Figure 6.3, the coating layer can be clearly observed around the particle. By using the imaging analysis software ImageJ, the perimeter of the particle and where the coating was present were determined. The surface coverage of the particle was then derived from the squared value of the ratio between the coating and total perimeter. In Figure 6.3 and Figure 6.4, noise can be observed from the coloured dots around the particles. This deviation might be due to the polishing process of the mould that embodied the particles in order to obtain the cross-section images. Residues and contamination from the sandpaper were caught on the surface of the mould, which were later detected as noise in the imaging process. In addition, the noise could also have been contributed by the overlapping energy of potassium and chloride with carbon, as illustrated in Figure 6.5.

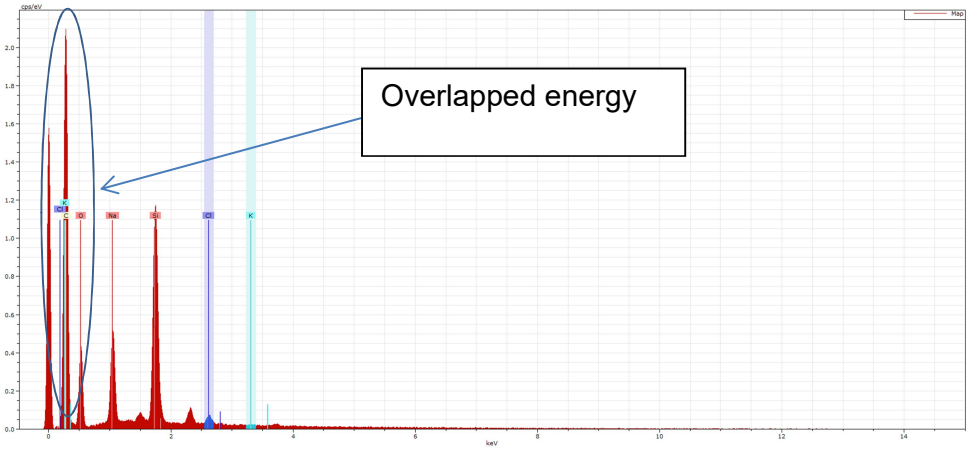

Figure 6.5 A sample of an element analysis obtained from S.E.M, EDX. The graph shows the surface composition of an uncoated HiLAS 33 particle.

The coverage of the core particles for shell-to-core mass ratios below 0.05 also proved to be a challenge due to the limitation of the equipment used in obtaining the surface composition of the sample. The coverage was determined by using the cross-sectional EDS images, as shown in Figure 6.3, to derive the total perimeter. However, as the coating material decreased to shell-to-core mass ratios of less than 0.05, it was hard to differentiate between the coated material and the noise, as shown in Figure 6.4.

Table 6.1 Summary of the coverage and thickness of the coating of HiLAS 33.

Shell-to-core mass ratio	**Blank**	**0.01**	**0.02**	**0.05**	**0.07**	**0.10**	**0.15**	**0.20**
Coverage [-]	-	-	-	-	0.52 ± 0.12	0.83 ± 0.15	1	1
Thickness [µm]	-	-	-	-	-	-	5.25 ± 0.32	5.66 ± 0.43
Theoretical Thickness [µm]	-	0.46	0.92	2.27	3.16	4.49	6.64	8.73

The coverage and thickness of the coating material were analysed and are summarised in Table 6.1. “Blank” refers to the uncoated HiLAS 33 powder. The theoretical thickness, calculated with the assumption that the particles were all spherical and of uniform size, and that all coating material was applied uniformly onto the surface of the core particles, is also shown in the table. The theoretical values of the coating were calculated using the mass of the coating material introduced and the density of the material. It was assumed that the core particle was a perfect sphere.

The analysis indicates that full coating was only achieved when sufficient coating material (shell-to-core mass ratio > 0.15) was injected into the fluidised bed. In comparison with the theoretical values, some KCl was lost in the coating process. This could be due to the high atomising gas velocity and operating temperature. These resulted in smaller droplets, which were subject to high evaporation at the elevated temperature. As a result, the salt crystallised before attaching onto the surface of the core material. These small amounts of crystallised salt could be lost by exiting the fluidised bed, as they would have a small particle size.

Furthermore, the difference was also caused by the irregular shape of the core particles and the presence of cracks on the surface of the powder. This could result in more coating material being deposited within the cracks or in the cavities on the surface to produce a more spherical structure. The coated material could also be removed through attrition in the fluidised bed due to the high gas/particle flow velocities generating

hydrodynamic forces within the system. This effect could be clearly observed in Figure 6.3, where the coating was irregular and thicker around the area with cavities.

6.2.2 Size, shape, particle density, and surface roughness of the uncoated and coated particles

Table 6.2 Particle characteristics of the uncoated and KCl-coated HiLAS particles.

Shell-to-Core Mass Ratio	**BLANK**	**0.01**	**0.02**	**0.05**	**0.07**	**0.10**	**0.15**	**0.20**
$D_{3,2}$ [µM]	298.9 ± 17.6	299.8 ± 17.2	325.3 ± 1.7	323.3 ± 15.3	330.1 ± 37.8	326.6 ± 12.6	331.5 ± 16.7	337.7 ± 16.2
Span [-]	0.77	0.68	0.88	0.64	0.63	0.64	0.65	0.66
Sphericity [-]	0.68	0.69	0.68	0.67	0.68	0.68	0.68	0.68
Density [g cm^{-3}]	1.82	1.82	1.82	1.83	1.83	1.83	1.83	1.83
S_A [µM]	12.3	13.7	12.8	12.7	13.2	14.1	14.3	13.9

Table 6.2 shows the results obtained from the particle sizing, shape analysis, density measurement, and surface roughness evaluation. The errors presented are twice the standard error derived from the obtained data. The variations in the particle size were due to different batches of particles produced each time from the fluidised bed. It can be observed that the particle sizes were similar when the shell-to-core mass ratio ranged from 0.02–0.2; however, they were roughly 20 µm smaller for the blank and the sample, corresponding to a shell-to-core mass ratio of 0.01. In addition, in comparison with the particle size of the raw particles shown in Table 4.1, the blank sample had a smaller d_{32}. This was due to the attrition caused by the high hydrodynamic forces experienced by the particles in the fluidised bed. Moreover, the span of the blank sample was

also wider than for the raw HiLAS 33. This suggests that other than attrition, there might be some agglomerates that fractured in the process, forming much smaller particles.

The density of the particles, shown in Table 6.2, refers to the true density of the powder. Helium gas was used in determining the true density. The results show that the density of the particles did not vary with the different samples.

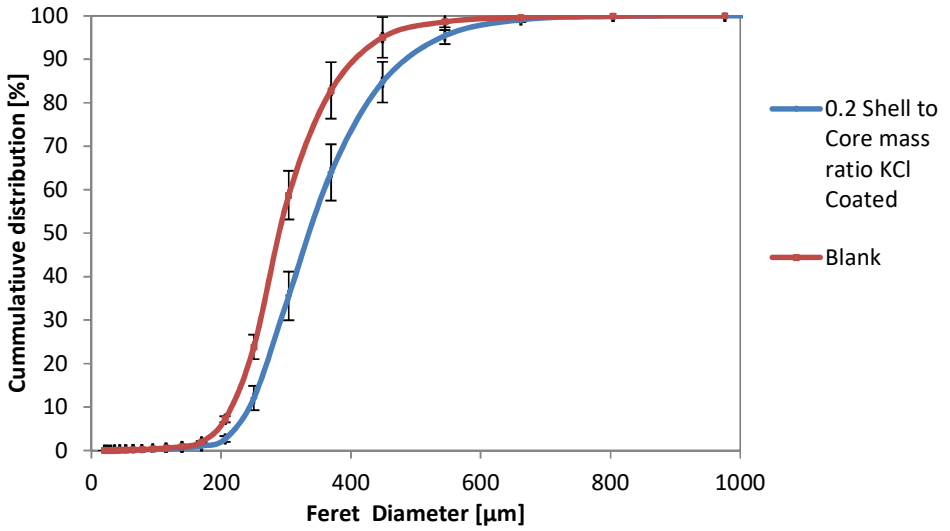

Figure 6.6 Particle size distributions of uncoated particles (Blank) and KCl-coated HiLAS particles (shell-to-core mass ratio 0.2)

In order to ensure that the coating process was the primary occurrence in the fluidised bed, the cumulative size distributions of the brank and KCl-coated HiLAS samples are shown in Figure 6.6. It is to be noted that the Feret diameter was used instead of surface-to-volume equivalent diameter. This was to ensure that the diameter was well represented, in order to check whether the particles were not twice as long on the longer end, which would suggest agglomeration. The curves suggest that most of

the KCl-coated particles increased in size by a fraction from the blank sample. It was thus deduced that the main mechanism of size enlargement in the fluidised bed was due to coating.

The sphericity of the median particle size was used to represent the shape of the different samples. No significant difference in shape between the bland and KCl-coated particles was observed. In addition, the particle densities of the different samples obtained using the helium pycnometer exhibited no significant variation. Lastly, the surface characteristics did not vary much after the coating process. However, a difference in the surface roughness was observed between the blank sample and the raw HiLAS 33, as shown in Table 4.1. The reduction in surface roughness of the blank particles was considered to be due to the coating process in the fluidised bed, wherein particles were placed under high hydrodynamic forces that smoothen the surface of the particles, resulting in more spherical particles, as the sphericity of the blank sample was higher than that of the raw HiLAS 33.

6.2.3 **Mechanical properties of the coated particles**

6.2.3.1 Adams model

The force/displacement data obtained from the compression process was converted to a stress and strain relationship, which was fitted to the Adams model as shown in Figure 6.7. It demonstrates that the compression process did not fit well with Adams model, and two regions can be observed. Samimi (2005) demonstrated in the first non-linear

region (ε_n < 0.3), the particles experienced elastic deformation while the powder deformed plasticity in the second linear stage of the compression.

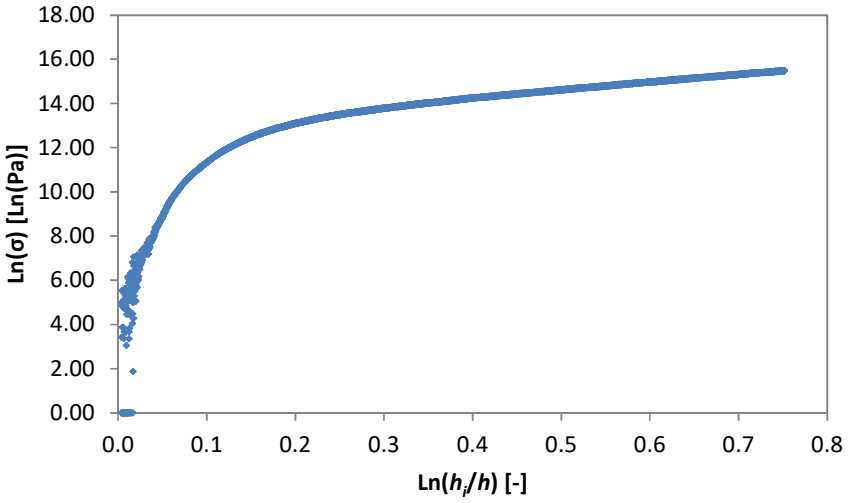

Figure 6.7 Compression data of KCl-coated surfactant particles in a powder bed (shell-to-core mass ratio of 0.15 and aspect ratio of 0.1) fitted to Adams' model.

Therefore, the linear region of the relationship was used, as shown in Figure 6.8, to determine the Adams' parameter. In addition, the second region with high strain was used due to the fact that the term, $ln(1 - e^{-\alpha' \varepsilon_n})$ in Equation (2.54), was assumed to be negligible as the natural strain was large (ε_n > 0.2) (Yap, et al., 2008). In Figure 6.8, it shows that by using the plastic region, high regression can be obtained from the best fit linear curve.

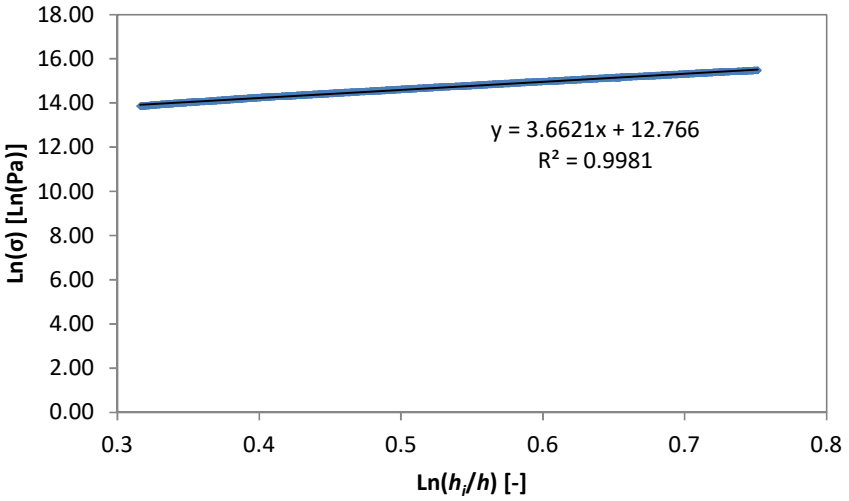

Figure 6.8 The linear region of Figure 6.7 used to derive the Adams parameters.

Subsequently, the values of the y-axis interception and gradient of the best fitted linear line were used to derive the apparent coefficient of friction, α', and the apparent strength of the particles, τ_o'. The calculated values of the apparent strength of the different samples were then presented in Figure 6.9.

In Figure 6.9, it was shown that the 0.15 shell to core KCl coated surfactant powder has the highest apparent strength while the 0.01 to 0.10 shell to core ratio coated samples demonstrated deterioration or similar in apparent strength in comparison with the uncoated blank samples. Therefore, from the Adams parameters, the enhancement of the particle apparent strength can only be achieved when the coating of the salt reaches more than 0.15 shell to core ratio, or when the particles are fully coated (i.e. 100% surface coverage). However, it was also demonstrated that excess coating material did not further increase the apparent strength of the sample.

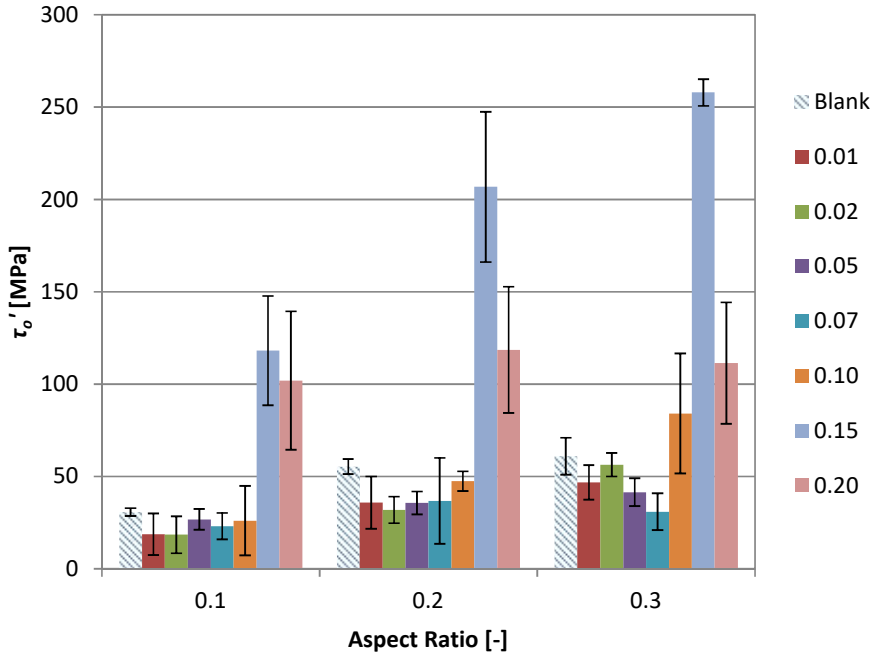

Figure 6.9 τ_o value of the different samples derived from compression curves fitted to the Adams model. The legends describe the different samples and the values represent the shell-to-core mass ratio. The error bars represent twice the standard errors of the mean from nine repetitions.

6.2.3.2 Kawakita's Model

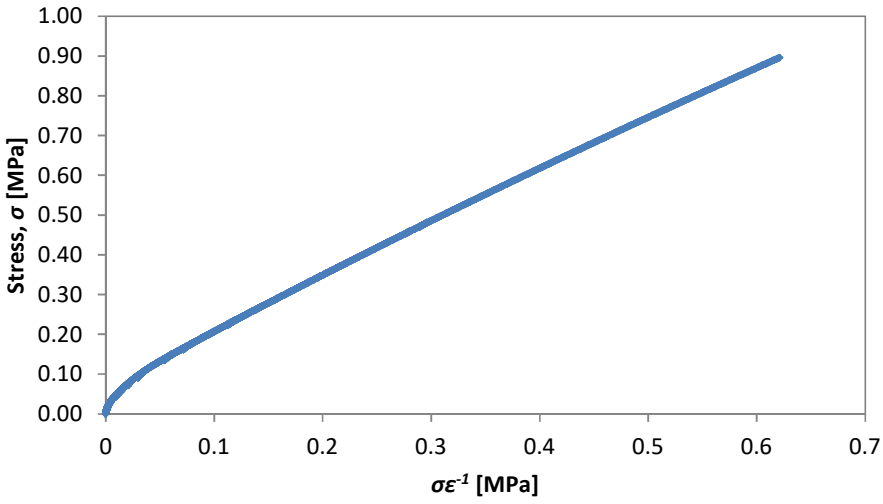

Figure 6.10 Compression data of KCl-coated surfactant particles in a powder bed (shell-to-core mass ratio of 0.1 and aspect ratio of 0.1) fitted to the Kawakita model.

On the other hand, the data fitted to the Kawakita model, as illustrated in Figure 6.10, shows a much more linear relationship throughout the whole compression stress/strain than the Adams Model. However, a non-linear region can be still observed at the beginning of the compression when $\sigma\varepsilon^{-1}$ is less than 0.1. Likewise to the Adams Model, during the initial stage of the compression, the powder experienced elastic deformation and this represented by this non-linear region. Therefore, only the linear region, as shown in Figure 6.11, was used to derive the Kawakita parameters.

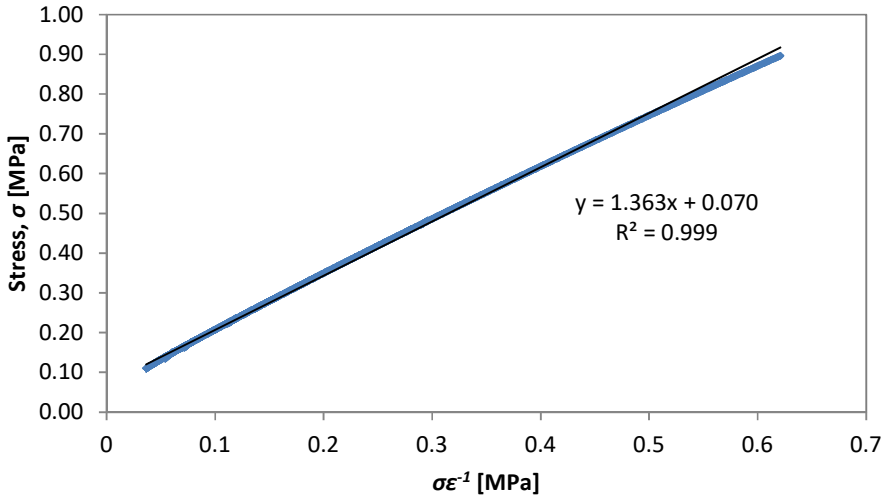

Figure 6.11 The linear region of used to derive the Kawakita parameters.

The constant a and b^{-1} parameters for different samples were calculated from the gradient and interception of the best fitted linear curve and are presented in Figure 6.12 and Figure 6.13 respectively.

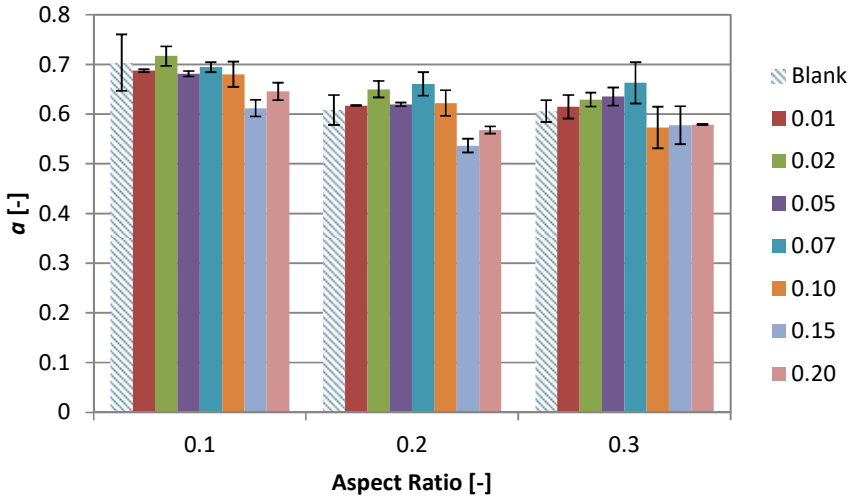

Figure 6.12 *a* value of the different samples derived from compression curves fitted to the Kawakita model. The legends describe the different samples and the values represent the shell-to-core mass ratio. The error bars represent twice the standard errors of the mean from nine repetitions.

From Figure 6.12, it can be observed that the blank sample and KCl-coated samples for shell-to-core mass ratios less than 0.1 had similar a values, which reflect the packing of the particles during the compression. On the other hand, the coated samples for shell-to-core mass ratios of 0.15 and 0.2 had lowered *a* values, especially for aspect ratios of 0.2 and 0.3. This could be due to the size of the particles, as larger particles resulted in higher bulk density. This effect was more obvious when the samples' volume increased as the aspect ratio increased. Furthermore, the *a* values of the different samples are similar across the different aspect ratios that occurred with the results as demonstrated in Chapter 4.

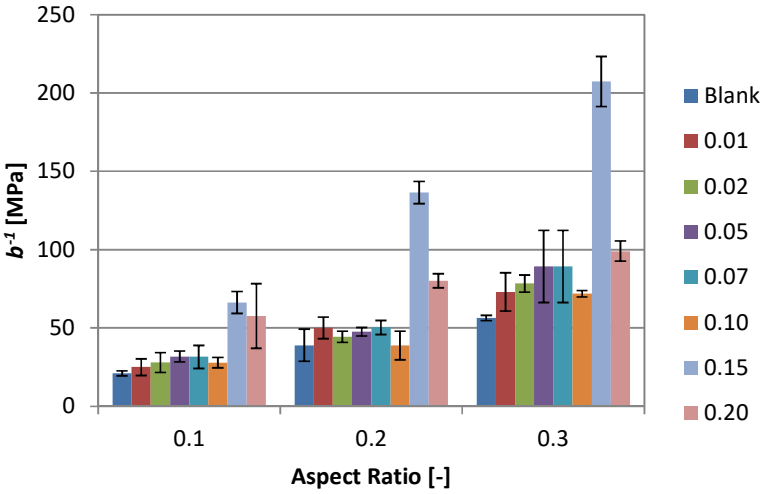

Figure 6.13 b^{-1} values of the different samples derived from compression curves fitted to the Kawakita model. The legends describe the different samples and the values represent the shell-to-core mass ratio. The error bars represent twice the standard errors of the mean from nine repetitions.

The b^{-1} was calculated from the intercept on the vertical axis of the fitted straight line. The results show that there are two groups with regard to the b^{-1} values: those corresponding to a shell-to-core mass ratios of 0.15 and 0.20, and all the others. The group corresponding to a shell-to-core mass ratio of 0.15 had the highest b^{-1} values, particularly for aspect ratios of 0.2 and 0.3. Referring to Table 6.2, it shows that the KCl coated particles for a shell-to-core mass ratio of 0.15 had the roughest surface. This indicates the b^{-1} reflects not only the fracture strength of the primary particles but also the surface roughness, which could increase the energy required during the compression due to the friction forces between the particles and the wall, and among the particles. The difference in the surface topology can be observed in Figure 6.14, taken using an SEM with back-scattered electrons. The smoother surface of the KCl-coated particles shown in Figure 6.11(b) could result from the particles experiencing a longer period

of coating time and attrition in the fluidised bed. This can be observed from the comparison of the uncoated HiLAS 33 shown in Figure 4.3 (a).

a) b)

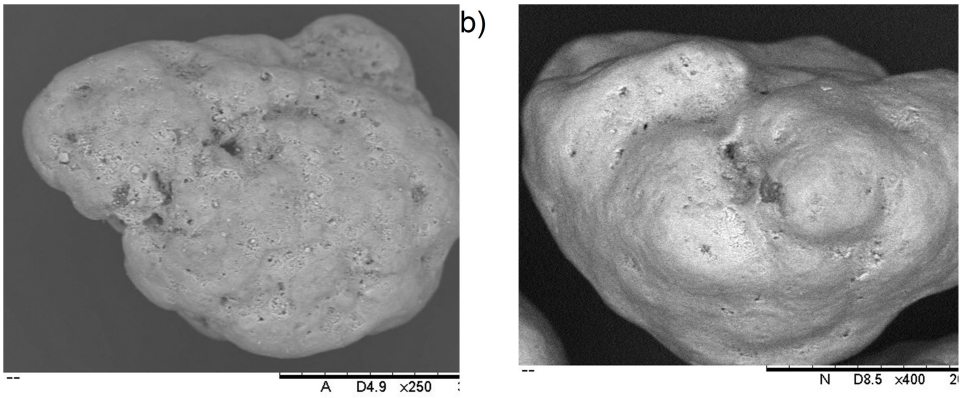

Figure 6.14 Image of a) 0.15 shell-to-core mass ratio KCl-coated particles, and b) 0.20 shell-to-core mass ratio KCl-coated particles, taken using S.E.M. The image was taken with back-scattered electrons at 15 kV in a highly vacuumed environment.

Furthermore, it can be observed in Figure 6.13 that the b^{-1} values increased with the aspect ratio, similarly to compression of the raw HiLAS 33 and HiLAS 70. This again suggests that the b^{-1} value indicates not only the failure stress of the particles but also the friction between the particles and the wall.

From Figure 6.13, it can be concluded that salt coating successfully enhanced the mechanical strength. This was reflected by the significant higher b^{-1} value of the 0.15 shell-to-core mass ratio KCl-coated particles in comparison with the blank sample. Mass-coated particles with a shell-to-core ratio of 0.2 also have higher fracture strength when compared with the blank sample.

6.2.3.3 Heckel Model

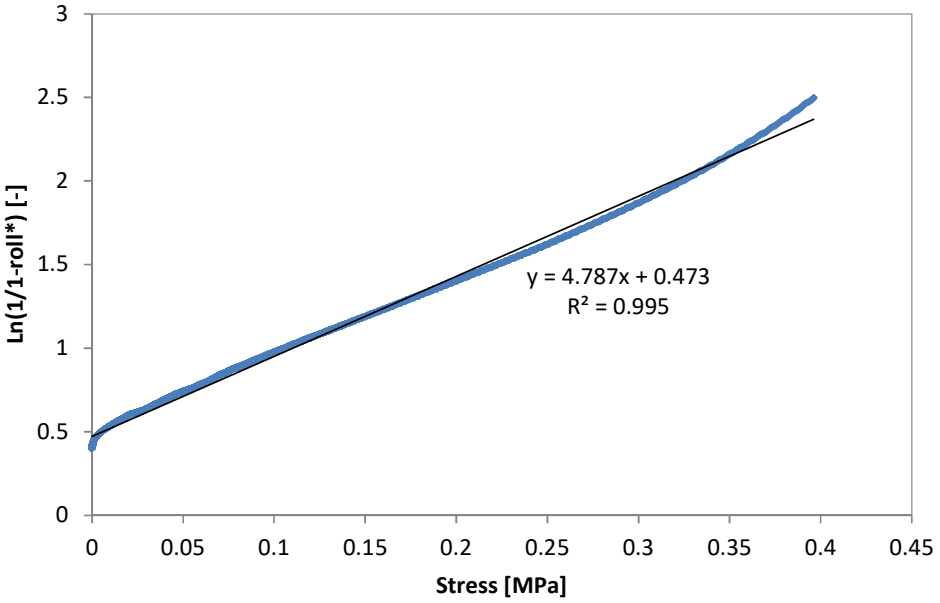

Figure 6.15 Compression data of KCl-coated surfactant particles in a powder bed (shell-to-core mass ratio of 0.05 and aspect ratio of 0.1) fitted to the Heckel model

The force/displacement data obtained from the compression process were fitted into the Heckel model as shown in Figure 6.15. The curve clearly illustrates three different regions, similar to those found in Chapter 4, as shown in Figure 6.16.

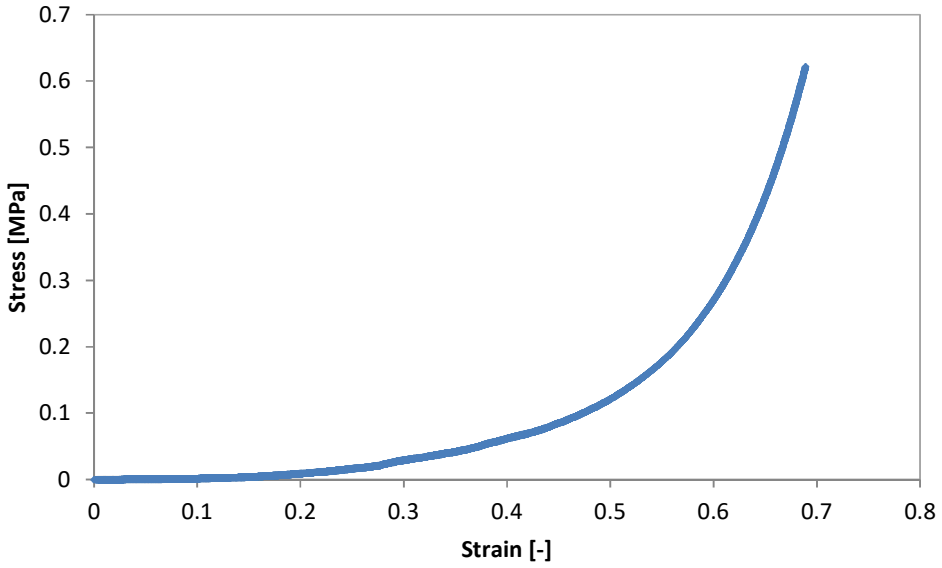

Figure 6.16 Stress/strain relationship of KCl-coated surfactant particles in a powder bed (shell-to-core mass ratio of 0.05 and aspect ratio of 0.1).

Initially, a sharp gradient can be observed, and this was attributed to the rearrangement of the particles. The sliding movement of the particles rapidly increased the bulk density of the sample. Subsequently, a linear line can be seen until the material structure failed and a steep deviation from the straight line was again observed. The Heckel parameters were derived from the gradient of the linear section of the curve, the average coefficient of determination being 0.99 ± 0.006.

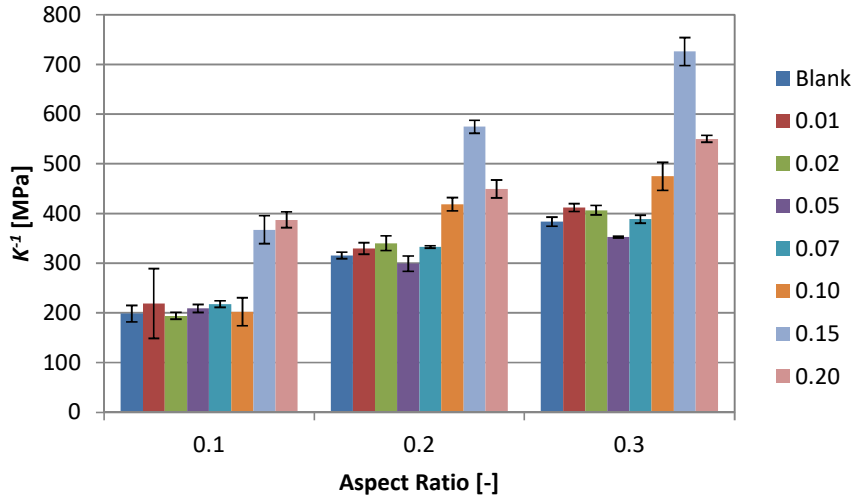

Figure 6.17 The derived Heckel parameters of uncoated and coated samples. The legends on the right indicate the shell-to-core mass ratios. The error bars represent twice the standard error of the mean.

Figure 6.17 presents the Heckel parameters of all the different coated samples derived from the gradient of the fitted curve as shown in Figure 6.15. Likewise, in comparison with the trend found with the Kawakita model, it shows that the sample corresponding to a shell-to-core mass ratio of 0.15 had the highest K^{-1} values with aspect ratios of 0.2 and 0.3. Furthermore, for an aspect ratio of 0.1, the Heckel parameter values for the two shell-to-core mass ratios were similar, which was also observed from the results using the Kawakita model. The other samples had similar parameter values.

In addition to the above, it was clear that the Heckel parameter directly increased the depth of the powder bed. This was due to increasing interactions between the particles and the wall. It was also shown that the particles were not spherical and that the number of contact points between particles also increased with the aspect ratio. The Heckel parameter thus

indicates not only the hardness of the particles but also the interactions between the particles and the wall. While the literature has shown that the Kawakita parameter was proportional to the Heckel parameter, they can be different depending on the material (Yap, et al., 2008).

6.2.4 Flowability of KCl-coated particles

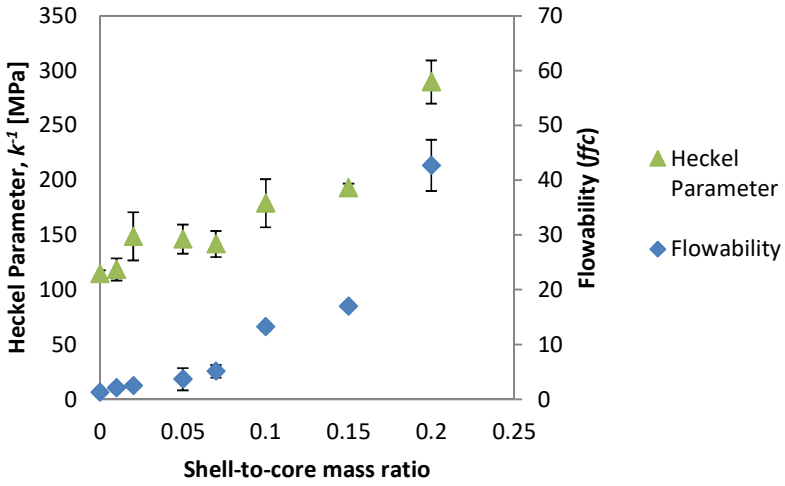

Figure 6.18 Flowability of the particles under a high pre-shear pressure of 20 kPa (diamond symbol) and their corresponding hardness expressed using the Heckel parameter, K^{-1} (triangle symbol). The error bars represented twice the standard error with three repetitions for each experiment.

In Figure 6.18, it shows the flowability of the uncoated and coated samples at a high pre-shear pressure of 20 kPa using a Schulze's ring shear tester. The high pressure was used to induce the worst-case scenario of the sample to flow under conditions the powders can experience under the powder's own weight. The Heckel parameters were derived from the y-interception by plotting the Heckel parameters of respective materials against the aspect ratio. This was to eliminate the effect of wall friction during the compression.

It has been demonstrated that the increase in coating material applied to the core particles, HiLAS 33, enhanced the flowability of the surfactant powder. Significant improvement in the flowability was observed when the shell-to-core mass ratio was greater than 0.10. This suggests that the core particles would have to be coated with a surface coverage of at least 83% in order to gain an improvement in the flowability. With a shell-to-core mass ratio of 0.1, the powder flowability could be improved into the free-flowing region under the high pre-shear pressure.

In Chapter 5, it was demonstrated that the increase in mechanical strength of the small particles led to easier flow of particles. In the experiments presented in this chapter, the samples had similar sizes (between 212 and 355 μm), as displayed in Table 6.2, and the difference between the samples was the degree of coating. When more salt was used to coat the surfactant powder surface, the powder's Heckel parameter value was increased. In Figure 6.18, the relationship between the flowability indexes and Heckel parameters and the amount of coating material applied to the core material was illustrated. It was clear that the flowability increased as the coating material increased as the samples got harder. Significant increases in hardness and flowability were observed when the coating material to core material ratio was more than the 0.1 shell-to-core mass ratio. This was because the reinforced structure increased the force required for plastic and viscoelastic deformation. The reduced deformation minimised contact points between the particles, thus reducing the interaction between them. The reduction in deformation also lowered the

effect of mechanical interlocking, which could also diminish the flowability (Tomas & Kleinschmidt, 2009). Furthermore, the particle size enlargement during the coating process was also a factor contributing to the improvement in flowability. The larger particle size reduced the effective contact area per unit volume (Liu, et al., 2008), and it can therefore be seen that by improving the hardness of the particles, the flowability of the powder will be enhanced.

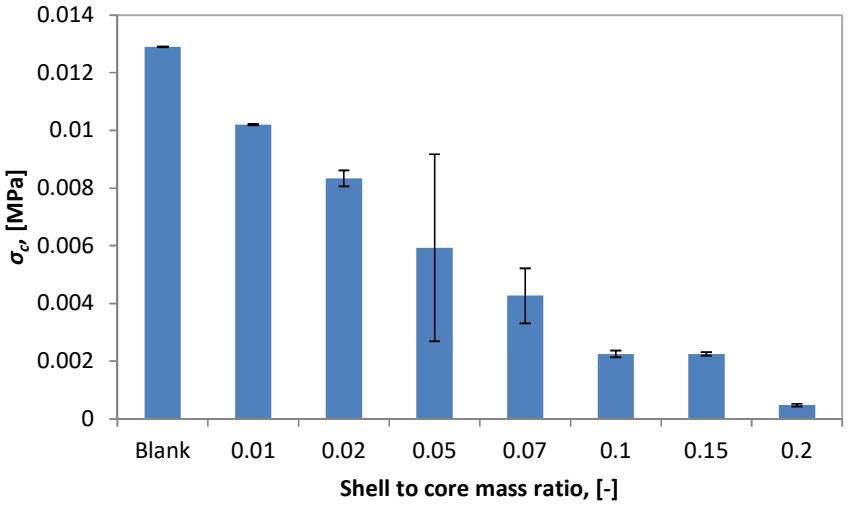

Figure 6.19 Unconfined yield stress of the HiLAS 33 KCl-coated samples determined using a ring shear-cell tester under 20 kPa pre-shear.

The unconfined yield stress of the different samples, σ_c, determined using the Schulze's ring shear-cell tester are shown in Figure 6.19. It was suggested that when samples coated with a shell-to-core mass ratio greater than 0.02, they were more resistant to caking. The unconfined yield stress is correlated to the flowability of the bulk powder, and hence it displayed a similar trend to Figure 6.18.

6.2.5 **Hygroscopicity**

In the previous section, it has been demonstrated that the coating of potassium chloride improved the flowability of the surfactant powder. This section aims to present the effect of the salt coating on the hygroscopic nature of the powder. Chapter 4 has shown that high adsorption of moisture would lead to high consolidation strength. This also means that the powder would be less stable in an environment with higher moisture, and the powder would be more prone to caking (unwanted agglomeration). In order to examine the ability of the coated powder to pick up moisture, a gravimetric technique was deployed.

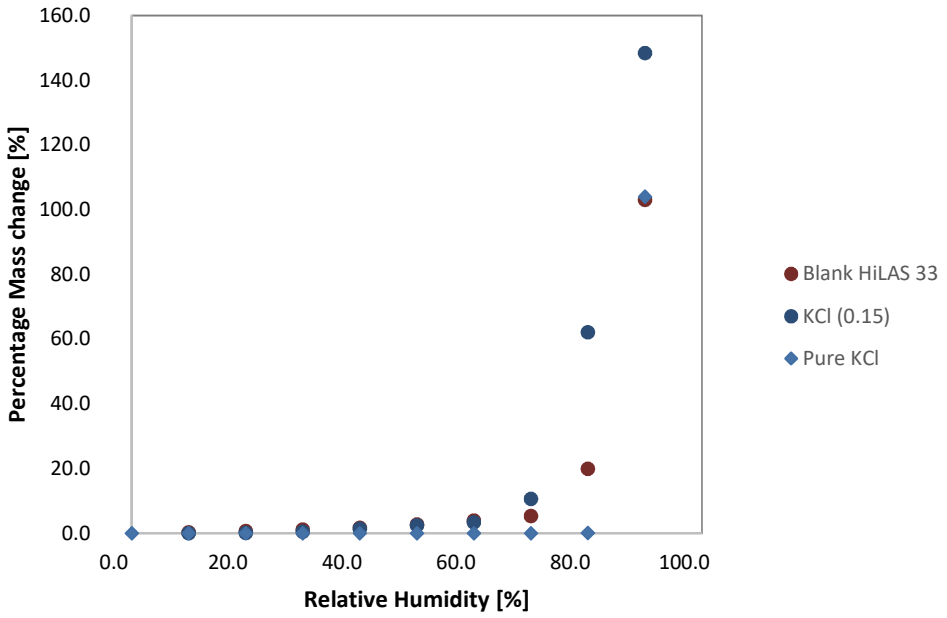

Figure 6.20 The water adsorption curve for the blank sample, coated HiLAS 33 powder (shell-to-core mass ratio of 0.15), and pure KCl.

The moisture adsorption behaviours of the blank sample, the HiLAS 33 powder fully coated by potassium chloride (shell-to-core mass ratio of 0.15), and pure KCl salt are displayed in Figure 6.20. It can be observed

that the KCl-coated particles deliquesced at a lower relative humidity than the blank sample. The deliquesce humidity for KCl salt, blank HiLAS 33 sample, and KCl-coated particles were 80.0% RH, 71.3% RH and 69.3% RH respectively. These were deduced from the rapid increase in change in mass with the relative humidity. Although the KCl salt deliquesced at almost 80% RH, the combination of the surfactant powder and the salt coating resulted in lower humidity where deliquescence occurred. This was in agreement with Salameh (2005), who was found that the binary mixture of the API and excipients resulted in lower relative humidity, where deliquescence commenced (Salameh & Taylor, 2005).

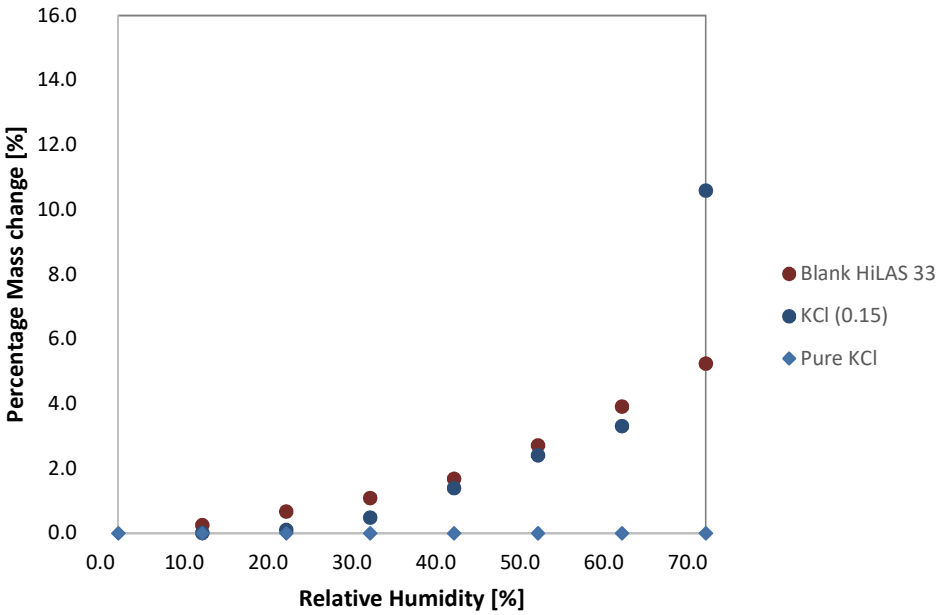

Figure 6.21 A close-up of the adsorption curve below 70% RH of the blank sample, KCl-coated HiLAS 33 powder (shell-to-core mass ratio of 0.15), and pure KCl.

The close-up of the adsorption behaviour of the different samples is displayed in Figure 6.21. Firstly, it can be observed that the potassium

chloride salt did not tend to pick up moisture when the relative humidity was less than 70%. Subsequently, in comparison between the uncoated and coated particles, the former seemed to pick up more moisture under 60% RH. This suggests that the salt coating reduced the moisture uptake before the coated particles started deliquescing. This result should be useful, as the product does not normally experience humidity higher than 50% RH in the storage bag (Rebecca, 2009).

6.3 Conclusions

Firstly, the coated particles were characterised by their size, shape, surface roughness, and particle density. Then, the coverage of the coating on the particles was characterised by using SEM. The mechanical properties of the powder were also investigated.

The results demonstrated that potassium chloride coating on the surfactant powder enhanced its flowability. The benefit was achieved when the shell-to-core mass ratios were more than 0.1, corresponding to 83% of the coating coverage around the particles, which was found to be related to the increase in the Heckel parameter value with the coating. The salt coating reduced the number of contact points and the ability of the particle to deform elastically and plastically, and would make the powder flow better. Furthermore, the salt coating also decreased the ability of the powder to pick up moisture from the environment. This would improve the storage stability of the powder. However, although the salt coating contributed to the improvement in the powder flowability and reduced the

moisture uptake, the coating reduced the humidity level where the sample deliquesced. In view of this, the coated sample will have to be stored in an environment lower than the deliquescence humidity (roughly around 70% RH).

Chapter 7. Surfactant Powder Coated with Different Materials

Previously, the difference between the surfactant powders HiLAS 33 and HiLAS 70 was studied with regard to their flowability and storage stability. It was found that while both samples were in the cohesive region, HiLAS 70 picked up moisture more easily due to its higher surfactant content, which resulted in higher consolidated stress. The effects of the particle size and Heckel parameter value of the sample on the flowability of HiLAS 70 were also studied. The investigation found that despite the increasing particle size, the mechanical properties of the large particles caused a reduction in their flowability.

Subsequently, it was demonstrated that with a potassium chloride coating on the surface of HiLAS 33 particles, the flowability improved and free-flowing powder under high consolidation stress could be achieved. This improvement was due to the enhanced hardness of the particles whereby they better resisted deformation, both elastically and plastically. Furthermore, it was shown that the salt coating reduced the moisture uptake under low humidity. However, it was also found that the salt coating resulted in lower deliquescence humidity, which was not desirable as it reduced the storage stability of the powder at high humidity.

The work presented in this chapter aimed to investigate the effects of another salt coating and a water-soluble polymer on the flowability and storage stability of the HiLAS 33 particles, to validate the main conclusions

reached in previous chapters. The coating was also applied to HiLAS 70 to examine the effect on the different core materials, in order to decrease the moisture intake of HiLAS 70 at low humidity.

7.1 Materials and Methods

As previously mentioned, many parameters could affect the quality of the coating. However, in this study, the focus was not on the effects of fluidised bed parameters on the coating quality, and hence, a constant set of parameters were implemented across the experiment.

7.1.1 Materials and Properties Measured

HiLAS 33 and HiLAS 70, supplied by P&G (Newcastle), were used as the surfactant powders and the core particles for the work presented in this chapter. Potassium chloride, sodium chloride, sodium sulphate, and polymer, EW base, were used as the coating materials. See Section 3.1 for more details.

The size and shape (Section 3.3), particle density (Section 3.4), coating coverage (Section 3.7), and hygroscopicity (Section 3.5) of the powder were analysed. Also, the bulk mechanical properties, Heckel parameters of the samples were determined using method in Section 3.9.1.

7.1.2 Coating of the surfactant powder

A Glatt® mini-fluidised bed coater, as previously mentioned in Section 3.10, was used for the coating process. Different coating solutions (20 wt% KCl solution, 20 wt% NaCl, 30 wt% Na_2SO_4, and 30 wt% EW base) were used

to coat the core particles of HiLAS 33. Different amounts of potassium chloride were applied to the core material and a range of salt (shell) to HiLAS 33 (core) mass ratios of 0.05–0.15 used. Triplicate coating experiments were carried out to ensure reproducibility. In order to ensure the consistency in results, the samples were stored and conditioned in a controlled environment at a temperature of 30°C and relative humidity of 30% before being analysed.

A set of blank samples was created to eliminate the effect of attrition and fragmentation due to the coating process. The controlled sample was produced by placing 30 g of the core material in the fluidised bed under the same conditions except without coating solution for a period of 1 hour.

In addition, the sodium sulphate was used to coat the highly concentrated surfactant powder, HiLAS 70. Ten grams of the raw material was placed in the fluidised bed chamber for each batch. Shell-to-core mass ratios of 0.15 and 0.25 were applied on the powder. The coated particles were subsequently kept in a dry condition in a desiccator for analysis.

7.1.3 **Flowability**

The flow behaviours of the samples were quantified using the method mentioned in detail in Section 3.11. A pre-shear pressure of 20 kPa was applied to investigate the effect of the pre-consolidation stress on the powder flowability. On the other hand, the standard test with a maximum of 3 kPa pre-shear pressure was used for the HiLAS 70-coated particles.

7.1.4 Storage stability

The storage stability was characterised by the unconfined yield stress of the consolidated powder bed, as outlined in Section 3.12. The sodium sulphate-coated HiLAS 70 powder was placed in a tableting mould (12 mm in diameter) in a desiccator for 24 hours. Following this, the unconfined yield stress of the powder bed under cyclic environmental conditions was obtained by firstly allowing the powder to be consolidated in an environmental chamber of 50% RH at 30˚C, and then exposing the sample to drying in the desiccator for 24 hrs. All of the unconfined yield stresses of the powder beds were obtained by compressing each consolidated bed with a flat probe of 100 mm diameter at a rate of 0.5 mm s^{-1} until the powder bed failed. The compression was carried out with the Instron microtester.

7.2 Results and Discussion

7.2.1 Sodium chloride-coated particles

In the previous chapter, it was demonstrated that flowability was improved with increasing amounts of potassium chloride coating on the surface of the surfactant powder. The flowability was enhanced from the cohesive region to the free-flowing region. In this section, the work presented aimed to examine whether the enhancement was transferable by using the sodium chloride salt.

In Table 7.1, the physical attributes of the coated particles are presented. In addition, the coating properties such as the surface coverage and coating thickness are also presented. It can be observed that the density of the sodium chloride-coated particles was less than that of the potassium chloride-coated particles for a given shell-to-core mass ratio. This was due to the different densities of the salts, KCl having a higher density than NaCl. The particle size of the coated particles was found to be similar, while the NaCl-coated surfactant particles were found to be more spherical than the KCl-coated particles.

Table 7.1 The properties of the coated surfactant particles, HiLAS 33, with two different salts, potassium chloride and sodium chloride. The errors presented in the table represent twice the standard error.

	Shell-to-Core Mass ratio [-]	Particle Density [g cm^{-3}]	Particle Size, d_{32} [µm]	Sphericity [-]	Coverage [-]	Thickness [µm]
KCl	0.05	1.83	323.3	0.67	-	-
	0.07	1.83	330.1	0.68	0.52 ± 0.12	-
	0.10	1.83	326.6	0.68	0.83 ± 0.15	-
	0.15	1.83	331.5	0.68	1	5.25 ± 0.32
NaCl	0.05	1.80	324.9	0.71	-	-
	0.07	1.80	323.8	0.72	-	-
	0.10	1.81	327.7	0.72	0.72 ± 0.26	-
	0.15	1.81	337.0	0.72	1	4.57 ± 0.82

The surface coverage by coating was also determined together with the thickness of the coating from the cross-sectional images of the coated

particles obtained using the SEM coupled with the energy dispersive X-ray spectrometer. It was found that the coverage of the sodium chloride on the particles was less than that of the potassium chloride for a given shell-to-core mass ratio of 0.10. It was observed that during the sodium chloride coating process, the salt crystallised on the tip of the atomisation nozzle. This resulted in more loss of coating material during the coating process and a reduction in shell thickness as seen in the fully coated particles. In addition, the process issue caused a higher error in surface coverage and thickness measurements, as the coating was less homogeneous.

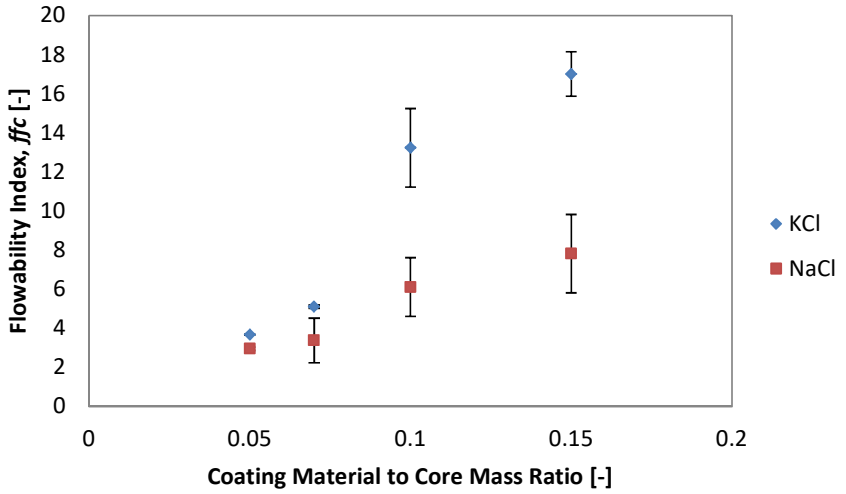

Figure 7.1 The flowability of the KCl- and NaCl-coated HiLAS 33 particles. The error bars represent twice the standard error of the mean.

The flowability indexes of both KCl- and NaCl-coated particles were then characterised and are presented in Figure 7.1. The NaCl-coated particles followed a similar trend to that of the KCl-coated particles, with their flowability improving as more coating was applied to the surface of the core particles. However, the enhancement of the flowability using sodium

chloride salt as the coating material was not as effective as the potassium chloride. The NaCl-coated sample showed a flowability index of 7.8 ± 1.2 for a coating-to-core mass ratio of 0.15, which is only in the easy-flowing region ($4 < ff_c < 10$), whilst the corresponding KCl-coated particles exhibited a flowability of 17.0 ± 0.9, in the free-flowing region ($ff_c > 10$). This was due to the less homogeneous coating, the reduced coverage, and the thinner shell produced by NaCl, as previously mentioned. This could also be due to the difference between potassium chloride and sodium chloride in molecular interactions with the core particles. The Hamaker constants calculated using the full Lifshitz model under a condition of full vacuum were found to be 6.8×10^{-20} J and 5.5×10^{-20} J for sodium chloride and potassium chloride respectively (Bergstrom, 1997). Greater Hamaker constants result in higher adhesion force between the particles, and hence, the flowability of NaCl was reduced.

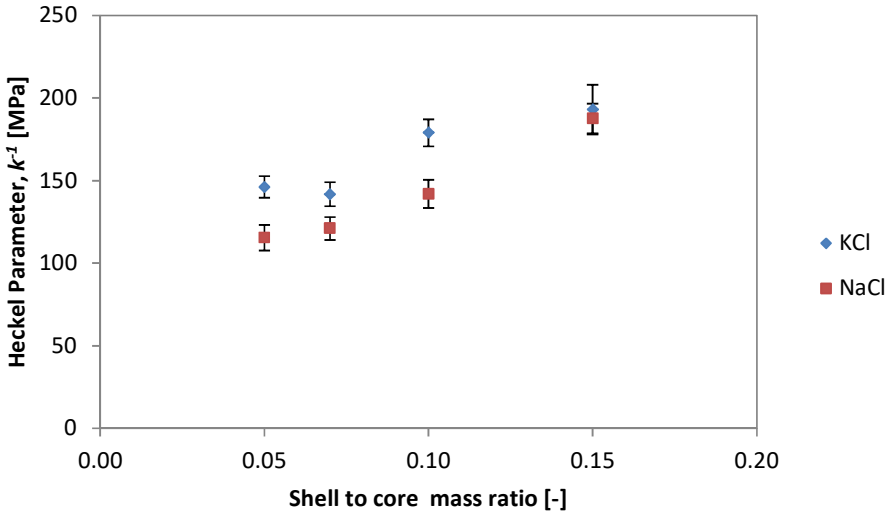

Figure 7.2 The derived Heckel parameters of the salt-coated HiLAS 33 particles. The error bars here represent the average standard error of the Heckel parameters derived from the different aspect ratios.

The Heckel parameters of the sodium chloride-coated particles were also derived and are compared in Figure 7.2 with those for potassium chloride. The K^{-1} values were derived from a confined compression test with different aspect ratios of the powder bed as outlined in the methods section. It was demonstrated that the sodium chloride coating, similarly to the potassium chloride coating, enhanced the K^{-1} value as the shell-to-core mass ratio increased. This suggests that the salt coatings were able to reduce the deformation both elastically and plastically when external force was applied. However, the significant enhancement was only observed when the shell-to-core mass ratio reached 0.10. This corresponds to 72% and 83% surface coverage of NaCl and KCl respectively on the core particles. Thus, in order to enhance the flowability of the powder, there was a minimum surface coverage threshold required by each salt.

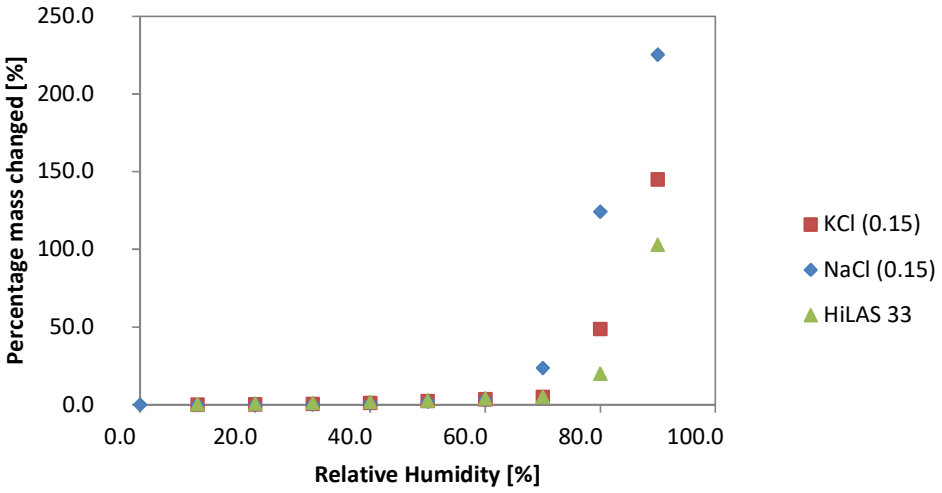

Figure 7.3 The adsorption behaviour of both KCl- and NaCl- coated HiLAS 33 powders under different humidity.

The moisture uptakes under various humidity levels were measured for both types of salt -coated particles for a given shell-to-core mass ratio of 0.15, and the results are exhibited with the control sample in Figure 7.3. It can be seen that both the KCl- and NaCl-coated particles were able to provide resistance to adsorption of moisture under lower humidity (< 70% RH) before the coated particles deliquesced. The deliquescence humidity of NaCl-coated particles (80.0% RH) was similar to that of KCl-coated particles (80.0% RH). The deliquescence humidity of pure sodium chloride at 293 K was found to be 75% RH comparing to 80% RH deliquescence humidity of KCl (Anon., 2000).

7.2.2 **Other coating materials**

Table 7.2 The particle characteristics of the surfactant particles, HiLAS 33, coated with different materials (potassium chloride, sodium chloride, EW base, and sodium sulphate).

Shell Material	Shell-to-Core Mass ratio [-]	Particle Density [g cm^{-3}]	Particle Size, d_{32} [μm]	Sphericity [-]	Coverage [-]
KCl	0.10	1.83	326.6	0.68	0.83 ± 0.15
	0.15	1.83	331.5	0.68	1.00
NaCl	0.10	1.81	293.7	0.68	0.71 ± 0.16
	0.15	1.81	325.1	0.68	1.00
EW base	0.05	1.88	348.4	0.64	0.36 ± 0.01
	0.10	1.82	454.2	0.59	0.67 ± 0.05
Na_2SO_4	0.10	1.90	311.0	0.68	0.32
	0.15	1.91	355.2	0.68	0.82 ± 0.12

The previous section has outlined how the salt coating on the surfactant powder enhanced its flowability. However, the salts deliquesced at high humidity, and so two other materials that are typically used in washing powder formulation, EW base (a water-based polymer) and sodium sulphate, were also investigated. More information on the ingredients can be found in Chapter 3.

Using a fluidised bed coater, the materials were used to coat the surface of the surfactant powder. The coated particles were then characterised and the results are presented in Table 7.2. The HiLAS 33 particles were only coated with the water-based polymer at shell-to-core mass ratios of 0.05 and 0.10. This was due to the apparently high viscosity of the coating liquid, which resulted in agglomeration instead of the formation of a shell layer. The agglomeration caused an increase in size of the EW base-coated particles at a shell-to-core mass ratio of 0.1, and lower sphericity. It was also found that EW base could provide a higher surface coverage than the other coating materials with the same shell-to-core mass ratio. This could be due to the larger droplets formed when atomising the coating liquid as the viscosity increased. These larger droplets could then bind and coat a relatively large area than the other coating materials. Furthermore, it was found that the coverage of the sodium sulphate on the core particles at a shell-to-core mass ratio of 0.15 was less than that of sodium chloride or potassium chloride. It was found that the viscosity of the coating materials NaCl (20 wt% solution), Na_2SO_4 (30 wt% solution),

and EW base (30 wt% solution), was 2.5 × 10^{-3} Pa s (Toolbox, 2007), 3.4 × 10^{-3} Pa s, and 0.44 Pa s respectively.

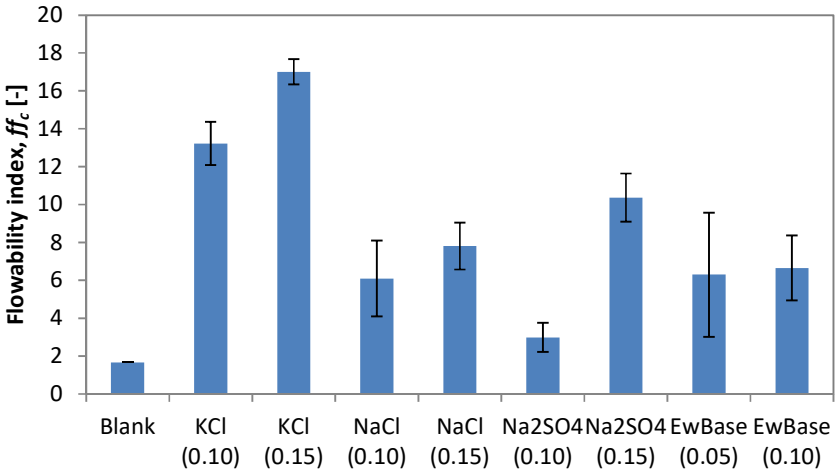

Figure 7.4 The flowability of the surfactant powder HiLAS 33 coated with different materials. A pre-shear pressure of 20 kPa was applied to the powder before the test. The error bars represent twice the standard error of the mean. The values in the brackets refer to the amount of coating material (shell-to-core mass ratio) on the surface of the HiLAS 33 particles.

The flowability of the coated particles was then characterised using a Schulze's ring shear test, the results of which are plotted in Figure 7.4. It should be noted that all the powder samples were pre-conditioned at 25°C and relative humidity of 30%. All types of coated surfactant particles showed an enhancement in flowability in comparison with the blank powder. Among them, it can be observed that potassium chloride performed the best for a shell-to-core mass ratio of 0.15, followed by sodium sulphate and then sodium chloride. However, when the shell-to-core mass ratio was reduced to 0.10, the sequence from the best to worst changed to KCl > NaCl ≅ EW base > Na_2SO_4. The particles coated by sodium sulphate under this condition still exhibited cohesive flow behaviour, since the coating did not achieve the minimum coverage that

was required for the improvement, as mentioned in the previous section. In order to achieve free-flow characteristics, more coating material is required, as demonstrated at a shell-to-core mass ratio of 0.15.

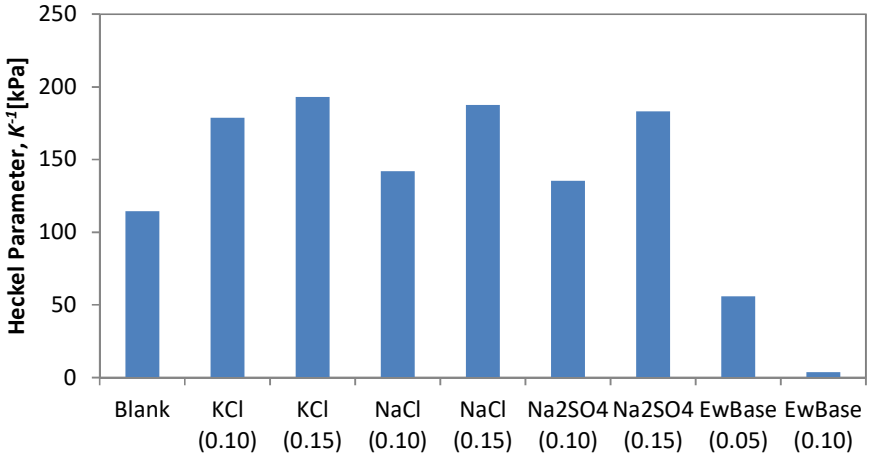

Figure 7.5 Heckel parameters of the uncoated particles (Blank), HiLAS 33, and those coated with various coating materials

The deformability of the coated particles was then characterised using a confined compression test to obtain the Heckel parameter. The results are displayed in Figure 7.5. It can be observed that the particles fully coated by the inorganic coating materials (shell-to-core mass ratio of 0.15) attained higher resistance to deformation in comparison to the blank surfactant powder.

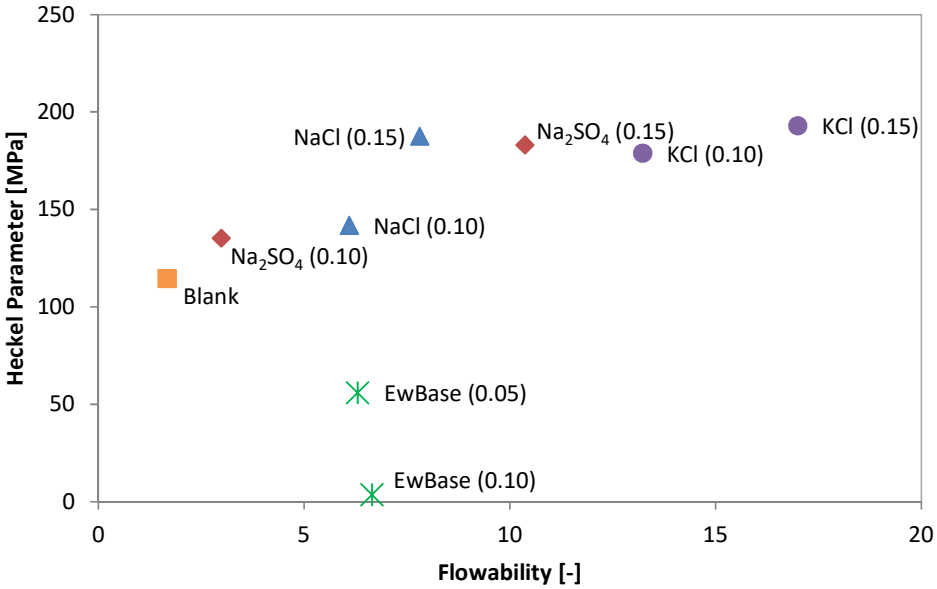

Figure 7.6 The relationship of the Heckel parameters and the flowability indexes of various coated and uncoated HiLAS 33 particles

The enhanced hardness of the particles resulted in an increase in flowability, as shown in Figure 7.6. It was also observed that different salt-coated particles (NaCl, Na_2SO_4, and KCl) with similar hardness displayed different flowability. This was due to the different inter-particle forces between the salts. From Equation (2.2) it can be seen that the adhesive force is a contributing force to powder flowability (free flow due to gravity). The difference in surface adhesion characteristics therefore resulted in irregularity flowability despite having similar Heckel parameters. Future work into investigation of the difference in surface adhesion between the salts should be conducted.

On the other hand, the results clearly show that EW base-coated surfactant powder, especially for the shell-to-core mass ratio of 0.10, was easier to deform as it had a lower Heckel parameter value than the

uncoated particles. However, the deformation did not lead to a reduction in flowability. Instead, the EW base-coated particles showed better flowability than the uncoated particles. To investigate the cause of the enhanced flow behaviour, the hygroscopicity of the powder was examined.

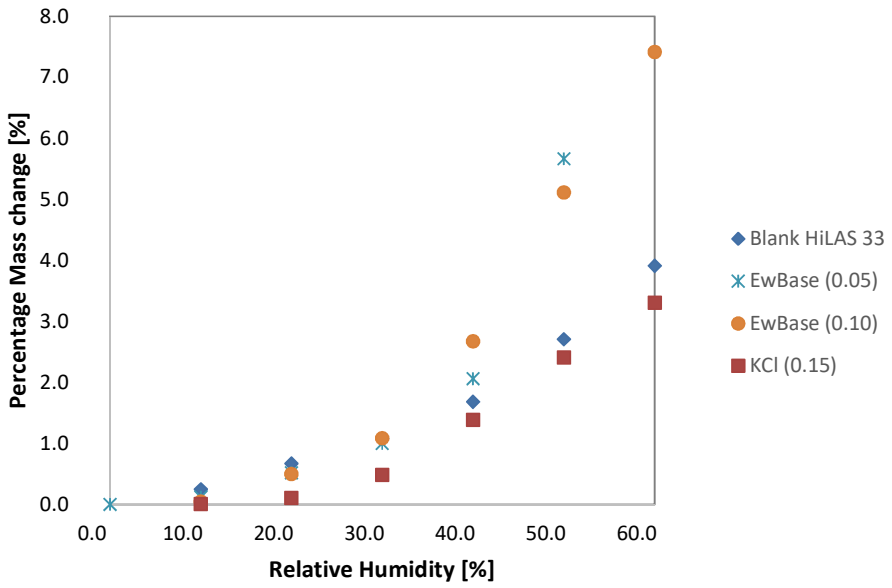

Figure 7.7 Moisture adsorption behaviour of EW base-coated surfactant powder in comparison to blank HiLAS

Using dynamic vapour sorption, the moisture adsorptions of the coated particles were examined. The results are presented in Figure 7.7. Unlike the salt coating results previously shown in Figure 7.3, the water-based polymer increased the amount of water uptake when the relative humidity was greater than 40%. The moisture adsorption on the surface of the particles could increase the adhesion by forming strong liquid bridges. On the other hand, it was found that the liquid could act as a lubricant among the particles and increase the distance between the particles, which reduced the vdW forces (Crouter & Briens, 2014; Emery, et al., 2009). It

seems that the moisture adsorbed by the uncoated surfactant powder deteriorated the flowability of the powder while the EW base-coated surface increased the flowability. The high moisture adsorption rate was possibly due to the -OH bonds attached to the monomer poly (acrylic acid-co-maleic acid) as shown in Figure 7.8. As a result, even when the EW base-coated particles were more deformable, the flowability of the particles was enhanced due to the moisture content on the surface. However, if the EW base-coated particles were to be exposed to a cyclic humidity cycle, the liquid bridges among the powder particles could result in higher cohesive force and thus decrease the storage stability (Crouter & Briens, 2014).

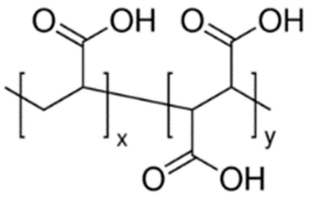

Figure 7.8. Chemical structure of poly(acrylic acid-co-maleic acid) (Anon., n.d.)

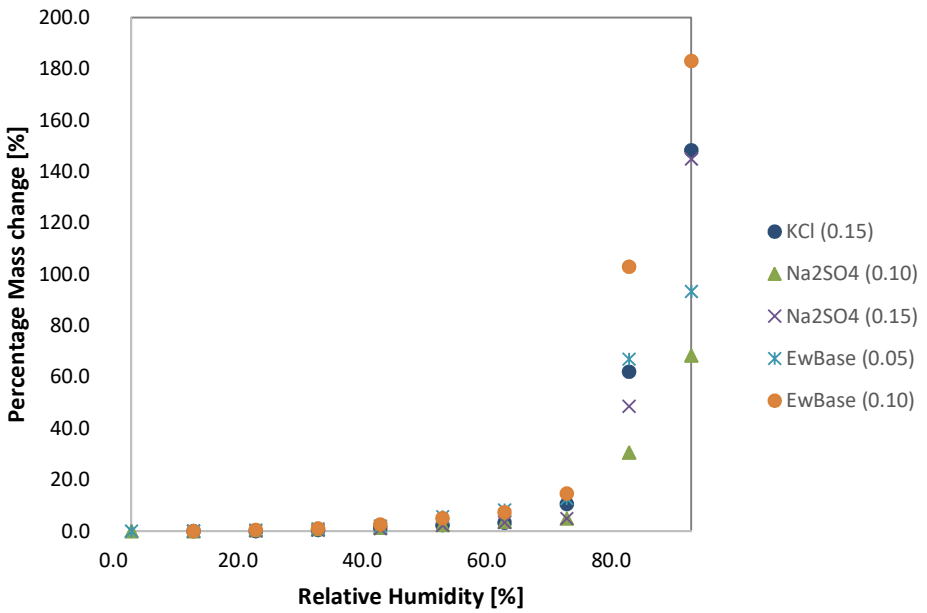

Figure 7.9 The adsorption curves of surfactant powder, HiLAS 33, coated with potassium chloride, sodium sulphate, and EW base

The adsorption curves of the surfactant powder coated with sodium sulphate, KCl, EW base and sodium sulphate are plotted together in Figure 7.8. This graph is the same graph as Figure 7.7 with different x-axis scaling. It can be found that the EW base coating resulted in reduced deliquesce humidity to 65.7% RH and 68.0% RH for shell-to-core mass ratios of 0.05 and 0.10 respectively in contrast to the 71% RH when the particles were not coated (Blank), while KCl-coated particles showed deliquesce humidity of 69.8% RH.

On the other hand, the sodium sulphate (shell-to-core mass ratio of 0.10) coating did not change the deliquesce humidity significantly. However, more sodium sulphate coating (shell-to-core mass ratio of 0.15) reduced the moisture adsorption in comparison with the other coating materials at high humidity when the salt deliquesced. Together with the ability to

reduce deformation under stress and the enhancement of the surfactant powder flowability, sodium sulphate can thus be considered to be a better coating material for storage under high-humidity environment than sodium chloride and potassium chloride.

7.2.3 Applying coating onto the highly surfactant powder HiLAS 70

After examining several coating materials and the different parameters that affected the flowability of HiLAS 33, the research aimed to achieve free-flowing and prolonged storage stability of the HiLAS 70 particles. As demonstrated in Chapter 4, higher surfactant composition resulted in a higher moisture uptake while the flowability was similar to the surfactant powder of lower concentration, HiLAS 33. In response to this, in an attempt to enhance the flowability and storage stability, sodium sulphate was applied onto the surface of the powder, following the work presented in the previous section.

Table 7.3 The size, shape, and coating material coverage of the sodium sulphate-coated HiLAS 70 particles together with the blank particles of HiLAS 70

	Shell-to-Core Mass ratio [-]	**Particle Density [g cm^{-3}]**	**Particle Size, d_{32} [µm]**	**Sphericity [-]**	**Coverage [-]**
HiLAS 70	Blank	1.31	224.2	0.7	-
Na_2SO_4	0.15	1.50	275.0	0.55	0.32 ± 0.21
Na_2SO_4	0.25	1.57	239.4	0.55	0.48 ± 0.12

In order to examine the effect of sodium sulphate on the surface of the surfactant powder, the coated particles' characteristics are presented in Table 7.3. It was found that a higher shell-to-core mass ratio was required to be applied onto the surface of the HiLAS 70 particles, as the powder had lower density than HiLAS 33. The results show that only a surface coverage of 32 ± 21% was achieved with a shell-to-core mass ratio of 0.15, the coverage increasing to 48 ± 12% 0.25 when the shell-to-core mass ratio was changed to 0.25. Furthermore, the HiLAS 70 particles had smaller particle size, d_{32}, which resulted in a higher surface area per volume in comparison with HiLAS 33 particles, and more coating material was therefore required. The additional coating material, however, was still not sufficient to achieve full coating of the particles.

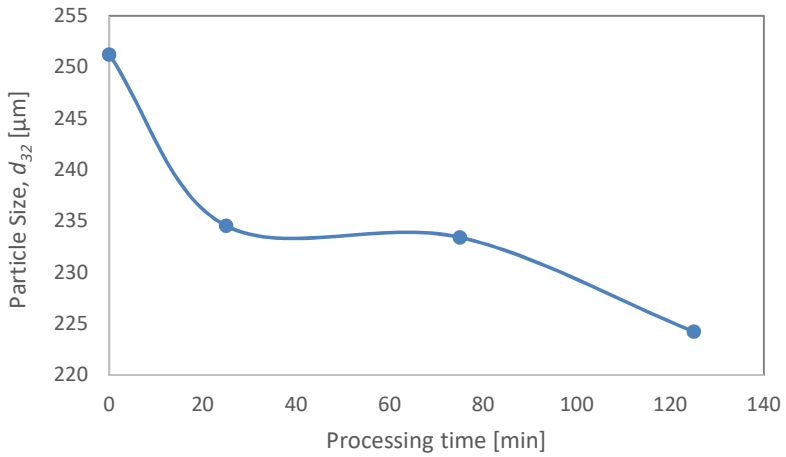

Figure 7.10 The particle size of the surfactant powder after various periods of processing time in the fluidised bed coater

Figure 7.10 shows how the size of the raw HiLAS 70 particles changed with time in the fluidised bed in the same operating conditions except

without the coating material. The apparent decrease in size with time was attributed to attrition and breakage of the particles. This phenomenon was also observed by Smith and Nienow (1983) whereby they reported an abrasive action in the fluidised bed that broke the particles down (Smith & Nienow, 1983). Furthermore, it is shown in Table 7.3 that the particles became less spherical after the coating process. It was also observed that the particle density increased with more coating material applied onto the surface of the surfactant powder, as expected.

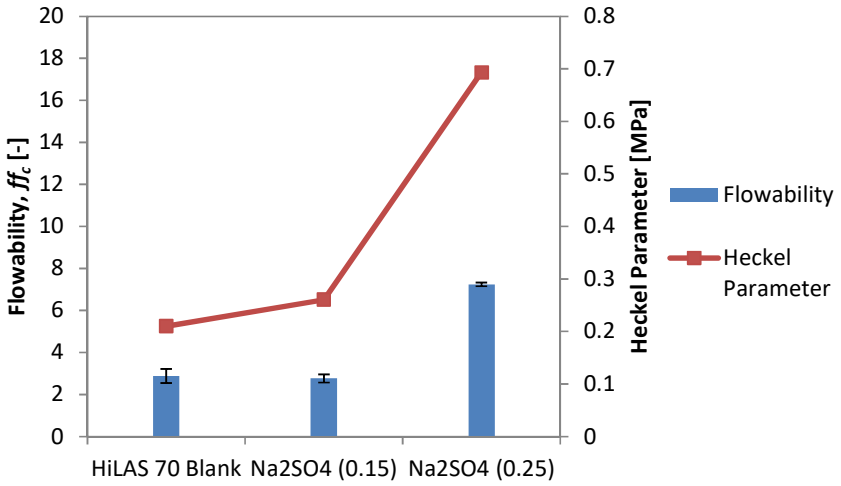

Figure 7.11 The flowability and Heckel parameter of the uncoated and sodium sulphate-coated surfactant HiLAS 70 powders

The hardness represented by the Heckel parameter and the flowability index of the uncoated and sodium sulphate-coated particles were determined, and the results are presented in Figure 7.11. It can be observed that the coated particles with a shell-to-core mass ratio of 0.25 showed a significant increase in hardness, the corresponding flowability index was also much higher, and the coated powders achieved the easy-

flowing region (Martin, 2008). On the other hand, the coating with a shell-to-core mass ratio of 0.15 improved neither the hardness nor the flowability of the powder, due to the low coverage (32 ± 21%) of the sodium sulphate on the core particles.

It should be noted that the data in this section is not comparable with the previous results in Section 6.2.4, as the powder had not been conditioned under 30% RH at 30°C before the characterisations. The sodium sulphate-coated particles produced with a shell-to-mass ratio of 0.25 appeared to have a higher Heckel parameter in comparison with the KCl-coated HiLAS 33, even though the coverage was less than 50%.

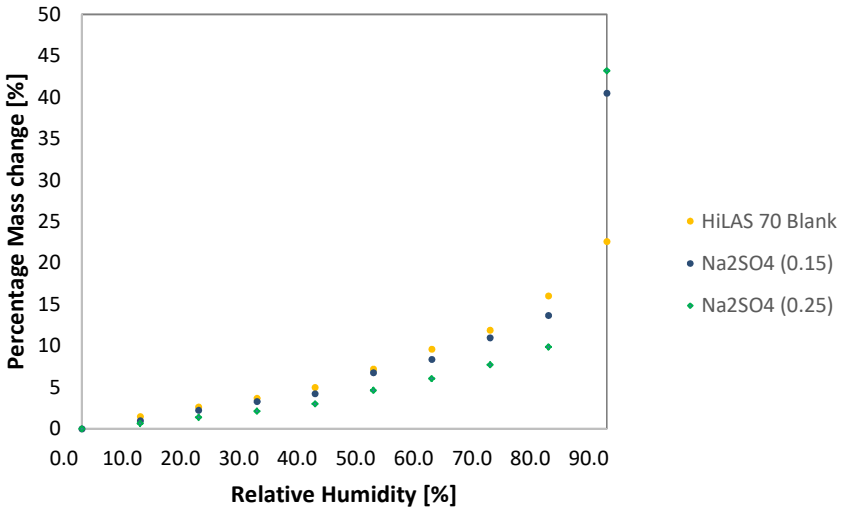

Figure 7.12 The moisture adsorption behaviours of the uncoated and sodium sulphate-coated HiLAS70 particles

The moisture adsorption characteristics of the coated particles were then obtained from the dynamic vapour sorption unit. The data are plotted in comparison with the uncoated particles in Figure 7.12. It shows that the coated particles with a shell-to-mass ratio of 0.15 improved the resistance

to the adsorption of water only marginally. When a shell-to-core mass ratio of 0.25 was used, the coating improved the hygroscopicity of the highly concentrated surfactant powder much more significantly. However, it also resulted in deliquesce of the particles under a relative humidity of 76.0%.

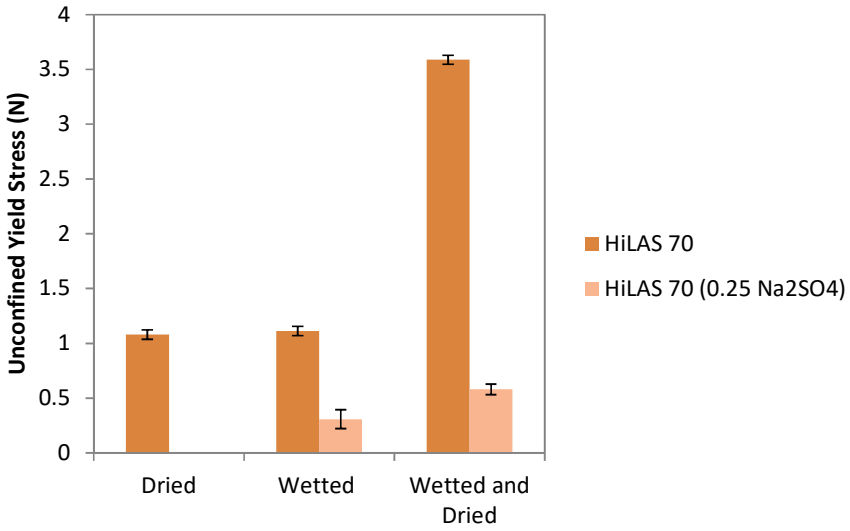

Figure 7.13 The consolidation stress of the raw HiLAS 70 and sodium sulphate-coated surfactant powder (shell-to-core mass ratio of 0.25).

The consolidation test was conducted in order to investigate the storage stability of the uncoated and coated powders. The results are displayed in Figure 7.13. It can be seen that the coating of sodium sulphate prevented caking under the dry conditions and reduced the consolidation stress when the powder was subjected to humidity and drying. In addition, the sodium sulphate-coated particles showed increased adhesion among the particles when the liquid bridge solidified. This was shown by the increase in the unconfined yield stress of the wetted and dried sodium sulphate-coated particles. The drop in the consolidation stress in comparison with

the uncoated particles was probably due to the reduction in moisture being adsorbed by the particles, as shown in Figure 7.12.

The results show that sodium sulphate was a good candidate to coat the highly concentrated surfactant powder, which was very hygroscopic. The material has shown to provide resistance to moisture uptake, and also an ability to enhance the flowability and material hardness. Ultimately, the material has been proven to increase the storage stability of the powder under 50% RH. However, the experiments did not include the optimisation of the coating process. Future work could involve optimisation of the coating process in order to increase the coverage of the coating material on the core particles.

7.3 Conclusions

In this chapter, it has been demonstrated that similarly to the potassium chloride salt, sodium chloride salt was able to enhance the flowability of the surfactant powder. This was achieved by applying a layer of coating onto the core particle surface with a minimum area coverage of 72%. It was also found that the Heckel parameter of the coated particles was positively correlated to the flowability of the powder. Furthermore, the salt coating also prevented the adsorption of moisture when the environmental relative humidity was less than 70%. However, the salt coating reduced the relative humidity where deliquescence occurred.

Subsequently, sodium sulphate and the water-soluble polymer EW base were used as the shell material to coat HiLAS 33 in order to further investigate the effect of different coating materials on the flowability and storage stability. It was found that both materials enhanced the flowability of the surfactant powder. However, the EW base-coated particles were the most hygroscopic, although the coating enhanced the flowability. This was probably because the adsorbed water acted as a lubricant among the particles, and the liquid bridges increased the gaps between the particles. These resulted in the reduction of the vdW force between them. On the other hand, the sodium sulphate-coated particles appeared to have better flowability in comparison to the uncoated and sodium chloride-coated particles. The sodium sulphate shell also reduced the moisture uptake of the powder.

With the results obtained from HiLAS 33, it was deducted that sodium sulphate would be a good candidate as the shell material for the HiLAS 70, which is highly hygroscopic. Na_2SO_4 was thus used to coat the highly concentrated surfactant powder. Improvements in flowability and storage stability were observed when a coating with a shell-to-core mass ratio of 0.25 was applied onto the surface of HiLAS 70 to generate less than 50% area coverage. After such coating, the surfactant powder was able to achieve easy-flow characteristics, and the moisture uptake was reduced. Furthermore, the consolidation strength of the coated particles at 50% relative humidity greatly decreased. However, the humidity level at which the powder deliquesced decreased to 68% with the salt coating on the

surface of the core particles. It can be inferred from this that the sodium sulphate-coated particles can be stored in a package with a humidity of below 60%.

Chapter 8. Overall Conclusions and Future Work

8.1 Overall Conclusions

It is expected that surfactant powder will continue to be the main ingredient in many commercial products, and the advantage of centralised production of this highly valued material has been discussed. It was found that the flow behaviour of adhesive powders can cause processing and storage problems in many different industries, pointing to a need to improve the flowability and storage stability of the powder to enable its transportation to different parts of the world.

Different mechanisms are behind the deteriorating flowability of the powder and the adhesion between the particles. Although several models have been developed to help understand the flowability of the powders, the complexity of powder systems has made the prediction of the flow behaviour difficult. Furthermore, it has been reported by Hart & Wu (2011) that the washing powder did not obey the prediction of the flowability models that larger particles will have better flowability. It was therefore necessary to better understand the relationship between the characteristics of surfactant powder, HiLAS 33 (33% surfactant) and HiLAS 70 (70% surfactant), and their flowability.

HiLAS 33 was found to have slightly worse flowability in comparison to HiLAS 70 and to deliquesce at low humidity of 71% RH due to the filler material, acetic acid salt, used. On the other hand, HiLAS 33 was

determined to have better storage stability than HiLAS 70 under 50% RH in a unconfined yield stress test. It was found that the better storage stability was due to HiLAS 70 had higher moisture adsorption affinity than HiLAS 33 in a low-humidity environment (lower than 70% RH) due to the natural hygroscopicity of linear alkylbenzene sulfonates. Moreover, it was demonstrated that HiLAS 33 deformed more easily than HiLAS 70 powder, as HiLAS 70 had a higher Heckel parameter value. The better flowability of HiLAS 70 powder was due to the lower deformability of the material.

To further investigate on the effects of the physical characteristics on the flow behaviour of highly concentrated surfactant particles, different size ranges of the surfactant powder and their flowability were investigated. It has been demonstrated in this research that the HiLAS 70 powder had smaller size but better flowability, which is in agreement with the findings of Hart & Wu (2011). This was found to be attributed to the mechanical properties of the larger particles, which deformed more easily than the smaller particles. This resulted in larger contact area between larger particles, leading to higher adhesion due to sintering. However, as the particles get smaller, the vdW force can become more significant.

The flowability data were fitted to an existing model (Liu, et al., 2008), which was found to be insufficient for predicting the flow behaviour of the powder. A new model was thus proposed in this chapter and was used to fit the results obtained from the highly concentrated surfactant powder. In this new model, it was demonstrated that the Heckel parameter is directly proportional to the flowability of the powder.

An attempt was made to characterise the mechanical properties of single particles using micro-manipulation. It was discovered that the data obtained are quite scattered due to the irregular shape of the particles, which caused varying contact points and contact areas between the particles and the compression probe. These made determination of their deformation difficult. In view of this, bulk powder characterisations using the Heckel parameter were used instead to quantify the hardness of the powder.

In this project, it was established that the hardness of the particles directly affects the flowability of the powder. Salt coating was therefore used in an attempt to increase the mechanical properties and hence the flowability of the powder. Coatings of NaCl, KCl, and Na_2SO_4 on the surfactant exhibited enhancement of the flowability of the bulk powder when 70% coverage of the coating surface was achieved. However, NaCl- and KCl-coated particles deliquesced at lower humidity. Sodium sulphate, on the other hand, was shown to be capable of enhancing the storage stability of the surfactant powder by reducing its adsorption affinity. It was shown that coating with sodium sulphate salt (0.25 shell-to-core mass ratio) reduced the consolidation stress under constant pressure of 0.75 MPa in 60% RH ambient conditions.

A water-based polymer, EW base, was also used as a coating material to enhance the flowability of the powder. The coated particles demonstrated improvement in flowability despite reduction in mechanical strength (lower Heckel parameter). Due to the hygroscopic nature of the water-based

polymer, it was the ability to adsorb water that caused the reduction in vdW forces by increasing the separation between particles. The moisture adsorbed also acted as a lubricant among the particles which resulted in the enhanced flowability.

In conclusion, the high storage stability and flowability of the surfactant powder were enhanced through coating with sodium sulphate. In addition, a new model was established to include the deformability of the particle, described by Heckel parameter, in the flowability model.

8.2 Future Work

Further research into the effects of particle size on the flowability of surfactant powders, based on the results shown in Chapter 5, is recommended. The data in the current work were not sufficient to demonstrate the benefits of the new proposed model beyond doubt. A narrower particle size range could be used for this investigation. Furthermore, the model could be improved by introducing surface chemistry properties, hygroscopicity, and crystalline structure, as it was indicated that these properties had an effect on flowability and storage stability.

The micromanipulation technique to measure the mechanical properties of single particles could be improved. An environmental chamber to control humidity and temperature could be installed and more cameras fitted into the rig to provide an accurate estimation of the contact area.

It has been found that salt coatings can improve the flowability of the surfactant powder. Future work could be considered to expand the use of other materials used as the coating material in order to build further understanding on how differences in surface chemistry can affect the flowability and storage stability of the powder. Furthermore, a combination of materials, such as water-soluble polymer with salt, might be exploited.

In addition to the above, different coating parameters could be investigated. These parameters include nozzle diameter, rate of drying, viscosity of the coating solution, and shear rate in the fluidised bed. These will affect the characteristics of the applied shell, such as density, crystalline structure, surface roughness, and coverage. Different coating methods, such as a twin-screw mixer, could also be investigated in the future. This would provide a cheap continuous alternative process, as fluidised beds have high operating and capital costs.

REFERENCES

Adams, M. & McKeown, R., 1996. Micromechanical analyses of the pressure-volume relationships for powders under confined uniaxial compression. *Powder Technology,* Volume 88, pp. 155-163.

Aguilera, J. M., Valle, J. M. d. & Karel, M., 1995. Caking phenomena in amporphous food powders. *Trends in Food Science & Technology,* Volume 6, pp. 149-155.

Althaus, T. O., Windhab, E. J. & Scheuble, N., 2012. Effect of pendular liquid bridges on the flow behavior of wet powders. *Powder Technology,* Volume 217, pp. 599-606.

Anon., 2000. Infrared Observations of the Response of NaCl, MgCl2, NH4HSO4, and NH4NO3 Aerosols to Changes in Relative Humidity from 298 to 238 K. *J. Phys. Chem. A,* Volume 104, pp. 2038-2047.

Anon., n.d. *Sigma-Aldrich Website.* [Online] Available at: http://www.sigmaaldrich.com/catalog/product/aldrich/416053?lang=en&region=GB [Accessed December 2016].

Bajpai, D. & Tyagi, V., 2007. Laundry Detergents: An Overview. *Journal of Oleo Science,* 56(7), pp. 327-340.

Barthel, E., 2008. Adhesive elastic contacts - JKR and more. *Journal of Physics D: Applied Physics,* 41(16).

Bergstrom, L., 1997. Hamaker constant for inorganic materials. *Advances in Colloid and Interface Science,* Volume 70, pp. 125-169.

Blumel, C. et al., 2015. Increasing flowability and bulk density of PE-HD powders by a dry particle coating process and impact on LBM processess. *Rapid Prototyping Journal,* 21(6), p. 697.

Boerefijn, R., Dontula, P.-R. & Kohlus, R., 2007. Detergent Granulation. In: *Handbook of Powder Technology.* s.l.:Elsevier.

Breakspear, S. & Smith, J., 2004. Returning to the same area of hair surfaces before and after treatment: a longitudinal AFM technique. *Journal of Microscopy,* 215(1), p. 34–39.

Brunauer, S., Emmett, P. H. & Teller, E., 1938. Adsorption of gases in multimolecular layers. *Journal of the American Chemists' Society,* pp. 309-319.

Calvert, G. et al., 2013. A new environment bulk powder caking tester. *Powder Technology,* Volume 249, pp. 323-329.

Chateau, M.-E., Galet, L., Soudais, Y. & Fages, J., 2005. Processing a detergent powder formulation: Direct compression, and high shear wet granulation followed by compression. *Powder Technology,* Volume 157, pp. 191-198.

Chattoraj, S., Shi, L. & Sun, C. C., 2011. Profoundly Improving Flow Properties of a Cohesive Cellulose Powder by Surface Coating with Nano-silica Through Comilling. *Journal of Pharmaceutical Sciences,* Volume 100, p. 4943–4952.

Chung, M. S. et al., 2000. Study of Caking in Powdered Foods Using Nuclear Magnetic Resonance Spectroscopy. *Food Engineering and Physical Properties,* Volume 65, pp. 134-138.

Cleaver, J. A. S. & Looi, L., 2007. AFM study of adhesion between polystyrene particles; - The influence of relative humidity and applied load. *Powder Technology,* Volume 174, pp. 34-37.

Crouter, A. & Briens, L., 2014. The Effect of Moisture on the Flowability of Pharmaceutical Excipients. *AAPS PharmSciTech,* 15(1), pp. 65-73.

Derjaguin, B., Muller, V. M. & Toporov, Y. P., 1975. Effect of contact deformations on the adhesin of particles. *Journal of Colloid and Interface Science,* 53(2), p. 314.

El Hagrasy, A. S. et al., 2013. Twin screw wet granulation: Influence of formulation parameters on granule properties and growth behavior. *Powder Technology,* Volume 238, pp. 108-115.

El Hagrasy, A. S. et al., 2013. Twin screw wet granulation: Influence of formultation parameters on granule properties and growth behavior. *Powder Technology,* Volume 238, pp. 108-115.

Emery, E. et al., 2009. Flowability of moist pharmaceutical powders. *Powder Technology,* Volume 189, pp. 409-415.

Faure, A., York, P. & Rowe, R. C., 2001. Process control and scale0up of pharmaceutical wet granulation processes: a review. *European Journal of Pharmaceutics and Biopharmaceutics ,* Volume 52, pp. 269-277.

Fitzpatrick, J. J. et al., 2004. Effect of powder properties and storage conditions on the flowability of milk powders with different fat contents. *Journal of Food Engineering,* Volume 64, pp. 435-444.

Freeman, R., 2007. Measuring the flow properties of consolidated, conditioned and aerated powders - A comparative study using a powder rheometer and a rotational shear cell. *Powder Technology ,* pp. 25-33.

Freeman, T., Brockbank, K. & Armstrong, B., 2015. Measurement and quantification of caking in powders. *Procedia Engineering,* Volume 102, pp. 35-44.

Fu, X. et al., 2012. Effect of particle shape and size on flow properties of lactose powders. *Particuology,* Volume 10, pp. 203-208.

Ganesan, V., Rosentrater, K. & Muthukumarappan, K., 2008. Flowability and handling characteristics of bulk solids and powders- a review with implications for DDGS. *Biosystems Engineering ,* Volume 101, pp. 425-435.

Godridge, R., 2009. *Predictive Storage Stability of Granular Laundry Detergents.* s.l.:University of Birmingham.

Goldstein, J. et al., 2003. *Scanning Electron Microscopy and X-ray Microanalysis.* s.l.:Springer.

Griffith, E. J., 1992. Cake Formation in Particulate Systems. *VCH Publishers,* Volume 334, pp. 1770-1837.

Hart, A., 2015. Effect of Particle Size on Detergent Powders Flowability and Tabletability. *Chemical Engineering & Process Technology,* 6(1).

Hart, A., 2015. Effect of Particle Size on Detergent Powders Flowability and Tabletability. *J Chem Eng Process Technol,* 6(1), p. 215.

Hartmann, M. & Palzer, S., 2011. Caking of amorphous powders — Material aspects, modelling and applications. *Powder Technology,* Volume 206, pp. 112-121.

Haughey, D. P. & Beveridge, G. S. G., 1966. Local voidage variation in a randomly packed bed of equal-sized spheres. *Chemical Engineering Science,* Volume 21, pp. 905-916.

Israelachvili, J. N., 2011. *Intermolecular and Surface Forces.* s.l.:Elsevier.

Iverson, S. M. et al., 2001. Growth regime map for liquid-bound granules: further development and experimental validation. *Powder Technology ,* Volume 117, pp. 83-97.

JOEL, 2009. *Basic Knowledge for Using the SEM,* s.l.: s.n.

Johanson, K. D., 2009. Effect of particle shape on unconfined yield strength. *Powder Technology,* 194(3), pp. 246-251.

Johnson, K. L., Kendall, K. & Roberts, A. D., 1971. Surface energy and the contact of elastic solids. *Proc. Roy. Soc.,* Volume 324, pp. 301-313.

Jones, R., Pollock, H. M., Geldart, D. & Verlinden, A., 2003. Inter-particle forces in cohesive powders studied by AFM: effects of relative humidity, particle size and wall adhesion. *Powder Technology,* Volume 132, pp. 196-210.

Kock, I. & Huhn, K., 2007. Influence of particle shape on the fricitional strength of sediments - A numerical case study. *Sedimentary Geology,* Volume 196, pp. 217-333.

Krupp, H., 1967. Particle adhesion theory and experiment. *Adv. Colloid Interface Sci.,* Volume 1, pp. 111-239.

Landi, G., Barletta, D. & Poletto, M., 2011. Modelling and experiments on the effect of air humidity on the flow properties of glass powders. *Powder Technology,* Volume 207, pp. 437-443.

Leturia, M. et al., 2014. Characterization of flow properties of cohesive powders: study of traditional and new testing methods. *Powder Technology,* Volume 253, pp. 406-423.

Li , Q., Rudolph, V., Weigl, B. & Earl, A., 2004. Interparticle van der Waals force in powder flowability and compactibility. *International Journal of Pharmaceutics,* Volume 280, pp. 77-93.

Lipasek, R. A., Ortiz, J. C., Taylor, L. S. & Mauer, L. J., 2012. Effects of anticaking agents and storage conditions on the moisture sorption, caking and flowability of deliquescent ingredients. *Food Research International,* Volume 45, pp. 369-380.

Liu, L. X. et al., 2008. Effect of particle properties on the flowability of ibuprofen powders. *International Journal of Pharmaceutics,* Volume 362, pp. 109-117.

Lozano, J. E., Rotstein, E. & Urbicain, M. J., 1983. Shrinkage, Porosity and Bulk Density of Foodstuffs at Changing Moisture Contents. *Journal of Food Science,* Volume 48, pp. 1497-1553.

Marigo, M. et al., 2014. Relationship between single and bulk mechanical properties for zeolite ZSM5 spray-dried particles. *Particuology,* Volume 14, pp. 130-138.

Martin, R., 2008. *Introduction to Particle Technology.* Chichester: Wiley.

Mauer, L. J. & Taylor , L. S., 2010. Water-Solids Interactions Deliquescence. *Annual Review of Food Science and Technology,* pp. 41-63.

Maugis, D. & Pollock, H. M., 1984. Surface forces, deformation and adherence at metal microcontacts. *Acta Metalls,* 32(9), pp. 1323-1334.

Mei, R., Shang, H., Klausner, J. F. & Kallman, E., 1997. A Contact Model for the Effect of Particle Coating on mproving the Flowability of Cohesive Powders. *KONA,* Volume 15, p. 132.

Mellmann, J., Hoffmann, T. & Furll, C., 2013. Flow properties of crushed grains as a function of the particle shape. *Powder Technology,* Volume 249, pp. 269-273.

Mettler Toledo, n.d. *What is a moisture analyzer and how does it work?.* [Online] Available at: https://www.mt.com/gb/en/home/library/FAQ/laboratory-weighing/what-is-a-moisture-analyzer.html
[Accessed 31 January 2018].

Molenda, M. & Stasiak, M., 2002. Deterination of the elastic constants of cereal grains in a uniaxial cmpression test. *Int. Agrophysics,* Volume 16, pp. 61-65.

Mullins, M. E. et al., 1992. Effect of Geometry on Particle Adhesion. *Aerosol Science and Technology,* 17(2), pp. 105-118.

Newitt, D. M. & Conway Jones, J. M., 1958. A contribution to the theory and practice of granulation. *Trans. IChemE,* pp. 422-442.

Oliver, W. & Pharr , G., 2004. Measurement of hardness and elastic modulus by instrumented indentation: Advances in understanding and refinements to methodology. *Journal of Materials Research,* 19(1), pp. 3-20.

Onwulata, C. I., Konstance, R. P. & Holsinger, V. H., 1996. Flow Properties of Encapsulated Milkfat Powders as Affected by Flow Agent. *Journal of Food Science,* 61(6), pp. 1211-1215.

Peleg, M., 1977. Flowability of Food Powders and Methods for its Evaluation - A Review. *Journal of Food Process and Engineering ,* Volume 1, pp. 303-328.

Prescott, J. K. & Barnum, R. A., 2000. On Powder Flowability. *Pharmaceutical Technology,* pp. 60-84.

Rebecca, G., 2009. *Predictive Storage Stability of Granular Laundry Detergents,* s.l.: University of Birmingham, School of Chemical Engineering.

Rhodes, M., 2013. *Introduction to Particle Technology.* s.l.:John Wiley & Sons.

Rieck, C. et al., 2015. Influence of drying conditions on layer porosity in fluidized bed spray granulation. *Powder Technology,* Volume 272, pp. 120-131.

Rock, M., 2006. Development of an Uniaxial Caking Tester. *Chem. Eng. Technol.,* 29(6), pp. 679-685.

Rosen, M. J. & Kunjappu, J. T., 2012. *Surfactants and Interfacial Phenomena.* New Jersey: John Wiley & Sons.

Rough, S. L., Wilson, D. I., Bayly, A. E. & York, D. W., 2005. Influence of process parameters on the tapping characteristics of high shear mixer agglomerates made with ultra-high viscosity binders. *Chemical Engineering Research and Design,* 83(A1), pp. 7-23.

Salameh, A. K. & Taylor, L. S., 2005. Deliquescence in Binary Mixtures. *Pharmaceutical Research,* 22(2), pp. 318-324.

Samimi, A., Hassanpour, A. & Ghadiri, M., 2005. Single and bulk compresssions of soft granules: Experimental study and DEM evaluation. *Chemical Engineering Science,* Volume 60, pp. 3993-4004.

Saw, H. Y., Davies, C. E., Paterson, A. H. J. & Jones, J. R., 2013. *The Inflouence of Particle Size Distribution and Tapping on the Bulk Density of Milled Lactose Powders.* Barton, s.n.

Schulze, D., 2006. *Flow properties testing with Ring Shear Testers RST-01.01, RST-01.pc, and RST-XS,* s.l.: s.n.

Schulze, D., 2011. *Flow Properties of Powders and Bulk Solids,* Wolfenbüttel, Germany: Ostfalia University of Applied Sciences.

Schulze, D., 2011. *Flow Properties of Powders and Bulk Solids,* Wolfenbüttel, Germany: Ostfalia University of Applied Sciences.

Sebhatu, T., Ahlneck, C. & Alderborn, G., 1997. The effect of moisture content on the compression and bond-formation properties of amorphous lactose particles. *Internation journal of Pharmaceutics,* Volume 146, pp. 101-114.

Seville, J., Willett, C. & Knight, P., 2000. Interparticle forces in fluidistion: a review. *Powder Technology,* Volume 113, pp. 261-268.

Smith, P. G. & Nienow, A. W., 1983. Particle Growth Mechanisms in Fluidised Bed Granulation - the Effect of Process Variables. *Chemical Engineering Science,* 38(8), pp. 1223-1231.

Sonnergaard, J., 1999. A critical evaluation of the Heckel equation. *Internation Journal of Pharmaceutics,* Volume 193, pp. 63-71.

Stoklosa, A. M., Lipasek, R. A., Taylor, L. S. & Mauer, L. J., 2012. Effects of storage conditions, formulation, and particle size on moisture sorption and flowability of powders: A study of deliquescent ingredient blends. *Food Research International,* Volume 49, pp. 783-791.

Sun, J., 2011. *The Use of Dynamic Vapor Sorption Method in the Determination of Water Sorption Limit and Setting Specification for Drug Substance,* s.l.: s.n.

Teunou, E. & Fitzpatrick, J. J., 2000. Effect of storage time and consolidation on food powder flowability. *Journal of Food Engineering,* Volume 43#, pp. 97-101.

Tomas, J., 2000. Particle Adhesion Fundamentals and Bulk Powder Consolidation. *KONA Powder and Particle Journal,* Issue 18, pp. 157-169.

Tomas, J., 2001. Assessment of Mechanical Properties of Cohesive Particulate Solids. Part 2: Powder Flow Criteria. *Particulate Science and Technology,* Volume 19, pp. 111-129.

Tomas, J. & Kleinschmidt, S., 2009. Improvement of Flowability of Fine Cohesive Powders by Flow Additives. *Chem. Eng. Technol,* Volume 10, pp. 1470-1483.

Toolbox, E., 2007. *Sodium Chloride and Water.* [Online] Available at: Available at: https://www.engineeringtoolbox.com/sodium-chloride-water-d_1187.html
[Accessed 11 October 2007].

Vesey, C., Cronlein, J., Breuer, A. & Gerstner, S., 2014. *Fluid Bed Nozzle Spray Characterization of an Aqueous Ethylcellulose Dispersion for Particle Taste-Masking Applications,* s.l.: Surelease.

Voutou, B., Stefanaki, E.-C. & Giannakopoulos, K., 2008. *Electron Microscopy: The Basics,* s.l.: Physics of Advanced Materials Winter School.

Weigl, B. et al., 2006. Comparative Testing of Powder Caking. *Chem Eng Technol,* 29(6), pp. 686-690.

Weisstein, E. W., n.d. *Oblate Spheroid.* [Online] Available at: http://mathworld.wolfram.com/OblateSpheroid.html [Accessed 20 Jan 2018].

Yap, S. F., Adams, M. J., Seville, J. P. & Zhang, Z., 2008. Single and bulk compression of pharmaceutical excipients: Evaluation of mechanical properties. *Powder Technology,* Volume 185, pp. 1-10.

Yu, Y., Zhao, J. & Andrew, E. B., 2008. Development of Surfactants and Builders in Detergent Formulations. *Chinese Journal of Chemical Engineering,* 16(4), pp. 517-527.

Zafar, U. et al., 2017. A review of bulk powder caking. *Powder Technology,* Volume 313, pp. 389-401.

Zhou, H. & Peukert, W., 2008. Modeling Adhesion Forces between Deformable Bodies by FEM and Hamaker Summation. *Langmuir,* Volume 24, pp. 1459-1468.